UNIVERSITY OF BELGRADE

FACULTY OF PHYSICS

INSTITUTE OF METEOROLOGY

Miloš N. Lompar

NUMERICAL MODELLING OF WARM AND COLD TYPE RAIN MODIFICATION

Doctoral Dissertation

Belgrade, 2018

УНИВЕРЗИТЕТ У БЕОГРАДУ

ФИЗИЧКИ ФАКУЛТЕТ

ИНСТИТУТ ЗА МЕТЕОРОЛОГИЈУ

Милош Н. Ломпар

Моделовање модификације падавина топлог и хладног типа

докторска дисертација

Београд, 2018

Подаци о ментору и члановима комисије

Ментор:

Проф. др. Млађен Ђурић, редовни професор у пензији

Институт за метеорологију, Физички факултет, Београд

Чланови комисије:

Проф. др. Млађен Ђурић

Редовни професор у пензији, Физички факултет, Београд

Проф. др. Дејан Јанц

Вандредни професор, Физички факултет, Београд

Проф. др. Мирјана Румл

Редовни професор, Пољопривредни факултет, Београд

Numerical modelling of warm and cold type rain modification

Abstract

Numerical models capable to simulate rain modification process are powerful tools of modern civilization, which helps scientist and laboratory researchers to determine the ability of newly produced reagent to enhance precipitation. Such models allow scientists to investigate what characteristics new material should have in order to give positive effect in weather modification process and this can determine further laboratory research. The use of such model is more economical than to conduct real seeding experiments and enables unlimited number of calculations and analysis to be done.

New gust front pulsation parameterization scheme is introduced in this thesis in order to improve Weather Research and Forecasting (WRF)–Advanced Research WRF (WRF–ARW) numerical model capabilities to simulate cloud development and rain formation process. The influence of this new scheme on model performances is tested through investigation of the characteristics of an idealized supercell cumulonimbus cloud in WRF, as well as studying a real case of thunderstorms above the United Arab Emirates. In the idealized case, WRF with the gust front parameterized produces more precipitation and shows different time evolution of mixing ratios of cloud water and rain, whereas the mixing ratios of ice and graupel are unchanged when compared to the default WRF run without the parameterization of gust front pulsation. The included parameterization did not disturb the general characteristics of thunderstorm cloud, such as the location of updraft and downdrafts, and the overall shape of

the cloud. New cloud cells in front of the parent thunderstorm are also evident in both idealized and real cases due to the included forcing of vertical velocity caused by the periodic pulsation of the gust front head. Despite the differences between two WRF simulations and satellite observations, the inclusion of the gust front parameterization scheme produced more cumuliform clouds thus matching the results better with the observations.

In this study, an analysis of the capabilities of existing weather models to simulate cloud development and rain formation process using explicit versus implicit treatment of natural aerosols is presented. The testbed selected for this study is a severe mesoscale convective system with supercells that struck west and central parts of Serbia in the afternoon of July 21, 2014. Numerical products of two model runs, i.e. one with aerosols explicitly (WRF-AE) included and another with aerosols implicitly (WRF-AI) assumed, are compared against precipitation measurements from surface network of rain gauges, as well as against radar and satellite observations. The WRF-AE model accurately captured the transportation of dust from the north Africa over the Mediterranean and to the Balkan region. On smaller scales, both models displaced the locations of clouds situated above west and central Serbia towards southeast and under-predicted the maximum values of composite radar reflectivity. Similar to satellite images, WRF-AE shows the mesoscale convective system as a merged cluster of cumulonimbus clouds. Both models over-predicted the precipitation amounts; WRF-AE over-predictions are particularly pronounced in the zones of light rain, while WRF-AI gave larger outliers.

Since modeling capabilities of modern 3D model were tested and improved, a new one-dimensional numerical model for cloud seeding experiments (1D

MCSE) was developed and performances of a novel aerosol at enhancing surface precipitation using the 1D MCSE model were tested. The novel aerosol is core/shell sodium chloride (NaCl)/titanium dioxide (TiO$_2$) nanostructure, also known as the shell structured TiO$_2$/NaCl. The introduced numerical model is a coupled dynamics of the Ćurić and Janc (1990) and Curić and Janc (1993a) 1D model with the Thompson and Eidhammer (2014) microphysics scheme. Two principally different approaches of numerically simulating the performances of the shell structured TiO$_2$/NaCl are utilized in this thesis. In the first approach the cloud droplet nucleation on the novel aerosols is evaluated via the lookup tables which were constructed by using the parcel model. The activation characteristics were modelled as function of ambient temperature, vertical velocity, relative humidity, the number of aerosols, and their chemical characteristics expressed by kappa parameter. In the second approach, the activation features of shell structured TiO$_2$/NaCl are explicitly resolved in the 1D MCSE model using the diffusion equation constructed from the laboratory experiments in cloud chambers with this novel aerosol. The performances of the novel aerosols were compared against the pure NaCl that has traditionally been used for precipitation enhancement, as well as against the base case without any seeding (i.e., cloud droplet nucleation only on the natural aerosols). In all analyzed cases, the novel aerosol shows profoundly better performances as precipitation enhancer than the pure NaCl. The superiority of this novel seeding material to pure NaCl is particularly noticeable in the unsaturated environments with the relative humidity below 75%. Analysis of spatiotemporal windows for these two artificial aerosols shows that the resulting precipitation enhancement from the shell structured TiO$_2$/NaCl is

more than 15% larger than using the pure NaCl and about 30% larger than in natural case.

Experiments with 1D MCSE model has yielded promising results in the field of precipitation enhancement with novel seeding material and this methodology was transferred to already improved and tested WRF-ARW model which led to new 3D MCSE model capable to simulate weather modification processes in realistic conditions. Results obtained with the new tool enabled detailed analysis of cloud seeding process in realistic conditions and enabled spatiotemporal analysis of precipitations. Precipitation enhancement results in 3D MCSE model are in agreement with 1D MCSE model obtained results. Precipitation footprint in the case of NaCl seeding and CSNT seeding is larger than in unseeded experiment. Precipitation increase due to seeding is not evenly distributed. The greatest increase is within light precipitations areas but increase in all categories is noticeable. Even NaCl and TiO_2/NaCl serves as CCN aerosols changes in cloud ice concentration due to seeding is observed. Cloud ice displacement is the main type of change.

Моделовање модификације падавина топлог и хладног типа

Резиме

Нумерички модели способни да симулирају процес модификације падавина, представљају моћан алат савремене цивилизације, који помаже научницима и лабораторијским истраживачима да утврде способност новопроизведеног реагенса да стимулише падавине. Нумерички модели омогућавају научницима да истраже какве карактеристике треба да има новопроизведени материјал како би позитивно утицао на процес модификације времена и добијени резултати могу одредити даља лабораторијска истраживања. Коришћење нумеричких модела је економски исплативије од спровођења експеримената са засејавањем у природи и омогућује да се уради неограничен број рачунских експеримената и анализа.

У овој тези представљена је нова шема за параметризацију олујног фронта, која има за циљ да побољша способност нумеричког модела Weather Research and Forecasting (WRF)–Advanced Research WRF (WRF–ARW) да симулира развој облака и процес формирања падавина. Утицај нове шеме на перформансе модела испитан је на примеру идеализованог суперћелијског облака у WRF моделу, као и проучавањем реалног случаја грмљавинске непогоде изнад Уједињених Арапских Емирата. У идеализованом случају, са укљученом параметризацијом олујног фронта у WRF моделу, формира се већа количина падавина и јавља се разлика у промени односа смеше облачне воде и односа смеше кишне воде са

временом, док су однос смеше леда и граупела остали непромијењени у поређењу са WRF моделом у којем није укључена параметризација олујног фронта. Примена параметризације није изменила опште карактеристике грмљавинског облака, као што су положај узлазне и силазне струје у облаку и облик облака. Форсирањем вертикалне брзине, које представља периодичне осцилације носа олујног фронта, у идеализованом и у реалном експерименту евидентирано је формирање нових конвективних ћелија испред олујног облака. Упркос разликама између симулација са WRF моделом и сателитских осматрања, укључивање шеме за параметризацију олујног фронта створило је више конвективне облачности, те довело до бољег слагања са осматрањима.

У овој студији приказана је анализа способности постојећих модела прогнозе времена да симулирају развој облака и процес формирања падавина за случај када су природни аеросоли експлицитно и имплицтно укључени у рачун. За ово истраживање одабран је мезоразмерни конвективни систем који се формирао изнад западних и централних делова Србије у поподневним часовима 21. јула 2014. године. Нумерички продукти модела са експлицитно третираним аеросолима (WRF-AE) и модела са имплицитно третираним аеросолима (WRF-AI), упоређени су са мерењима из мреже падавинсих станица, као и са радарским и сателитским осматрањима.

WRF-AE модел је добро симулирао транспорт прашине из северне Африке преко Медитерана и Балканског полуострва. Оба модела су изместила облак ка југозападу и дала мање максималне вредности композитне радарске рефлексивности у односу на осмотрене вредности.

VII

Слично сателитским сликама, WRF-AE модел приказује конвективни мезоразмерни систем као обједињен скуп кумулонимбусних облака. Из оба модела се добијају веће количину падавина од осмотрених; код WRF-AE модела је дошло до повећања у зони слабих падавина, док се код WRF-AI модела јавља повећање падавина у зони јачих падавина.

Након што су испитане могућности савременог 3D модела и након што је модел унапређен, развијен је нови једнодимензиони модел за спровођење експеримената засејавања облака (1D MCSE). Помоћу 1D MCSE модела испитана је способност новог реагенса да стимулише падавине. Нови реагенс је со (NaCl) премазана нано слојем титанијум диоксида (TiO_2) и у даљем тексту користи се ознака CSNT (core/shell sodium chloride (NaCl)/titanium dioxide (TiO_2)). Нови модел представља спој динамичког језгра модела Ћурић и Janc (1990) и Ћурић и Janc (1993a) и микрофизичке шеме Thompson и Eidhammer (2014). У овој тези су примењена два различита приступа нумеричког симулирања перформанси CSNT материјала. У првом приступу нуклеација облачних капљица на новом реагенсу рачуната је помоћу унапред израчунатих табела које су припремљене помоћу модела облачног делића. Активација је моделована као функција околне температуре, вертикалне брзине, релативне влаге, броја природних аеросола и хемијских карактеристика аеросола изражених преко к параметра. Код другог приступа, активирање CSNT у 1D моделу рачунато је користећи једначину дифузије која је конструисана на основу лабораторијских мерења спроведених у облачној комори. Резултати добијени употребом новог реагенса упоређени су са резултатима добијеним применом соли и са резултатима добијеним моделом без засејавања. У свим анализираним случајевима, нови

материјал је показао далеко боље перформансе него NaCl као средство за стимулацију падавина. Супериорност новог материјал у односу на NaCl је нарочито видљива у незасићеној средини при релативној влажности мањој од 75 %. Анализом просторних и временских прозора за два реагенса показано је да је CSNT дао 15 % веће падавине у односу на NaCl и 30 % веће падавине у односу на незасејану средину.

Експерименти са 1D MCSE моделом дали су обећавајуће резултате у области стимулисања падавина са новим материјалом и ова методологија је пренета у већ побољшани и тестирани WRF-ARW модел и тиме је добијен 3D MCSE модел који је способан да симулира процес модификације времена у реалним условима.

Резултати добијени са новим алатом омогућили су детаљну анализу процеса засејавања облака у реалним условима и анализу просторно временских прозора. Резултати стимулисања падавина добијени са 3D MCSE моделом су у сагласности са 1D MCSE моделом. Падавинска зона при употреби NaCl као материјала за засејавање и при употреби CSNT материјала је већа него у незасејаном експерименту. Повећање падавина услед засејавања није равномерно распоређено. Највише се повећају падавине у области слабих падавина, али је повећање и у осталим областима приметно. Иако NaCl и CSNT служе као језгра за нуклеацију облачних капљица промене у концентрацији облачног леда су приметне услед примене ових материјала. Најуочљивија промена је просторно измештање облачног леда.

Кључне речи: аеросоли, динамика облака, микрофизика облака, моделовање облака, ваздушни слапови, олујни фронт, падавине, грмљавина, модификација времена

Научна област: Геофизичка наука

Ужа научна област: Метеорологија

УДК број: 551.5 (043)

X

Table of contents

List of figures

List of tables

Abbreviations

CAPE	Convective Available Potential Energy
CCL	Convective Condensation Level
CCN	Cloud condensation nuclei
CSNT	Core/shell NaCl/TiO$_2$
ECMWF	European Centre for Medium-Range Weather Forecasts
EF	Enhanced Fujita Scale of the strength of tornadoes
EL	Equilibrium Level
GF	Gust front
GFS	Global Forecast System
GOCART	Goddard Chemistry Aerosol Radiation and Transport
IFS	Integrated Forecasting System
IN	Ice nuclei
LI	Lifted Index
LCL	Lifted Condensation Level
LFC	Level of Free Convection
MCS	Mesoscale Convective System
MCSE	Model for Cloud Seeding Experiments
MODIS	Moderate Resolution Imaging Spectroradiometer
NIFA	Number of ice-friendly aerosols
NWFA	Number of water-friendly aerosols
SEVIRI	Spinning Enhanced Visible & Infrared
SRH	Storm Relative Helicity
TT	Total Totals
WRF	Weather Research and Forecasting model
WRF-AE	WRF with aerosols explicitly included
WRF-AI	WRF with aerosols implicitly assumed

This page intentionally left blank

CHAPTER 1

1 Introduction

1.1 General introduction

The fact that we can simulate atmospheric processes with numerical models is of great scientific significance. Numerical models are used in everyday life, but they also play important role in scientific research because they help us to better understand fundamental meteorological processes. Successful forecast of rain is considered as one of the most important segments in weather forecast and is closely related to microphysical processes.

Unfortunately, we still cannot compute microphysical processes explicitly in weather forecast models because of high computation costs and great complexity of microphysical processes. Because of that, we approach to this problem with parametrizations. Two main types of parametrizations used in this field are bin and bulk parametrizations. In most 3D numerical models bulk methodology is used because it is less computationally intensive.

In bulk approach, size distributions for each individual category of hydrometeors is assumed. Main categories are cloud water, rain water, snow, graupel and cloud ice. Presence of individual category depends on actual temperature value so we can divide microphysical processes to cold and warm processes. If temperature is below 0° C, snow, graupel and ice can exist, but if temperature is above 0° C, only cloud water and rain water exists. Warm processes are simpler to calculate because there are less cloud categories and thus we have smaller number of interactions between categories.

For accurate parametrization of microphysical processes, it is important to describe process with correct equations, but it is also important to make good choice of required hydrometeor categories and to describe all important interactions between those categories. Most important microphysical processes are nucleation of cloud droplets, diffusional growth, process of collide and coalescence, drop breakup, evaporation, ice production and melting (Ćurić, 2001).

The atmospheric aerosols are small particles of size from 10^{-3} μm up to few centimeters. Their shape is irregular and most often we approximate them as spherical particles. Three theories about aerosols origin exists: cosmic, continental and oceanic. No matter how they come to atmosphere and how they were created (naturally or with unintentional human activity) we call them atmospheric aerosols. Unlike natural aerosols, particles which were created in laboratory in strictly defined conditions, and as such are introduced into atmosphere in a controlled manner we call seeding aerosols or reagent (Ćurić, 2001).

Aerosols have complex influence on clouds life and precipitation formation process. They serve as cloud condensation nuclei (CCN) and ice nuclei (IN) so presence of aerosols is important for formation of cloud droplets and ice crystals. Increase in number concentration of aerosols typical contributes to increase in number of small cloud droplets and that leads to increase in albedo value, which is known as the first indirect effect (Twomey, 1974). In addition, because of decrease of size of droplets in a cloud, it is possible to have delay in rain formation, or change in amount of precipitations which is known as second indirect effect (Twomey, 1974) and is explained in more details by (Tao et al., 2012; Thompson and Eidhammer, 2014).

Nucleation by cloud condensation nuclei and ice nuclei is called heterogeneous nucleation as it involves a foreign substance on which cloud water and ice water can form, compared to homogeneous nucleation, for which no foreign

substance is needed for nucleation. Heterogeneous nucleation of liquids can be a function of several variables, such as temperature, vapor pressure or supersaturation, pressure, and factors or activation coefficients related to the composition of aerosols involved. (Straka, 2009). There are four modes of heterogeneous nucleation of ice: deposition nucleation mode, condensation-freezing ice nucleation mode, contact nuclei mode and immersion mode. Heterogeneous nucleation is modelled using activation curves.

One typical distributions used is bulk methodology is Gamma distribution:

$$N(D) = N_0 D^\alpha e^{-\lambda D} \tag{1.1}$$

Parameters of the distribution N_0 and λ are slope intercept and slope of the distribution respectively. α is shape parameter of the distribution. Changes is cloud categories are described by change of distribution parameter values with time. We achieve this with prognostic equation for one or more parameters in the distribution. To calculate all three parameters, three prognostic equations are required and such model is called three-moment model. Calculation of three equations is expensive and in past most models were one or two-moment models. One approach to use three parameter gamma distribution in two-moment model is that parameter α value is being diagnosed based on values of N_0 and λ (Thompson et al., 2008). Murakami (Murakami, M., 1990) has shown that two-moment models can be used successfully in forecast of cloud top height, cloud height and we can accurately forecast time of start of precipitation formation at cloud base. Also first radar echo can be represented well in such models and hydrometeors are accurately located relative to upward current. He also got good results with forecast of cloud ice concentration.

1.2 Motivations and objectives

The main goal of this thesis is to better understand influence of natural and artificial aerosols on the process of formation of warm and cold type precipitations and to determine applicability of numerical models in rain

modification simulations. It is assumed that artificial aerosols are used as seeding material in rain modification experiments. Important step is to incorporate aerosols into microphysical processes. With usage of adequate parameterizations, we can describe influence of size distribution of aerosols, chemical composition of aerosols and their hygroscopicity on rain formation process. All those parameters play important role in process of nucleation.

The key point in research is to determine conditions in which new material can be used as cloud condensation nuclei or ice nuclei. It is expected to determine relationship between microphysical processes and cloud structure regards to cloud dynamics and to determine how are cloud droplets formed on CCN and IN and in which conditions seeding with artificial aerosols delays or prevents formation of raindrops. Most of the rain never reaches ground, but it is important to know what amount of water evaporate on the way to the ground and what is the influence of evaporation on thermodynamics of atmosphere.

It is important to know where to seed and what amount of seeding material is required to achieve expected results. This problem is known as spatiotemporal windows.

One of the goals of this thesis was to develop a 1D model for cloud seeding experiments and investigate the seeding performances of the shell structured $TiO_2/NaCl$ (novel) reagent in comparison with pure NaCl. The constructed model is expected to be capable of simulating droplet growth on the natural population of aerosols as well as on different seeding reagents. Moreover, it is expected that the model will give us possibility to study droplet activation and their sensitivity to external factors such as humidity, temperature and vertical velocity, as well as internal factors such as chemical characteristics of aerosols. In addition, the model would explore how hygroscopic seeding might affect the initiation of coalescence and the production of rain through the processes of autoconversion of cloud droplets, gravitational collection, rain self-collection, drop break-up, and evaporation.

The other goal was to develop a 3D model for cloud seeding experiments based on existing cloud and weather models. It is planned to incorporate knowledge and experience gained from 1D model and overcome well known disadvantages of 1D model like insufficiently detailed cloud dynamics and lack of spatial distribution of precipitations with development of 3D model. 3D model enable us to conduct experiments in realistic conditions and is meant to be best tool for this research. Without such a model, there is unthinkable further progress in this field.

This research should also point out what is the best way to incorporate aerosols in cloud droplet nucleation and evaporation processes, and in the processes of ice formation.

The final goal is to conduct experiments with 1D and 3D model with different environmental conditions and different seeding materials, to summarize the results and to give answers to the difficult and important questions.

1.3 Expected contributions

The methodology used to modify the precipitation of a warm and cold type used in this thesis should contribute to the study of cloud microphysics in general and to numerical modelling of clouds. This methodology is expected to show significance of the inclusion of aerosols in meteorological models. Results obtained in this thesis should help us to determine possibilities to modify rain formation process with artificial aerosols.

Accurate computation of rain formation processes on natural and seeding aerosols, gives us full insight, how great is the seeding contribution to precipitation formation from the point of view of chemical characteristics of seeding materials, amount of seeding material used, and the dependency of spatiotemporal windows in seeding process. With this research we gained a tool, which can be used to verify very exactly all those facts.

The world faces a lack of drinking water, and modern science tries to give its contribution to this issue. The usage of real aerosol data measured with modern satellites together with good quality weather data can help us to verify usability of modified microphysical scheme in real conditions. Simulations conducted with real data and artificial aerosols used as seeding material can show us the possibilities of rain enhancement for the purpose of usage in agriculture or usage in provision of drinking water. Provision of water by rain enhancement is inexhaustible and ecologically acceptable solution regards to other well-known processes like desalinization.

1.4 Organization of the thesis

This thesis is written in the "monograph" format as specified by the Faculty of Physics at the University of Belgrade.

Chapter 1 provides a general introduction to the topic of numerical modelling of warm and cold type rain modification. The expected outcomes and contributions of this research are also presented in this chapter. The next chapter contains the comprehensive literature review on numerical modelling of clouds and aerosols. Chapter 2 therefore documents the present state of knowledge in the field of weather modification and numerical modelling. Improvements added to the 3D model and capabilities of recent 3D models are described in Chapter 3. The same chapter describes experiments conducted to verify applicability of the chosen 3D model in this thesis. Chapter 4 explains process of construction and development of the 1D model and process of adaptation of 3D model for seeding experiments. The results obtained using 1D and 3D model for cloud seeding experiments are given in Chapter 5. Detailed analysis of the results of 1D model for two modelling approaches is given in the first section of this chapter, and detailed analysis of the results from 3D model for cloud seeding experiments is given in second section of this chapter. At the end, conclusions and recommendations for future research are provided in Chapter 6.

CHAPTER 2

2 Literature review

2.1 Gust front

For both a trained meteorologist as well as a layman, a sudden intensification of surface winds characterized by pronounced gustiness (and thunder) are well-known precursors of an approaching thunderstorm. These vigorous winds are known as the gust front. Gust fronts originate in the thunderstorm as a diabatically cooled air heavier than the surrounding air. Due to the negative buoyancy, this cold air starts descending from the base of the cloud in an impinging jet-like fashion known as a downburst (Fujita, 1985). Upon reaching the surface, the air spreads radially in a form of a starburst outflow, sometimes causing high intensity gusts that can be as large as 75 m s^{-1} (Fujita, 1981). Note that, for instance, these gusts correspond to velocities observed in EF3 tornadoes (almost an EF4), based on the Enhanced Fujita Scale of the strength of tornadoes (Wind Science and Engineering Centre, 2006). The leading edge of the starburst outflow is known as the gust front. Gust fronts can last for a couple of hours and their horizontal dimensions are of the order of dozens of kilometers. If a gust front passes over a weather station, its typical footprint in measurement records is characterized with: (1) a surface pressure jump, (2) an abrupt change in wind direction, (3) a sudden increase in wind, and (4) a decrease in temperature; in that order These facets together with the structure of the gust front are schematically portrayed in Figure 2.1.
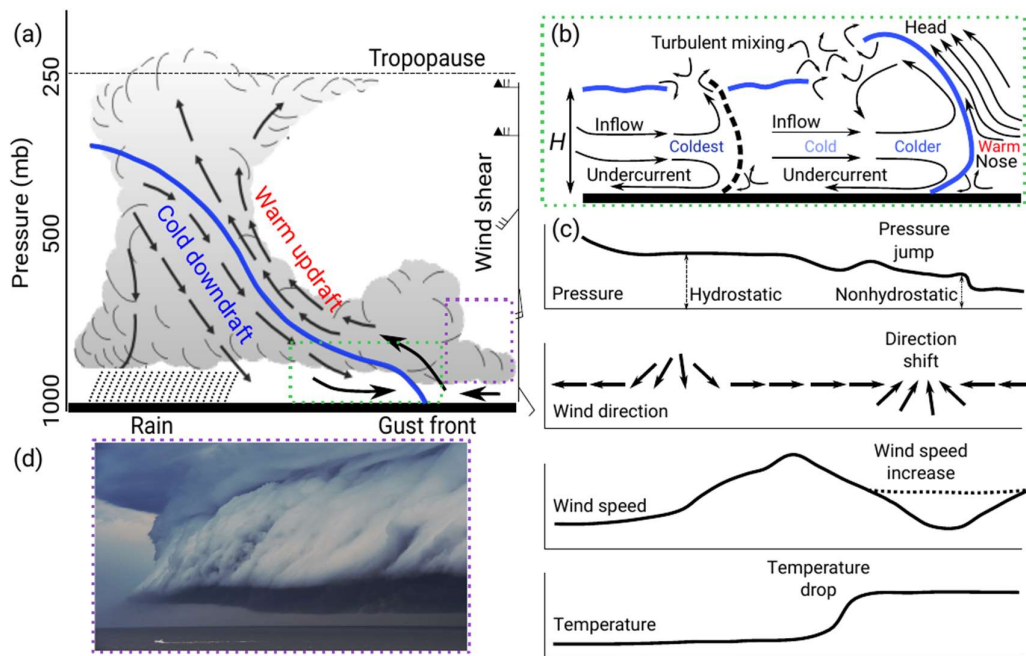
Figure 2.1 (a) Schematic mature cumulonimbus cloud with the main dynamics outlined. (b) Closer look at the gust front relative flow. (c) Changes in several surface meteorological parameters associated with a gust front passage. The schematics are not to scale; modified after Charba (1974); Wakimoto (1982); Mueller and Carbone (1987); Droegemeier and Wilhelmson (1987). (d) A photograph of shelf clouds overseeing a gust front in Australia (courtesy of Nick Moir, with permission).

The cold inflow from the parent storm cuts under warm air bringing it closer to the storm's main updraft, as shown in Figure 2.1a. This forced convection leads to a formation of arcus clouds appearing as a menacing-looking shelf cloud (Figure 2.1d). Strong turbulent mixing takes place in the wake region above the inflow current due to the Kelvin-Helmholtz instability (Britter and Simpson, 1978). Surface friction directly influences a layer approximately 20 m deep in the main current (Sherman, 1987) resulting in the smaller wind speeds close to the ground and the undercurrent backflow (Droegemeier and Wilhelmson, 1987). As a result, the leading edge takes a nose-like shape (Figure 2.1b) with the height of about 750 m above ground (Charba, 1974), but smaller values have also been observed (Goff, 1976). The sudden nonhydrostatic pressure increase is

due to the short lull caused at the boundary between the cold and warm air masses (Wakimoto, 1982). This brief calm, however, is not observed in all gust front records (e.g., Sherman, 1987; Järvi et al., 2007; Burlando et al., 2017) and according to Mahoney (1988) it occurs when the front propagates into the strong opposing winds (thus the dashed line in the wind speed graph in Figure 2.1c). The pressure minimum behind the gust front head is caused by dynamic effects of the pronounced turbulence mixing in that region (Droegemeier and Wilhelmson, 1987). The height above ground of the main inflow (H) is typically between 1000 m to 2000 m, with the height of the head being $\sim 2H$. This structure of gust front is similar with that of gravity currents (Simpson, 1969). The gust front evolution graphs similar to Figure 2.1c, but for the condensation of condensational nuclei, visibility and electric filed can be found in Williams et al. (2009).

Most of the analytical models and quantitative descriptions of gust front and downburst dynamics (e.g., Charba, 1974; Mueller and Carbone, 1987; Oseguera and Bowles, 1988; Vicroy, 1991; Holmes and Oliver, 2000; Chay et al., 2006) are based on either full scale measurements from weather stations, Doppler radars and tall meteorological towers (e.g., Fujita, 1976; 1985; Wakimoto, 1982; Hjelmfelt, 1988; Atkins and Wakimoto, 1991; Holmes et al., 2008; Pistotnik et al., 2011; De Gaetano et al., 2014; Gunter and Schroeder, 2015; Burlando et al., 2017) or physical experiments in wind tunnels (e.g., Simpson, 1969; Letchford and Chay, 2002; Xu and Hangan, 2008; McConville et al., 2009). Interestingly, though, a large number of analytical models as well as wind tunnel experiments are developed for analyzing gust fronts from a wind engineering point of view. This interest of wind engineering community in gust fronts is not surprising due to the observed damages that these severe weather events can inflict on man-made structures and environment. Their hazardous nature is particularly know for aircrafts that are in their landing and take-off stages of the flight. However, gust fronts also play a crucial role in the dynamics, precipitation formation, and lifecycle of the parent thunderstorm.

Some of the above-mentioned analytical models are based on the conservation of momentum and the continuity equations (Oseguera and Bowles, 1988; Vicroy, 1991; Holmes and Oliver, 2000; Chay et al., 2006) following the impinging jet models well established in fluid dynamics. The thermodynamics and, consequently, the energy aspects of gust front were not considered. However, being a buoyancy driven phenomena, these gust front facets should not be neglected. That is, accounting for the thermodynamic effects and surface friction reveals an important feature of the gust front nose—its pulsation in time (e.g., Simpson, 1972; Charba, 1974; Goff, 1975; Mitchell and Hovermale, 1977; Ćurić, 1977; 1980; Curić and Janc, 1993; Geerts et al., 2006). Namely, the faster main flow aloft the undercurrent propagates further into the warm air region (Figure 2.1c) and once the formed nose extends far beyond the warm air beneath, it collapses into the warmer air. Due to the act of surface friction (Ball, 1960), the whole process starts again, thus the cyclical occurrence of the nose. The idea of periodical collapse of the overhanging cold air was first introduced by Charba (1974) after analyzing several contradictory observational reports of the structure of leading edge of gust fronts. This proposal was latter discussed and observationally confirmed by Goff (1975, 1976), Droegemeier and Wilhelmson (1987), Ćurić et al. (2003) and Geerts et al. (2006), and numerically by Mitchell and Hovermale (1977). Moreover, Ćurić (1980), Ćurić and Janc (1987) and Ćurić et al. (2003) demonstrated that these periodic height changes of the gust front nose reflect as the periodic impulses of warm air in the main updraft and consequently may alter the precipitation pattern of the parent cloud. Similar rain periodicity pattern was also noticed by Park and Sikdar (1982) in their case study of a severe thunderstorm in Oklahoma, United States.

2.2 Natural CCN and IN aerosols

Numerical simulations of clouds and precipitation are sensitive to the choice of utilized microphysical scheme. Unfortunately, it is not a straightforward task to assess the accuracy of different schemes (Levin and Cotton, 2009). Ćurić and

Janc (2010) investigated differences between observed and modelled amounts of precipitation in flat and mountainous regions of the central-north and eastern Serbia. Using a few different size distributions of raindrop spectrum in their cloud-resolving model, they concluded that the Khrgian-Mazin size distribution provides the best matching between numerical results and observations in both flat and rugged regions. Kovačević and Ćurić (2013) performed a comparison of two microphysical schemes, one with and the other without hailstone embryos, and they showed the scheme with the embedded hailstone embryos gives better results, such as the time occurrence of hailstone and accumulation of hail on the ground. In a very recent paper, Kovačević and Ćurić (2015) demonstrated that the unified Khrgian-Mazin distribution is more accurate at modelling rain showers than the monodisperse Marshall-Palmer distribution. Efstathiou et al. (2013a) and Efstathiou et al. (2013b) tested the Weather Research and Forecasting (WRF) model at simulating an intense rainfall event over Chalkidiki, Greece, using few different cloud microphysics schemes and two different boundary layer schemes. They showed that performances of each scheme depend on the type of numerical product that is analyzed. For example, the Ferrier scheme was the best option for modelling the intense hourly precipitation rates, while the Purdue-Lin scheme accurately captured the locations of maximum rainfall. None of the above studies, however, investigated the impact of modelled aerosols on cloud dynamics and microphysics. Tao et al. (2012) in a review study reported that different aerosol treatments can result in large discrepancies between simulated precipitation rates. Interestingly, they concluded that the under- or over-predictions of modelled precipitations are not a general rule, but it rather varies from study to study.

An explicate inclusion of aerosols leads to the activation of limited number of aerosols as CCN and IN (Lim and Hong, 2009; Thompson and Eidhammer, 2014; hereafter TE14). That is, cloud droplet number concentration varies in contrast to implicitly modelled aerosols where this number is fixed constant,

such as in Thompson et al., 2008; hereafter T08. This approach enables direct prediction of the concentration of cloud water droplets, as well as the concentration numbers of activated aerosols that serve as CCN and IN. In the TE14 scheme, the concentration of activated CCNs depends on the in-cloud temperature, vertical velocity, the total number of available aerosols, as well as the two prescribed constants (hygroscopicity parameter and the mean radius). The activation rules are based on the results reported in the works by Feingold and Heymsfield (1992) and Eidhammer et al. (2009) and the activation is most sensitive on the total number of available aerosols and vertical velocity. When it comes to the ice phase, the number of mineral dust aerosols dictates the number of activated INs. It has been demonstrated that mineral dust is highly active IN with moderate concentrations in the atmosphere (Hoose et al. 2010; Murray et al. 2012).

TE14 tested the scheme for an idealized case of two-dimensional flow over a hill as well as for a winter cyclone above the continental United States. They noticed the aerosols had largest impacts in the zones of light precipitation. However, their sensitivity analysis could not distinctively determine which set of prescribed aerosol conditions produces the best match with observations; thus they stated that more research is need. Recently, Nugent et al. (2016) used the TE14 scheme to analyze six idealized cases of thermally driven orographic convection. Their study is limited to warm clouds and therefore the ice-phase microphysics was neglected. Thompson et al. (2016) coupled the TE14 scheme with the Rapid Radiative Transfer Model-Global scheme for radiation. Their analysis showed small differences between the effective radii and cloud optical depth calculated in the coupled and uncoupled cases. Similarly to TE14, they also recognized that more research is needed on this subject. It seems there is a general agreement in cloud modelling community that the "cloud-aware" aerosol schemes require more testing due to the novelty of this approach and the large complexity of numerous interactions between.

2.3 Cloud seeding with human made aerosols

Weather modification is one of the oldest branches of atmospheric sciences, as people have always wanted to tailor the weather for their needs. Some weather modifications are unintentional and happen as a by-product of everyday human activities such as the release of environmentally harmful gasses from vehicles and power plants or, for instance, modified wind flows due to the man-made structures on Earth's surface. The purpose of this thesis, however, is to investigate the subject of intentional weather modification in the form of cloud seeding. The modern era of weather modification dates back to the 1940s and the experimental work of Irving Langmuir and Vincent Schaefer in cloud chambers (Schaefer, 1946) and real environment through the Project Cirrus in 1947. Although their results to modify a hurricane at full scale were questionable, it sparked scientific interest for this important field of meteorology. Consequently, a number of field campaigns, cloud chamber experiments and numerical models kicked off with the main objective to investigate the efficiency of cloud seeding for precipitation enhancement or suspension. For detailed reviews on this subject, see Orville (1996), Bruintjes (1999) and more recently DeFelice and Axisa (2017). Precipitation enhancement by cloud seeding using numerical approach and a novel seeding reagent is investigated in this thesis. The subject of precipitation enhancement is of particular importance nowadays as the overall area with severe droughts increased from 8% to 14% in the period 2014–2015 (Blunden and Arndt, 2016). According to Zhao and Dai (2015), further increase of the frequency of droughts is expected on global level.

In numerical modelling, cloud physics is one of the most complex and time consuming modules of the model, but, at the same time, it is also one of the quintessential components of any numerical weather prediction (NWP) or cloud models (Khain et al., 2000). This complexity is due to the large number of processes between different cloud species whose concentrations vary in space

and time. Seeding a cloud with a reagent additionally increases the complexity of the system. The microphysics schemes that characterize these interactions are classified either as the bulk parameterization schemes or spectral bin schemes (Khain et al., 2015; Sarkadi et al., 2016). The bulk parameterization schemes use integral parameters to describe the size spectrum of hydrometeors, whereas the spectral bin schemes describe each of the species through the distribution functions that evolve through space and time.

The shell structured $TiO_2/NaCl$ is a novel cloud seeding aerosol recently developed and tested by Tai et al. (2017) (hereafter T17). Some of the well-known and frequently utilized seeding materials are NaCl (e.g., Thaveau et al., 1987; Sorjamaa et al., 2004; Kristensen et al., 2014; Neukermans et al., 2014), dry ice (i.e., solid form of carbon dioxide, CO_2) (e.g., Schaefer, 1946; Huggins and Rodi, 1985; Mertes et al., 2001; French et al., 2018), and silver iodide (AgI) (e.g., Vonnegut, 1947; Ćurić and Janc, 1990; Ćurić and Janc, 1993b; Dessens et al., 2016; Vujović and Protić, 2017). A number of other seeding materials has also been used in different experiments (e.g., Mather et al., 1997; Seo et al., 2012; Drofa et al., 2013; Reuge et al., 2016). NaCl is typically employed as a seeding material in warm clouds, whereas dry ice is used for the seeding of cold clouds. Previously, coating of NaCl with a condensing vapor of zinc chloride ($ZnCl_2$) was proposed by Alonso and Alguacil (2006). Despite being very hygroscopic substance, $ZnCl_2$ is also associated with a number of environmentally harmful characteristics (Rohe et al., 2014). When it comes to the shell structured $TiO_2/NaCl$, T17 demonstrated that this substance absorbs more water vapor than NaCl—in particular at low relative humidity which makes it very favorable substance for precipitation enhancement applications. The superior performances of the shell structured $TiO_2/NaCl$ over pure NaCl are due to the combined effects of the hydrophilic TiO_2 shell and hygroscopic NaCl core microstructure. As concluded in the T17 paper, this novel seeding material deserved further investigation as a rain-enhancement reagent. The present study is a step forward in that direction.

In general, the hygroscopic seeding of convective clouds is achieved through one, or a combination, of the following three concepts (Drofa et al., 2010). First, the cloud can be seeded with CCNs whose diameters are larger than 10 µm. In this case, those giant CCNs directly serve as embryos for raindrops. The second approach is to use CCNs with the diameter in the interval 1–10 µm in order to increase the concentration of large droplets, which in turn enhances the formation of raindrops (Segal et al., 2004). The third methodology is to increase the competition for available water vapor by seeding the cloud with CCNs whose diameter is around 1 µm. As discussed in Drofa et al. (2010) and Cooper et al. (1997), this seeding approach tends to increase the rate at which large drops coalesce into rain drops by decreasing the overall number of cloud drops and consequently increasing the size of the largest drops.

2.4 Literature review summary

The overall conclusions of the literature review can be summarized as follows:

- Gust front originate in the thunderstorm and can last for a couple of hours and its horizontal dimensions are of the order of dozens of kilometers.

- Periodic height changes of the gust front nose reflect as the periodic impulses of warm air in the main updraft and consequently may alter the precipitation pattern of the parent cloud.

- An explicate inclusion of aerosols leads to the activation of limited number of aerosols as CCN and IN and cloud droplet number concentration varies in contrast to implicitly modelled aerosols where this number is fixed constant.

- "Cloud-aware" aerosol schemes require more testing due to the novelty of this approach.

- People have always wanted to tailor the weather for their needs and seeding a cloud with a reagent additionally increases the complexity of the numerical model.

- Some of the well-known and frequently utilized seeding materials are NaCl, dry ice and silver iodide. The shell structured $TiO_2/NaCl$ is a novel cloud seeding aerosol recently developed.

CHAPTER 3

3 Improvements to WRF-ARW/MCSE model and capabilities of recent models

It was necessary to choose modern numerical model which will be capable to simulate cloud development and accurately forecast precipitations. WRF model was chosen and we made choice to use Advanced Research WRF (ARW) variant of the model and to incorporate into it natural and human made aerosols. Testing of the chosen model was done to verify its capabilities to simulate detailed cloud dynamics and cloud microphysics and to determine where improvements can be made.

3.1 Gust front

3.1.1   Gust front pulsation model

One of the significant phenomena related to strong thunderstorm clouds is gust front. It is well known that gust front phenomena are associated with severe winds, which are of great importance in theoretical meteorology, weather forecasting, cloud dynamics and precipitation, and wind engineering. An important feature of gust fronts demonstrated through both theoretical and observational studies is the periodic collapse and rebuild of the gust front head. This cyclic behavior of gust fronts results in periodic forcing of vertical velocity ahead of the parent thunderstorm, which consequently influences the storm dynamics and microphysics.

The decision was made to improve the existing numerical model with development of the new gust front pulsation parameterization scheme. Numerical weather prediction models, such as the WRF-ARW, do not account

for this periodic height changes of the gust front nose. The existence of gust fronts in WRF simulations is documented in many studies (Del Genio et al., 2012; Csirmaz et al., 2013; Abulikemu et al., 2016; Lompar et al., 2017) but none of them reported a period collapse of the nose. Observations, however, indicate that these cyclic collapses occur in nature.

The influence of this new scheme on model performances is tested through investigation of the characteristics of an idealized supercell cumulonimbus cloud, as well as studying a real case of thunderstorms.

Motivated by this discrepancy between numerical simulations and full scale measurements of gust front characteristics, the two main objectives behind this scheme are: (1) to implement a simple analytical model of the periodic height changes of the gust front nose in WRF–ARW, and (2) to test the added scheme for one idealized and one real case. The study aims to show to what extent, if any, this more realistic treatment of gust front nose influences the simulated cloud dynamics, precipitation and ultimately the forecast accuracy of the WRF–ARW model.

The nose of gust front exhibits periodic collapses. Ćurić (1980), Ćurić and Janc (1987), Curić and Janc (1993) and Ćurić et al. (2003) showed using theoretical derivations, a cloud model, as well as observations of a cumulonimbus (Cb) cloud along a river valley in Serbia that these episodic height changes of the gust front nose reflect as periodic changes of the vertical velocity of warm air that is forced to rise along the gust front head. A scheme of the cold air outflow below Cb base and spreading of the gust front head as a function of time (t) are shown in Figure 3.1a.

This periodic forcing of vertical velocity (w_f) can be expressed as the positive branch of a sinusoidal curve with the following shape (Ćurić and Janc, 1987; Curić and Janc, 1993):

$$w_f = W_0 \sin\left(\pi \frac{t - t_0}{\tau_0}\right), \tag{3.1}$$

where W_0 is the amplitude of w_f, t_0 is the initiation time of the forcing, and τ_0 is the duration of the forcing. That is, the forcing starts at the time t_0 and lasts until $t_0 + \tau_0$, when it stops. It is easy to show that w_f reaches the maximum when $t = t_0 + (\tau_0/2)$. The forcing ceases to exist in the time period between $t_0 + \tau_0$ and $t_0 + 2\tau_0$, after which it starts again and lasts until $t_0 + 3\tau_0$, and so on, as shown in Figure 3.1b.
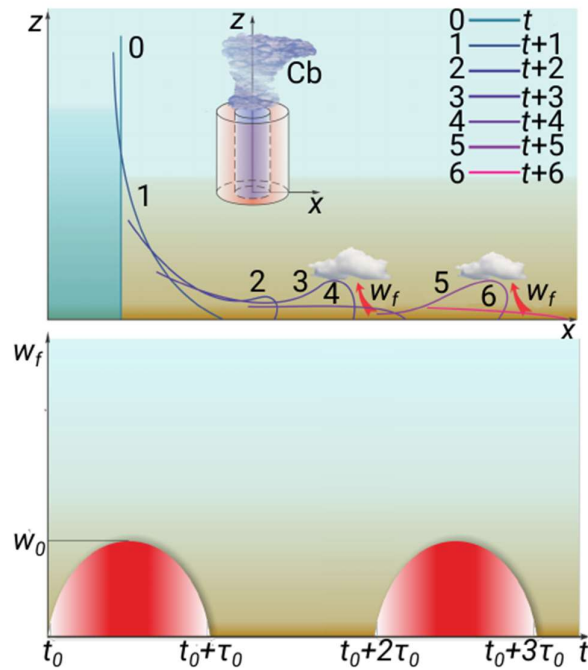
Figure 3.1 (a) Schematic representation of the downburst below Cb and gust front as a function of time (t). Locations of the maximum forced vertical velocity (w_f) are shown with the red arrows. (b) Forced vertical velocity as the function of time.

The values of W_0 and τ_0 are taken as constants throughout the numerical simulations and equal to $W_0 = 2$ m s^{-1} in the idealized case, $W_0 = 6$ m s^{-1} in the real case, whereas $\tau_0 = 20$ min for both cases. The initiation time t_0, is the time when precipitation from the parent cloud reaches the surface. The implementation of the above concept and Eq. (3.1) into the WRF–ARW model are achieved in three steps each described below.
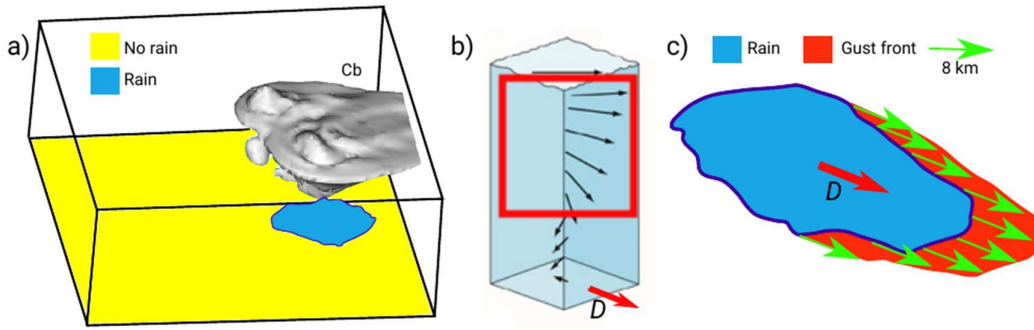
Figure 3.2 (a) A rendered view of Cb cloud in the idealized WRF-ARW computational domain with the schematics of precipitation zone underneath the cloud. (b) Representation of wind shear outside of the cloud with D indicating the mean direction of Cb cloud propagation [Eq. (4b)]. (c) The extent of gust front is 8 km ahead of the precipitation zone in the direction of the storm movement.

The first step is to determine the surface precipitation area below the Cb cloud. Figure 3.2a is a rendered view of cloud and associated precipitation zone underneath defined through the rain mixing ratio (q_r). In this approach, for each grid point in the horizontal plane (i, j) in the lowest $N = 8$ levels from the surface, the model is adding up the q_r values, and if:

$$\sum_{k=1}^{N} q_{r,k} > 0, \tag{3.2}$$

then the considered grid point on the surface is in the rain zone. The decision for using eight lowest model levels instead of the lowest level alone is driven by the nature of the gust front origin in Cb clouds. Namely, evaporation of liquid and solid hydrometeors below the zero isotherm, as well as the drag due the precipitation are the main downburst drivers, which upon reaching the surface spreads horizontally resulting in the gust front. For example, the rain droplets that do not reach the surface but instead evaporate in the layer between the cloud and surface will decrease air temperature of that layer and augment the downburst descent (Proctor, 1988). Similarly, melting of ice, hail in particular, seem to be an important factor in downburst formation (Wakimoto and Bringi, 1988).

The second step is to estimate the movement velocity of the Cb cloud. Here, the storm propagation is calculated as the mean wind speed and the mean wind direction outside of the cloud in the layer between the half of the atmosphere and the upper 3/4 of the atmosphere in the WRF–ARW model, as shown in Figure 3.2b. A lot of research has been conducted on predicting the thunderstorm motion (e.g., Newton and Fankhauser, 1964; 1975; Maddox, 1976; Bunkers et al., 2000) and these empirical methods are based on observations mostly performed in North America. This study uses a simple approach to estimate the storm motion similar to the one proposed by Maddox (1976). In the mathematical form, the mean zonal wind component ($\bar{u}$) and the mean meridional wind component ($\bar{v}$) in a grid point (i, j) are calculated as:

$$\bar{u}(i,j) = \frac{1}{k_{3/4} - k_h + 1} \sum_{k=k_h}^{k_{3/4}} u_k(i,j), \tag{3.3a}$$

$$\bar{v}(i,j) = \frac{1}{k_{3/4} - k_h + 1} \sum_{k=k_h}^{k_{3/4}} v_k(i,j). \tag{3.3b}$$

Here, k_h and $k_{3/4}$ are the vertical levels at the half of the atmosphere and at the upper 3/4 of the atmosphere in the WRF–ARW model, respectively. The mean wind speed (V) and the mean wind direction (D) of the storm propagation are then computed as, respectively:

$$V(i,j) = \sqrt{\bar{u}^2(i,j) + \bar{v}^2(i,j)}, \tag{3.4a}$$

$$D(i,j) = \frac{180}{\pi}\left(2 \cdot \arctan\left(\frac{V(i,j) - \bar{v}(i,j)}{\bar{u}(i,j)}\right) + \pi\right). \tag{3.4b}$$

More advanced, but also more computationally demanding methods such as the one proposed by Bunkers et al. (2000), could be implemented in the future work.

The third and last step is to determine the extent of the gust front ahead of the parent Cb cloud. The implemented procedure in this thesis follows the work by

Tompkins (2001), who showed that the cold pools of air spread out to between 3 km and 18 km with the mean value being around 8 km from the cloud. Therefore, our model assumes the extent of the gust front is 8 km in the direction *D* ahead of the precipitation zone as schematically depicted in Figure 3.2c. The implementation of Eq. (3.1) is at the border between the cold outflow and the surrounding air in the lowest eight levels in the WRF–ARW domain. Finally, the total vertical velocity (w_t) is given as:

$$w_t = w_b + w_f, \qquad\qquad (3.5)$$

where w_b is the background vertical velocity calculated solving the non-hydrostatic vertical momentum equation in the WRF–ARW model (Skamarock et al., 2008). The above-described method is included in the WRF–ARW model as a special option of cumulus parameterization. Namely, when this option is specified in the WRF namelist, the standard cumulus parameterization must be turned off and the only cumulus-related parameterization is the gust front nose pulsation specified by Eq. (3.1) and the above-described procedure.

3.1.2   WRF–ARW configurations

The WRF–ARW settings for both idealized and real cases are given in Table 1. The idealized three-dimensional quarter-circle shear supercell simulation is a present option for the WRF–ARW model (Skamarock et al., 2008; Morrison and Milbrandt, 2010; Kalina et al., 2014; Zhao et al., 2015). The model is run on a domain of size 160×160×20 km with the vertical resolution of 500 m. The horizontal resolution is 2 km with the open boundary conditions (i.e., gravity-wave radiation conditions) and top of the model is a constant pressure surface. Vertical profiles of potential temperature and water vapor mixing ratio are adopted from the studies of Weisman and Klemp (1982, 1984, 1986). In their sounding (Figure 3.3), the surface water vapor mixing ratio is 14 g kg^{-1} (results in CAPE ~2200 m^2 s^{-2}). The horizontal and vertical radii of perturbation that kicks off convection are 10 km and 1.5 km, respectively, with the maximum amplitude of the perturbation set to 3 K in the center of the thermal bubble.
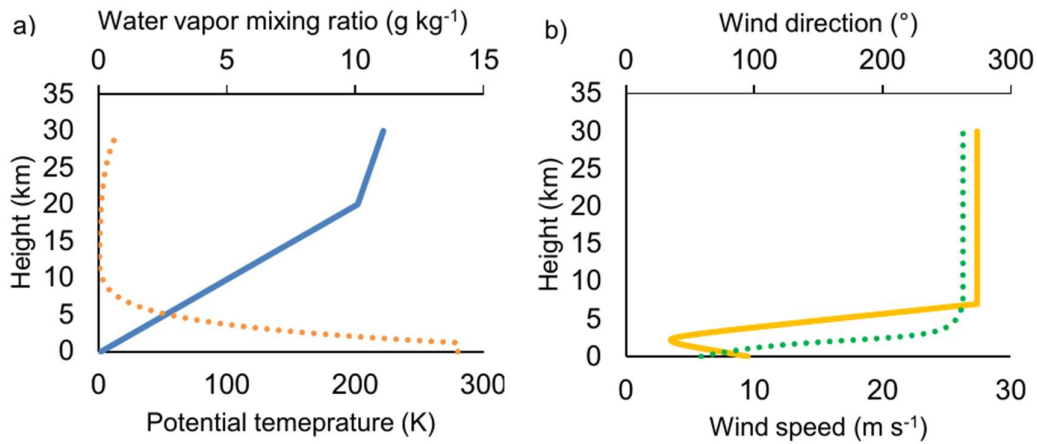
Figure 3.3 (a) Vertical profiles of potential temperature (full line) and water vapor mixing ratio (dotted line) in the idealized case. (b) Vertical profiles of wind speed (full line) and wind direction (dotted line) in the idealized case.

The profiles of potential temperature and water vapor mixing ratio are provided in Figure 3.3a. The quarter-circle wind shear favors the right moving growth of new cells with the wind direction shear being quasi-constant in the first ~5 km and zero aloft (i.e., constant wind direction) (Figure 3.3b). The wind speed profile in the idealized case is given in Figure 3.3b. It can be seen the wind speed becomes constant at the height of 7 km above surface (27.2 m s^{-1}). Lastly, the Coriolis terms in the idealized case are off and the simulation was run for 2 h of integration time.

Table 1 WRF-ARW configurations used for ideal and real cases. Note that although cumulus convection is turned off, the parameterization of the gust front nose pulsation in time is turned on in both cases.

	Idealized case	Real case
Microphysics	Thompson et al. (2008)	Thompson and Eidhammer (2014)
Longwave radiation	RRTM (Mlawer et al., 1997)	
Shortwave radiation	Dudhia (1989)	
Surface layer	–	MM5 Similarity Scheme
Land surface	–	Unified Noah Land Surface Model (Ek et al., 2003)

		Yonsei University Scheme (Hong et al., 2006)
Planetary boundary layer	–	
Cumulus convection	–	
Horizontal resolutions (km)	2	3, 1
Time step (s)	12	20
Number of vertical levels	41	64
Start time	–	17 July 2009 (00:00 UTC)
End time	–	18 July 2009 (00:00 UTC)

The WRF–ARW domains in the real case are positioned over the UAE and surrounding countries as shown in Figure 3.4. The initial and boundary conditions are obtained from the global Integrated Forecasting System (IFS) model with 0.25°×0.25° (~25×27 km) horizontal resolution, which is the operational model at the European Centre for Medium-Range Weather Forecasts (ECMWF). Two justifications for leaping from ~25 km resolution of lateral conditions to 3 km resolution in the WRF domain d1 (Figure 3.4) are the following. Objective is to test the parameterization of the gust front nose pulsation scheme and therefore the parameterization of cumulus convection had to be turned off. However, preserving a recommended 3:1 scaling from the lateral conditions would result in an additional domain with the horizontal resolution of ~9 km, which, in turn, would require the cumulus parameterization to be set on. Changes of physical packages from one domain to another are generally not recommended procedure in WRF. It should be noted that a jump from ~25 km to 3 km is not too far off the 1:5 scaling, which is also a recommended setting in WRF simulations. Secondly, the weather situation on 17 July 2009 in the that geographical region was characterized with the pronounced westward to northwestward movement of air from the Gulf of Oman and Arabian Sea (Figure 3.4) and therefore the finest resolution domain d2 (Figure 3.4) is far away from the east and south boundaries of d1 where the transition from ~25 km to 3 km spacing is the most noticeable.
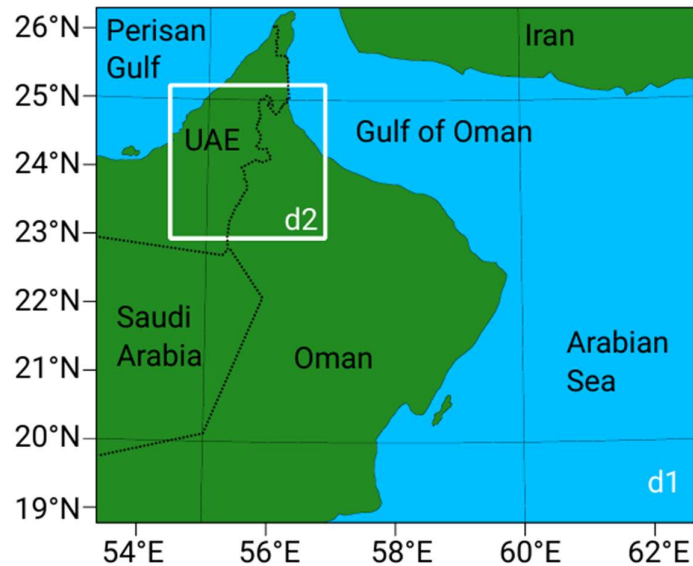
Figure 3.4 WRF-ARW domains d1 and d2 used in this study. Location of the meteorological radar at Al Dhafra Air Force Base in UAE indicated with the red dot.

The convection that is investigated in the real case started around 11:00 UTC (17 July 2009) and the first 6 h of simulation represent a spinup period. Integration time step in the largest domain was 20 s, with the exception of the acoustic modes for which the time step was 5 s. The Runge-Kutta 3rd order approximation using a predictor-corrector formulation is used to advance solution in time. The advections of momentum and scalars are the 5th order in horizontal and the 3rd order in vertical directions. Lastly, this simulation uses the 2nd order diffusion on coordinate surfaces.

3.1.3 Idealized supercell case validation

Figure 3.5 shows the time evolution of the idealized supercell Cb cloud without (top rows) and with (bottom rows) the gust front head pulsation parameterization. The isolines of mixing ratios are selected subjectively in order to depict the proper shape of a Cb cloud. The included forcing of vertical velocity has an impact on cloud dynamics in all stages of cloud development and the influence on precipitation increases with time. Development of new cells and their growth in the case of parameterized gust front are clearly

depicted throughout the cloud lifetime. In first 30 min (Figure 3.5e), the newly spawned cells are small and fairly scattered ahead of the main Cb cloud.
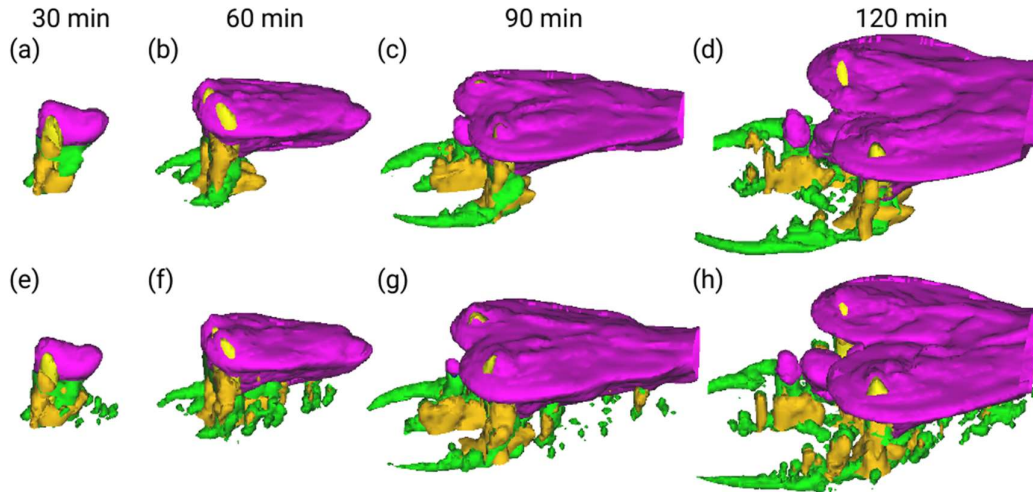
Figure 3.5 Supercell development without (top row) and with (bottom row) the gust front pulsation scheme. The colors represent the mixing ratios of snow (purple, 8×10^{-2} g kg-1), graupel (yellow, 4.5 g kg-1), rain (orange, 5×10^{-1} g kg-1), and cloud water (green, 5×10^{-2} g kg-1). The cloud ice (blue, 4×10^{-2} g kg-1) is not visible in this figure due to being encapsulated in cloud snow.

Even at that early stage the forcing seem to alter the precipitation region in the front part of Cb. The vertical structure of the main precipitation zone in the back flank of Cb, however, seem to be intact at this time. After 60 min, the cells have grew, merged and connected with the parent cloud creating the flanking line (Figure 3.5f). The development of yet another cell is also evident far ahead of the Cb cloud and underneath its anvil-like top (purple color). In the last two stages (i.e., after 90 min and 120 min), the difference between these two cases also becomes visible in the side flanks of the thunderstorm (Figure 3.5g,h). Namely, besides influencing the precipitation and cloud dynamics in the front part of Cb, the parameterization of gust front seems to alter the precipitation in the side flanks as well, as shown in Figure 3.5g,h. The increase of precipitation amounts after 90 min and 120 min in the right flank of the Cb cloud with gust front being parameterized is apparent. The main precipitation zones in the rear

flank of the cloud as well as the anvil-like top of the cloud, however, are not greatly influenced by the inclusion of the gust front pulsation parameterization scheme.
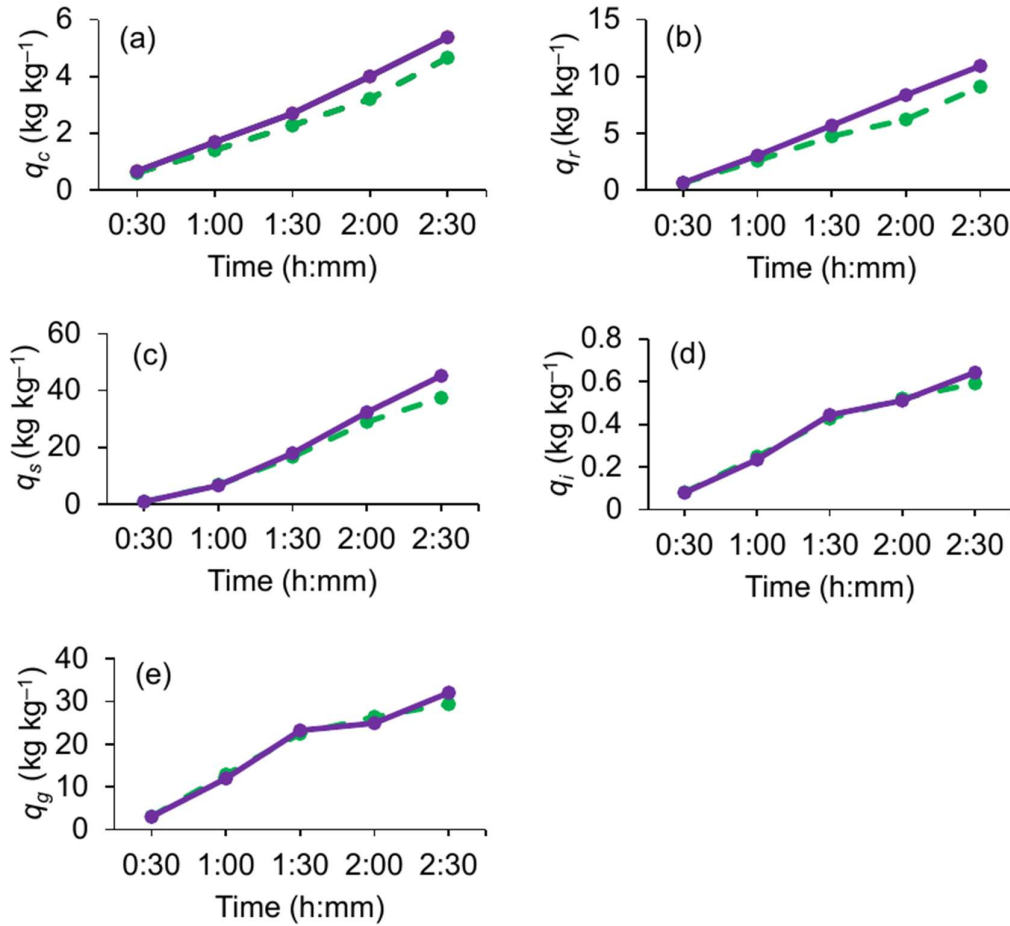
Figure 3.6 Time evolution of mixing ratios of (a) cloud water, (b) rain, (c) snow, (d) ice, and (e) graupel. The full purple lines represent the WRF run with the gust front pulsation parameterization on, while the dashed green lines are the case when the scheme is turned off.

Figure 3.6 is a quantitative analysis of what is going on in Figure 3.5. The time evolutions of all five mixing ratios are shown with the same 30 min time increment that was used in Figure 3.5. It can be seen that the inclusion of the gust front parameterization scheme (full lines in Figure 3.6) has the largest influence on the mixing ratios of cloud water (q_c) and rain (q_r), and to a lesser

extent to snow (q_s). While the divergences between q_c's and q_r's are already noticeable after the first hour (Figure 3.6a,b), the differences between q_s's start to arise after 2 h in simulation (Figure 3.6c). On the other hand, the discrepancies between the mixing ratios of ice (q_i) and graupel (q_g) in the two analyzed cases are very small (Figure 3.6d,e). Note that all mixing ratios are larger in the case when the gust front is parameterized. This latter observation is expected since the periodic forcing of vertical velocity ahead of Cb brings more moisture into the cloud.
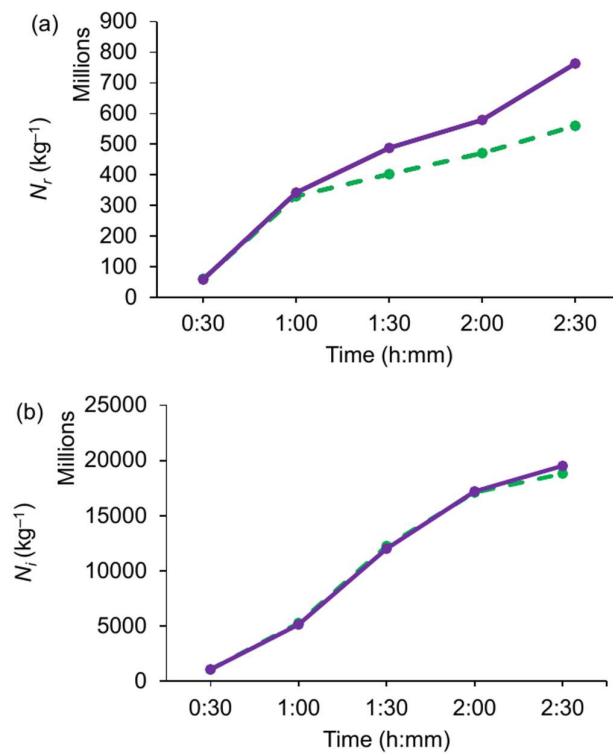
Figure 3.7 Time evolution of concentrations of (a) rain, and (b) ice. The lines color scheme asin Figure 3.6.

The physical explanation of why this additional moisture is mostly reflected as the difference in the mixing ratios of liquid hydrometeors (i.e., q_c and q_r in Figure 3.5a,b, respectively) deserves a deeper examination. The additional influx of moist air in the case of parameterized gust front results in more water vapor and q_c in the cloud. Knowing that the riming and collision are the

dominant processes in the formation of rain in mixed clouds (Pruppacher and Klet, 2010), and since q_r increased in the case with gust front, it is logical to conclude that the gust front parameterization scheme amplifies the effectiveness of these two processes. Since the efficiency of both riming and collision is proportional to the size and concentration of hydrometeors, as well as taking into account that q_i's and q_g's are unchanged between the runs, it follows that the concentration of raindrops (N_r) increased in the case when the gust front is parameterized. This result is further demonstrated in Figure 3.7a. Simultaneous increase of q_r and N_r shows that the number of small raindrops markedly increased in the parameterized case since the increase of N_r is several orders of magnitude larger than the increase of q_r. It seems the introduced parameterization of gust front dominantly influences the liquid and vapor phases, whereas the solid water phase stays unchanged. Namely, similar to q_i's, the concentrations of cloud ice (N_i) are also unaltered between the two runs as shown in Figure 3.7b. The ice phase in the cloud is located in the upper regions of Cb and since the included forcing of vertical velocity is limited to the lower part of the atmosphere, it is somewhat logical to expect that the liquid phase will be more affected by the introduced parameterization.

The influence of parameterization of gust front pulsation on accumulated surface precipitation from the idealized Cb cloud is demonstrated in Figure 3.8. Several differences between the two cases are worth pointing out. The edge of precipitation zone in the parameterized case (Figure 3.8b) is choppier than without the gust front (Figure 3.8a). This feature in probably caused by the development of additional cumuliform cells ahead of the parent Cb in the parameterized case (see also bottom row in Figure 3.5), which after merging with the parent cloud disturb the ideal and smooth shape of precipitation footprint underneath. Similar differences between the two cases are observed for the contours within the precipitation zone. The areas characterized with heavy precipitation (green and dark green colors in Figure 3.8) have the same

overall orientation in both runs, but their structures differ. Namely, they appear in patches in the case when gust front is parameterized, and, once again, the smooth shape and high degree of symmetry between the left and right flanks are lost.
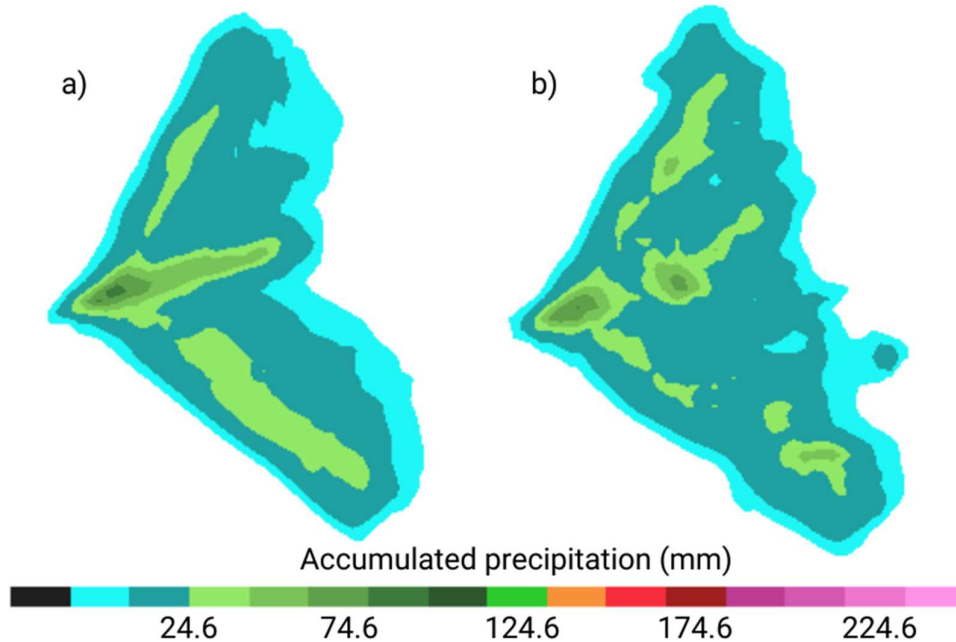
Figure 3.8 Accumulated surface precipitation over the whole simulation period without (a) and with (b) the gust front pulsation scheme.

The parameterized gust front case also shows the existence of two zones of the strongest precipitation displaced along the line of cloud propagation. This pattern is likewise evident as the filling of the concave area of precipitation-free zone at the leading edge of the Cb cloud in Figure 3.8a—namely, the same zone does not exist in Figure 3.8b. In other words, the precipitation footprint in Figure 3.8b has a triangular shape whereas its shape in Figure 3.8a is heart-like. The zones of heavy precipitation in the side flanks of the Cb cloud with included gust front scheme are in accordance with Figure 3.5. Note, however, that precipitation in the far peripheral regions started in the later stages of cloud

life (after ~90 min as demonstrated in Figure 3.5c,g). The strong precipitation areas along the central line and the rear flanks of the storm are in accordance with the splitting mechanism in Cb clouds (Wilhelmson and Klemp, 1978). The inclusion of the gust front scheme also gives rise to small irregularities in the overall shape of the precipitation footprint, as it can be observed in the lower-right corner in Figure 3.8b. The periodic amplifications of the total vertical velocity ahead of the cloud [Eq. (3.5)] in combination with the overall non-linear dynamics of a Cb cloud are probably the main contributors for the observed choppiness and different irregularities of the precipitation footprint in the case when the gust front is parameterized. Lastly, it should be noted here that the precipitation footprints in real thunderstorms do not show these highly idealized patterns (Lompar et al., 2017) due to the influence of many environmental factors that are not considered in these two simulations (e.g., land cover, orography, realistic initial conditions).
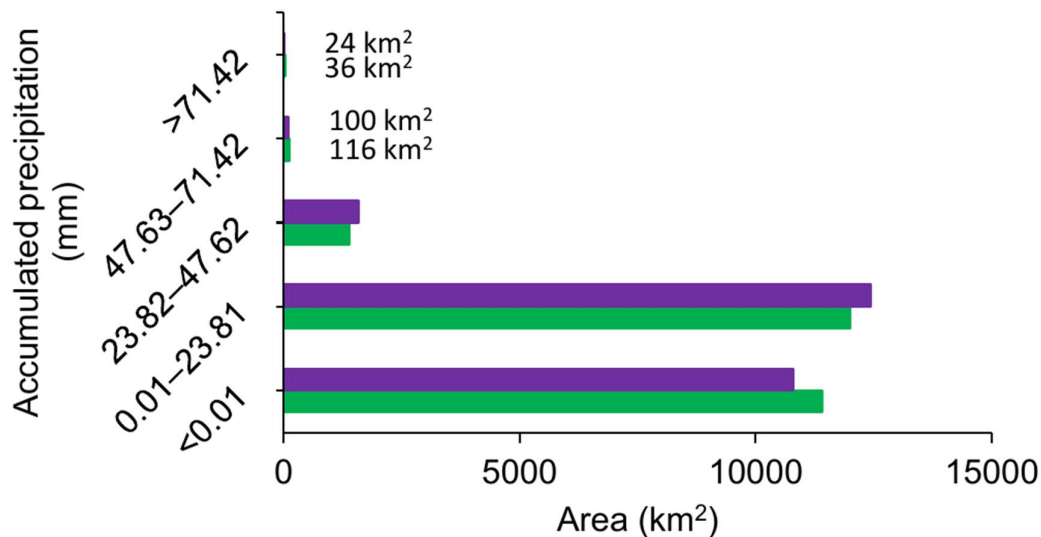
Figure 3.9 Histogram of different precipitation amounts in the case with the parameterized gust front (purple bars) and the default run without gust front (green bars).

Further quantitative analysis of Figure 3.8 shows that the run with parameterized gust front produced more precipitation. Over 2.5 h of simulated

time, the accumulated surface precipitation in Figure 3.8a is 25,202.6 litres (L) and 27,676.8 L in Figure 3.8b. That is, the inclusion of gust front scheme increased the surface precipitation for 9.8%. This increase, however, is not evenly distributed through all precipitation regimes as demonstrated in Figure 3.9. First, the presented results show that the precipitation footprint in the case when the gust front is parameterized is larger than without it (the precipitation-free area in the former case is smaller for 612 km^2). Within the precipitation zones, the light and moderate precipitations (below 23.81 mm and 23.82–71.42 mm) are larger in the case with the parameterized gust front for 456 km^2 and 184 km^2, respectively.. The areas with heavy precipitation are similar in size, but the simulation without gust front slightly spreads the heavy precipitation over larger areas. This result is particularly interesting in the light of several recent studies by Lompar et al. (2017), Thompson and Eidhammer (2014), Sorooshian et al. (2010) and Qian et al. (2009), who showed that the microphysics schemes with explicate treatment of aerosols tend to underestimate the light precipitation. The results presented herein indicate that the parameterization of the gust front pulsation couples nicely with the explicit modelling of aerosols in the WRF–ARW model in terms of increasing the precipitation amounts in the areas with light rain. However, more research is needed to confirm this hypothesis since the analyzed case represents a highly idealized situation.

Figure 3.10 shows the vertical cross-section of the idealized Cb cloud after 90 min of simulation time in both cases. While the overall features of the cloud look the same, the inclusion of gust front parameterization widened the updraft (around 1.5 times wider in the parameterized case at the level of the anvil back-shear). Similarly, the lower parts of the updraft seem to be augmented as well. Consequently, the downdrafts below the updraft (rear flank downdraft) and on the right side of the updraft (forward flank downdraft) are amplified. The region of vertical velocities above 8 m s^{-1} ahead of Cb in Figure 3.10b is a direct consequence of the introduced forcing. As a result, a small cloud cell can be

seen in front of the parent Cb cloud in the zone of shelf clouds. As discussed above, the inclusion of the gust front parametrization scheme altered the updraft and the dynamics of cloud top, but the mixing ratios of the ice phase (Figure 3.6) have small discrepancies between the two runs. Significant differences between q_s's, q_i's and q_g's are noticeable only in the last 30 min of simulations.
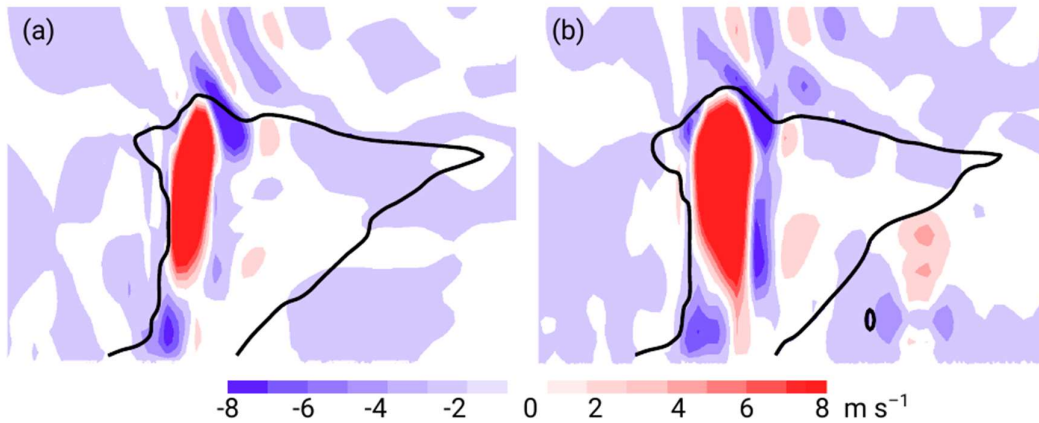
Figure 3.10 A vertical slice of Cb cloud (a) without and (b) with the gust front parameterization scheme at t = 90 min. Cloud edges indicated with the thick black line.

The cloud dynamics portrayed in Figure 3.10 shows the typical layout of updrafts and downdrafts in a supercell Cb (e.g., Cotton et al., 2010). However, since the cross-section is in a two-dimensional plain, the three-dimensionality of the rotating updraft (i.e., meso-cyclone) due to the environmental wind shear cannot be depicted. The rear flank downdraft is located in the back of the cloud and it is less pronounced than the forward flank downdraft. The anvil back-shear and the flanking line at the lower base of Cb extend approximately the same length in the rear direction from the overshooting top and the updraft. The stronger forward flank downdraft together with the amplified updraft (Figure 3.10b) explain more precipitation in the parameterized case (Figures 3.8b and 3.9) from the cloud dynamics point of view. Broadening and intensification of both updraft and downdrafts (especially the forward flank

one) also clarifies the pattern of the surface precipitation in Figure 3.8b (i.e., larger area covered with light precipitation). Lastly, it is important to note that the introduced parameterization correctly preserved the main features of the cloud, rather than entirely (and erroneously) modifying the physics and dynamics of this idealized supercell.

3.1.4   Real case validation

This section analyzes the applicability of the gust front parameterization scheme in a real case of thunderstorms that developed over the UAE region on 17 July 2009. Due to the novelty of this approach and the "ideal" atmospheric sounding that was used to spawn the supercell Cb, the performances of the scheme in the real (modelled) atmosphere are nevertheless worth investigating. Figure 3.11 shows the satellite observations (IR108 channel) for 17 July 2009 and from 10:00 UTC to 17:00 UTC over the UAE and surrounding regions. Figures 3.12 and 3.13 are the WRF simulations of the IR108 channel without and with the gust front parameterization scheme, respectively. It should be noted here that the original satellite images (Figure 3.11) and the WRF replicas (Figures 3.12 and 3.13) are geographically not a perfect copy of each other due to the differences in the projections used in the satellite imaging and the WRF model. The differences, however, are very small and they do not influence neither the results nor their comparisons. It should be also noted that the comparison between the brightness temperatures in the original satellite images and WRF-produced replicas should be in relative, rather than absolute terms as the values of parameters and coefficients used to produce the original satellite images were not available. Using Reanalysis-2 data (Kanamitsu et al., 2002), it is determined that the sea surface temperature in the satellite images is around 303–305 K, while the cloud tops are most likely around 206 K. These values are uncertain, in particular the cloud top temperatures. However, since the goal of this analysis is to assess the differences in the cloud evolution, structure, shape and location, performing relative comparisons without knowing the exact temperature values in the satellite images is satisfactory. Lastly, in order to

minimize any confusion in the comparisons between these three figures, the WRF results are first be compared against each other and afterwards their similarities and discrepancies are compared to observations.
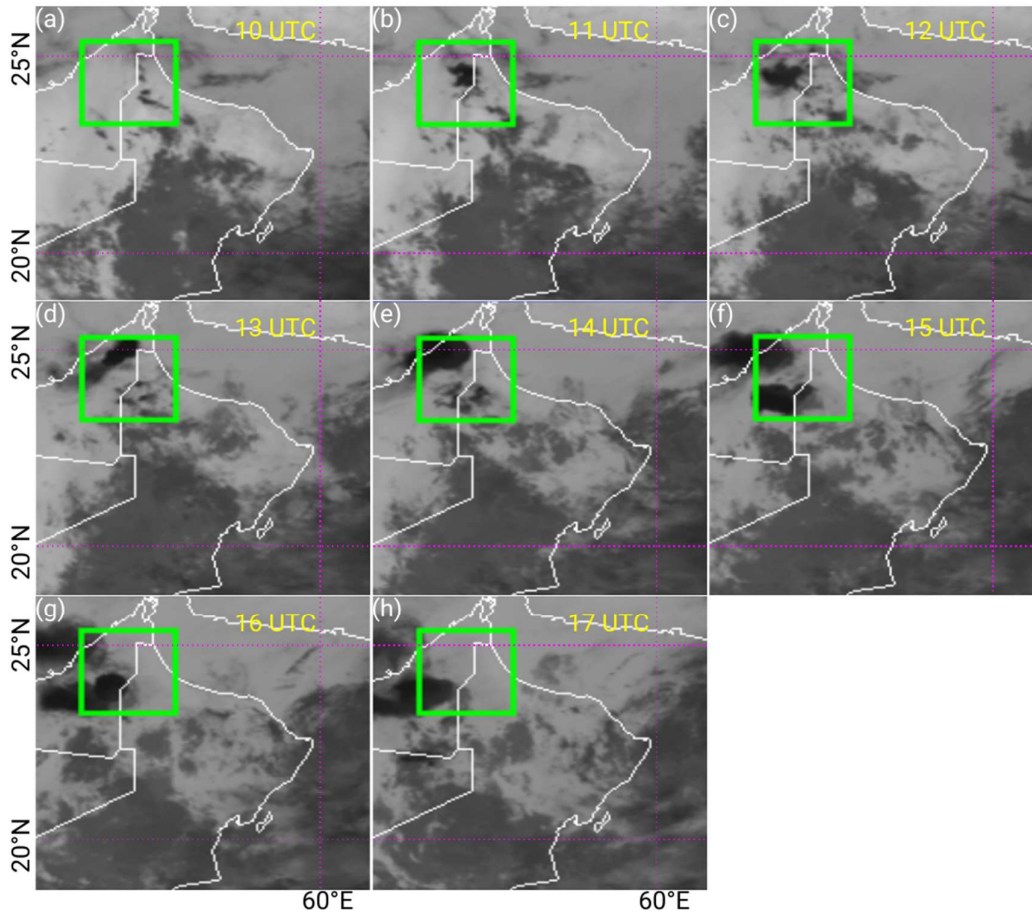
Figure 3.11 Satellite images obtained using the IR108 channel (showing brightness temperature) onboard Meteosat Visible Infra-Red Imager (MVIRI) for the d1 domain in WRF. The green rectangle represents the d2 domain (see Figure 3.4). The yellow text shows UTC time.

The focus of this analysis is on the strong convection that starts to develop in the center of the domain d2 (green rectangle) around 10:00 UTC. It can be observed that WRF with the gust front parameterization scheme (Figure 3.13) clearly produces more convective clouds throughout the simulation period. For instance, at 11:00 UTC the differences in the lengths of squall lines in the center

of d2 are clearly visible—the squall line in Figure 3.13b is 1.7 times longer than the one in Figure 3.12b.
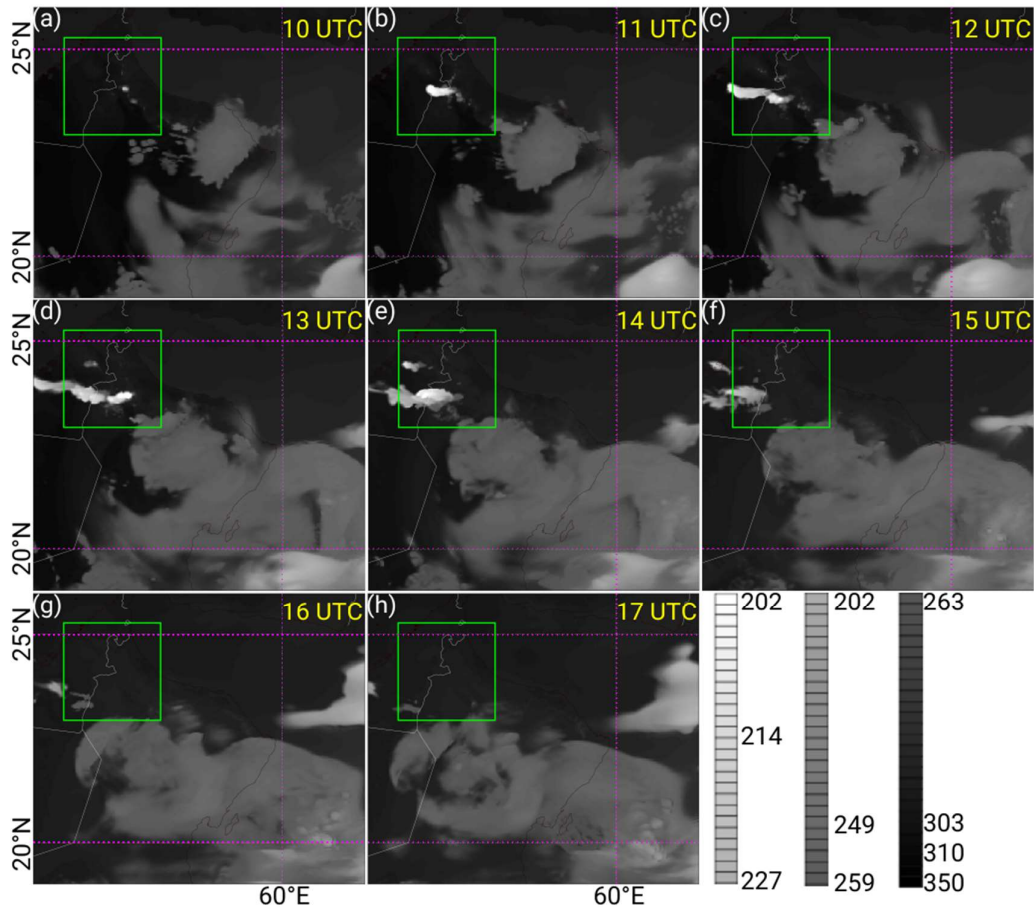
Figure 3.12 Same as Fig. 12, but created using WRF model without the gust front parameterization scheme. The brightness temperature is given in K

Similar ratio between the lengths of the squall lines in the direction of the cloud propagation is found at 12:00 UTC, as well as at 14:00 UTC for a new cloud system that appeared in the northwest part of d2. At 10:00 UTC, i.e., time when the squall line was in its early development stage, the ratio of the footprint lengths was as high as 5.1. The result that WRF with the parameterization of gust front produces more cloud is anticipated, but it is important to note that the new cells are spawned in the direction of the cloud movement, which was calculated from the prevailing wind direction in the upper atmopshere.

The satellite observations (Figure 3.11) show the existence of this convective system, but not in a squall line form as the WRF simulations reproduced. Convection in Figure 3.11 resembles an irregular spot-like shape particularly in the early stages of development (from 10:00 UTC to 12:00 UTC). In satellite images, the convective clouds formed around 13:00 UTC and their width is 2–3 times larger than in the two WRF cases.
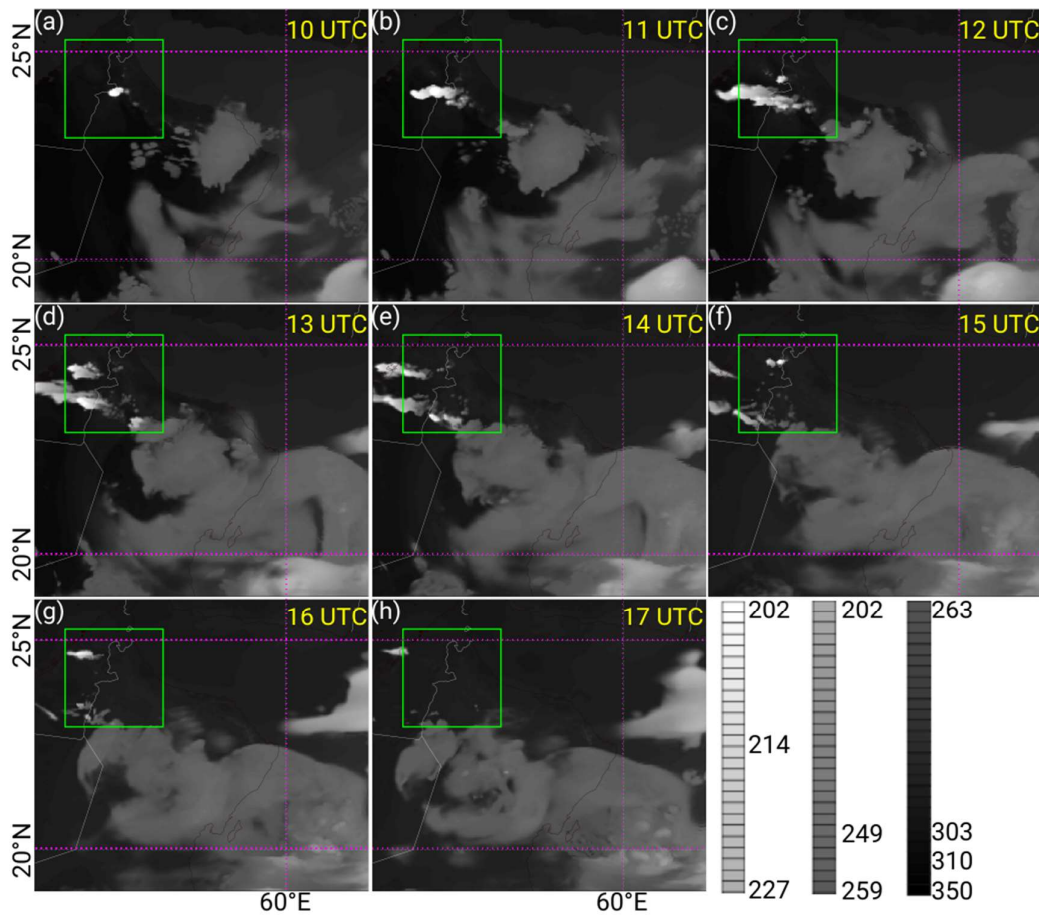
Figure 3.13 Same as Figures 3.11 and 3.12, but created using WRF model with the gust front parameterization scheme. The brightness temperature is given in K.

Apart from these differences, the WRF simulation with parameterization of gust front (Figure 3.13) produced more convective clouds, thus making the results more similar to the satellite observations. This tendency of WRF with gust front scheme to match the satellite measurements when compared to the WRF model

without gust front parameterization is particularly noticeable at 12:00 UTC and 13:00 UTC. The differences between the WRF results and the satellite images are also very evident in the late afternoon. That is, despite the strong convection that still persist around 16:00 UTC and 17:00 UTC (Figure 3.11g,h), the WRF model without the gust front scheme did not produce any convective clouds in d2, whereas the WRF with the gust front scheme spawned some convection in the northwest region of d1 and d2. Once again, it seems the inclusion of the gust front parameterization scheme qualitatively brings the simulation closer to the observations. The results also show that the scheme was accurately deployed only on the deep convective clouds in both domains. The stratiform clouds in the southeast part of d1 are not influenced by the presence of this scheme.

Figure 3.14a shows the observed maximum composite radar reflectivity (in dBZ) and the accompanying WRF simulations in the panels b and c. At 13:00 UTC, the differences between WRF simulations and the observation are very pronounced. The orientation, the length, and the width of the cloud footprint in the radar image are considerably different than those in the WRF simulations. The prevailing orientation of the zone with strong radar reflectivity (> 40 dBZ) is southwest to northeast in the radar image (Figure 3.14a), while the same zone is in the east-west direction in the WRF simulations (Figure 3.14c,d) and much smaller. Similar to satellite observations, the length and width of clouds in radar images are several times larger than in the WRF cases. It is important to note, however, that the poor WRF performances in this particular case are independent of the gust front collapse treatment as they also appear in the default WRF simulation without gust front scheme. Similar geographical displacements of WRF clouds from the observed locations were also reported by Lompar et al. (2017) in their investigation of severe thunderstorms over Serbia and Bosnia and Herzegovina. WRF deviations from radar observations are also documented in the papers by Koch et al. (2005), Molthan et al. (2010), Shi et al. (2010) Molthan and Colle (2012) and Min et al. (2015). It seems the differences between simulated and observed radar reflectivity are a strong

function of deployed microphysics scheme and simulated weather conditions. Yet another source of discrepancies between numerical simulations and radar observations might be radar miscalibration and measurement errors (see Wilson and Brandes (1979), Jordan et al. (2003) and Zhong et al. (2016) and references therein). These results point out that regardless of the gust front parameterization scheme, a lot of research is needed before the numerical results can accurately match the radar observations.
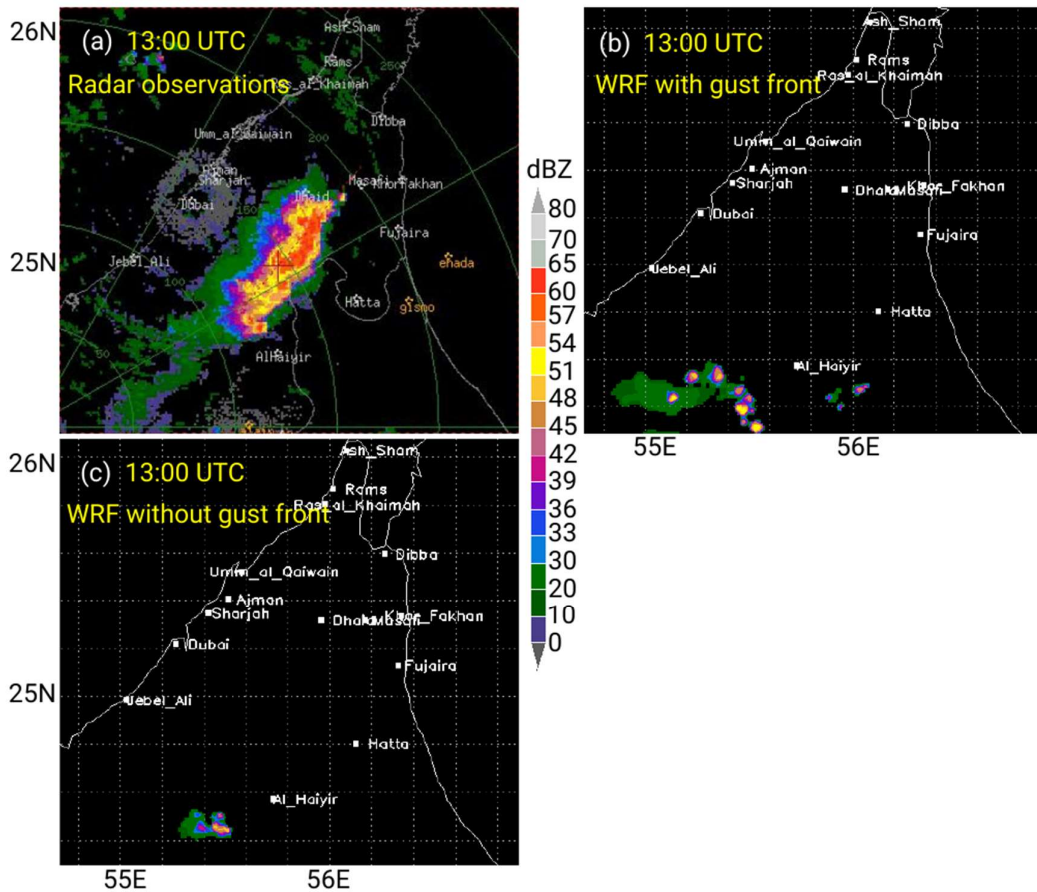
Figure 3.14 (a) Maximum composite radar reflectivity from radar observations and the WRF model (b) with and (c) without the gust front parameterization scheme at 13:00 UTC.

Despite the reported differences between the WRF simulations and radar measurement, Figure 3.14 once again demonstrates that the WRF model with the gust front scheme produced more clouds in the direction of prevailing cloud

movement than the WRF without the gust front scheme. The footprint of maximum composite radar reflectivity when the gust front is parameterized is ~3.5 times longer than in the default WRF run. Both models gave the maximum radar reflectivity of about 55 dBZ, while the corresponding maximum in the measurements reaches 65 dBZ. In Figure 3.14b (WRF with gust front), there are five cells with the composite radar reflectivity above 50 dBZ southwest and west from Al Haiyir, while there is only a single cell with this value of radar reflectivity in Figure 3.14c (WRF without gust front). The periodic appearance of new cells in the direction of cloud movement in Figure 3.14b is in accordance with the sinusoidal forcing of vertical velocity that is implemented in the proposed scheme. Another difference between the two WRF runs is the formation of cumuliform clouds southeast of Al Haiyir in the parameterized case (Figure 3.14b). Although both simulations considerably differ from the radar measurement, the WRF model with gust front scheme produced a larger zone with radar reflectivity than the default WRF, thus bringing it closer to the reality in the investigated case.

Surface accumulated precipitation over two 30-min periods and in the area of interest is shown in Figure 3.15. Real measurements were unfortunately not available for this sparsely populated desert region in UAE. In both time intervals, WRF with the gust front scheme produced more precipitation than the default WRF. In the period 12:00–12:30 UTC, the inclusion of the gust front scheme approximately doubled the amount of total precipitation. In the next 30 min the difference between two WRF simulations decreased but the gust front scheme still resulted in more surface precipitation. In the first 30-min period, WRF with the gust front scheme formed three additional precipitation zones south of Al Ain that do not appear in the default WRF run.

The precipitation amount reaches 16 L in 30 min in the center of the largest of these three zones. Between 12:30 and 13:00 UTC, a weak precipitation zone northeast of Al Ain in the default WRF run is much more pronounced in the

terms of size and intensity in the WRF model with the gust front scheme (Figure 3.15c).
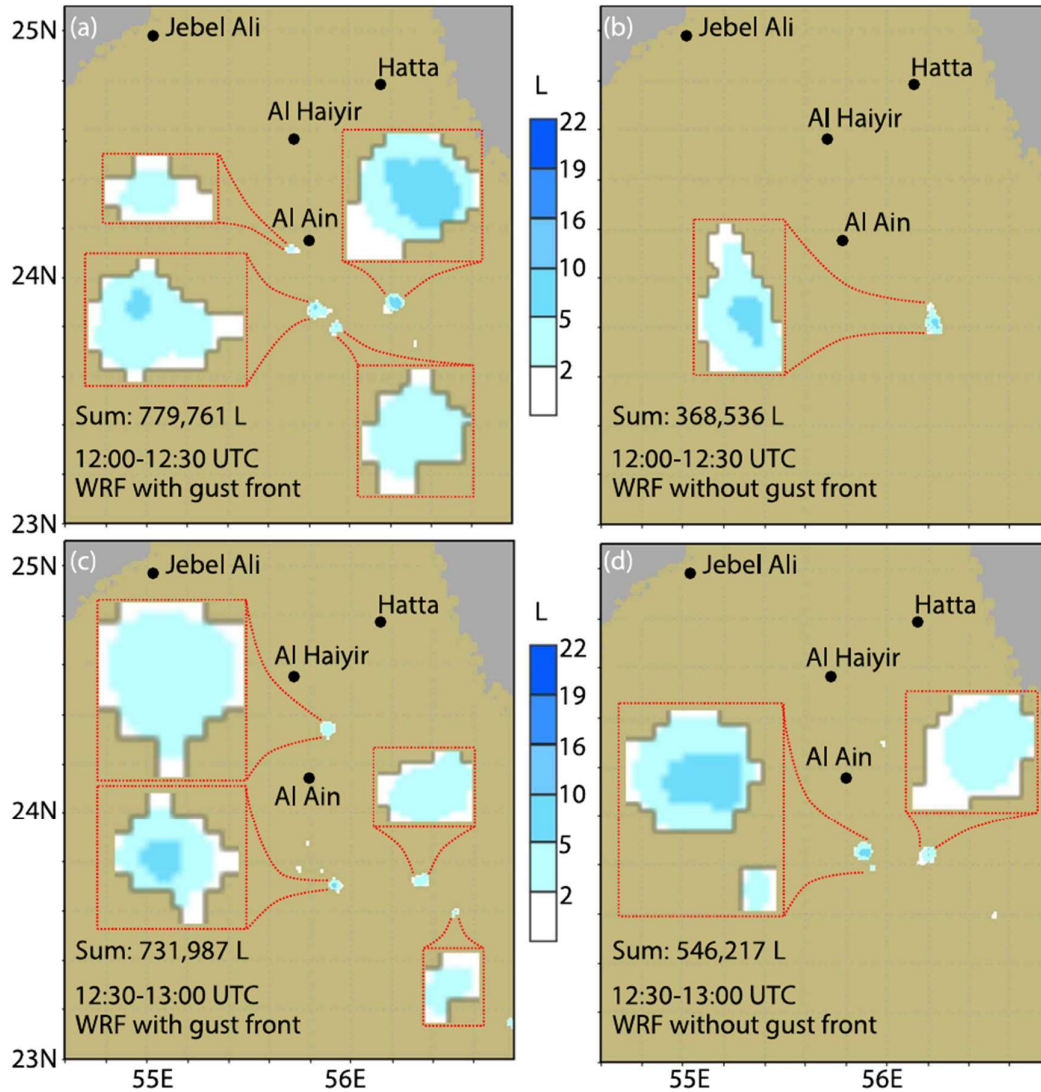
Figure 3.15 Accumulated surface precipitation between over two 30-min from the two WRF runs. The red parallelograms contain enlarged (zoomed-in) areas with significant amounts of accumulated precipitation. Real surface measurements are unavailable for this event.

Comparing these surface precipitation results (Figure 3.15) with the WRF-generated radar image at 13:00 UTC (Figure 3.14b,c), it seems that only the convective clouds southeast of Al Haiyir formed precipitation that reached

surface. The convective cells west and southwest of Al Haiyir do not appear in the surface precipitation footprint in Figure 3.15c. The similar observation regarding the discrepancies between radar and surface precipitation results also holds for the WRF simulation without gust front scheme (Figures 3.14c and 3.15d). These differences might be due to a couple of reasons. First, the radar images produced in WRF are instantaneous slices over time and space while the surface precipitation is accumulated over the 30-min period prior to the time when the radar images were created. Second, convection that appears west and southwest of Al Haiyir in the radar images might be a rapidly developed cumuliform cloud whose lifetime was short in order for the processes such as riming and collision to produce precipitation that would reach surface.
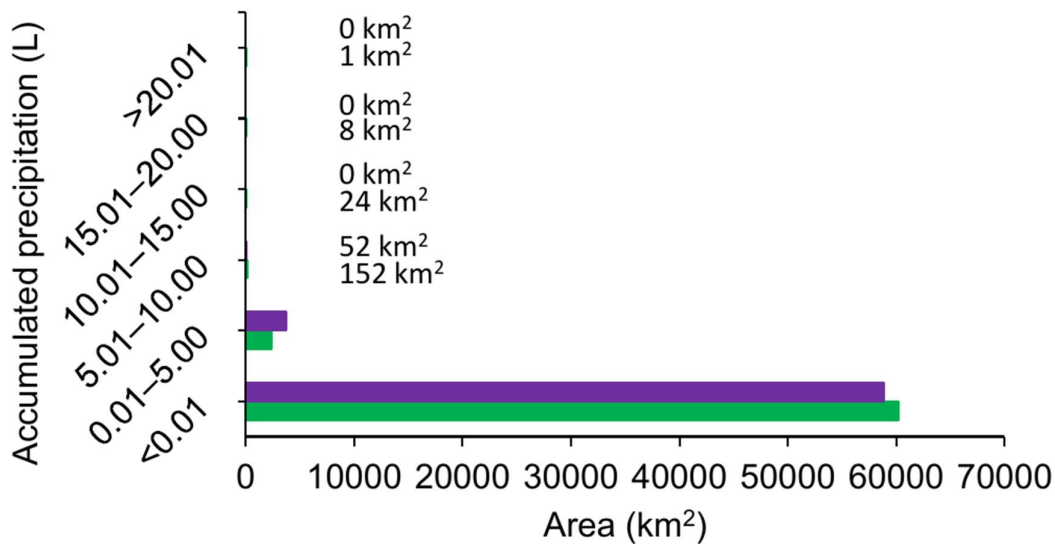
Figure 3.16 Histogram of different precipitation amounts in the domain d2 with the parameterized gust front (purple bars) and the default run without gust front (green bars). See Figure 3.9 for the comparison with the ideal case.

A histogram of precipitation intensities in the domain d2 for the time interval 12:00–13:00 UTC is depicted in Figure 3.16. Similar to the ideal case (Figure 3.9), the inclusion of the gust front scheme significantly increased the area with light precipitation (0.01–5.00 L) and consequently decreased the overall area without

precipitation (<0.01 L). Moreover, it seems that the gust front scheme hampered the development of very intense and localized precipitations as the areas with the accumulated precipitation above 10.01 L do not exist in the gust front case. The area characterizes with precipitation 5.01L and 10.00 L is larger in the default run. These results are similar to the ideal case (Figure 3.9) in which the strong precipitation was also more pronounced in the default WRF run without the parametrized gust front. This result is particularly important since both simulations used the microphysics scheme with explicit treatment of aerosols (Thompson and Eidhammer, 2014) which tends under-predict the light precipitation (Lompar et al. 2017, Thompson and Eidhammer 2014; Sorooshian et al., 2010; Qian et al., 2009).However, more research is needed before a definite conclusion can be drawn on the performances of this scheme in real atmospheric simulations.

3.2 Natural aerosols in WRF-ARW

Despite an important role the aerosols play in all stages of cloud lifecycle, their representation in numerical weather prediction models is often rather crude. Here we investigates the effects the explicit versus implicit inclusion of aerosols in a microphysics parameterization scheme in WRF-ARW model has on cloud dynamics and microphysics. The testbed selected for this study is a severe mesoscale convective system with supercells that struck west and central parts of Serbia in the afternoon of July 21, 2014. Numerical products of two model runs, i.e. one with aerosols explicitly (WRF-AE) included and another with aerosols implicitly (WRF-AI) assumed, are compared against precipitation measurements from surface network of rain gauges, as well as against radar and satellite observations.

3.2.1 Model configuration and data
The tests were performed embedding four one-way nested domains with horizontal grid spacing of 27, 9, 3, and 1 km on Arakawa C-grid (Figure 3.17).

The largest domain includes Europe and parts of the north Africa in order to simulate the transport of aerosols from the Sahara Desert to the Balkans.
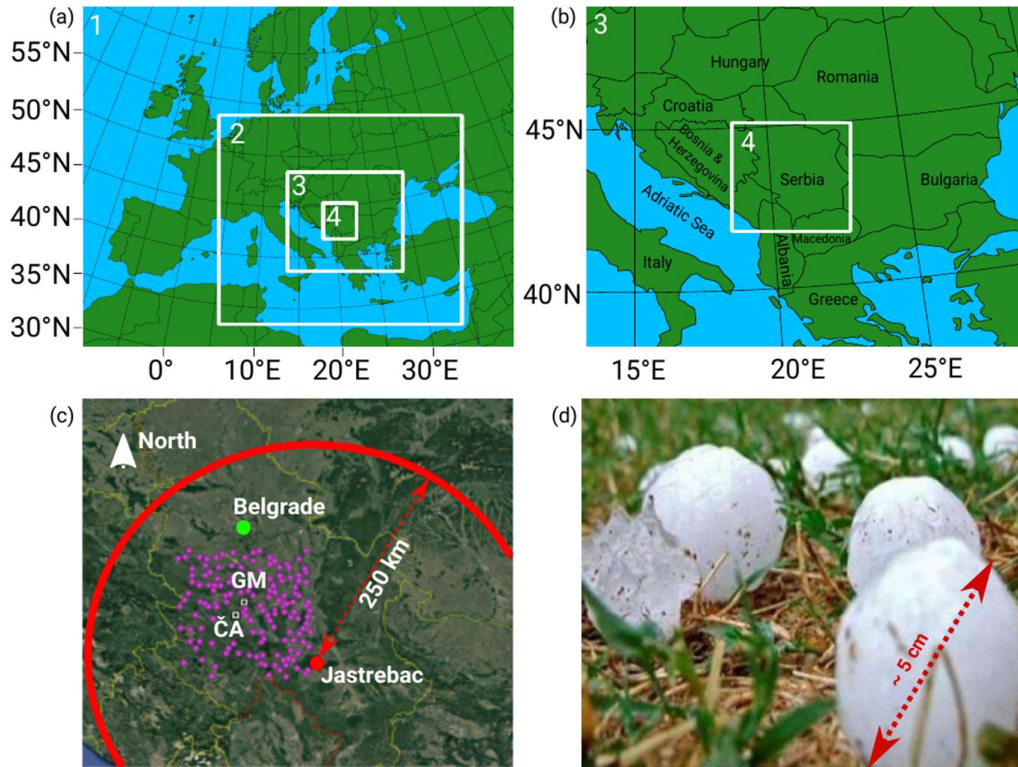
Figure 3.17 (a) Model domains used in this study and (b) the closer look at the two finest domains. (c) Study area with 149 weather stations (pink dots) used for validation of numerical simulations. The hailstorm on July 21, 2014 was most intense in the Čačak (ČA) and Gornji Milanovac (GM) regions [white squares in (c)], as demonstrated with the hailstone size of a golf ball in (d). In (c), the position and range of the Doppler radar in Jastrebac are indicated with a red dot and red circle, respectively (radar altitude is 1522 m). The position of Belgrade radiosonde station is depicted with the green circle in (c).

The recommended 3:1 nesting ratio is used and all domains had 64 vertical levels. The finest domain encompasses the MSC that is used as a test case in this study. The physical schemes used are Thompson et al. (2008) (T08 hereafter) and Thompson and Eidhammer (2014) (TE14 hereafter) for cloud microphysics (Thompson et al. 2008; Thompson and Eidhammer 2014), the Rapid Radiative Transfer Model scheme for longwave radiation (Mlawer et al., 1997), the

Dudhia scheme for shortwave radiation (Dudhia, 1989) and the Noah land surface scheme (Ek et al., 2003). Cumulus convection is parameterized in the coarse domains (27 and 9 km horizontal resolutions) utilizing the Kain-Fritsch scheme (Kain, 2004), whereas a cumulus scheme was not used for the finest two domains (3 and 1 km horizontal resolutions). In TE14, for instance, cumulus parameterization was excluded in the domains with horizontal grid-spacing below 4 km. Lastly, the planetary boundary layer scheme employed in this study is the Yonsei University scheme, which is nonlocal, first-order scheme with explicit entrainment layer and parabolic K (eddy diffusion coefficient) profile in unstable mixed layer.

In total, two numerical simulations are performed; one using T08 scheme and another using TE14 microphysics, while the rest of the model configuration stayed unchanged. That way, the influence of explicitly modelled aerosols could be estimated against the base case in which the aerosols are not modelled. Both cases are validated against the measurements from the rain gauge network and Doppler radar data (see Figure 3.17c). This dual-polarization radar operates at 10 cm wavelength.

The model simulations were initiated at 00:00 UTC on July 21, 2014 and ended at 06:00 UTC on July 22, 2014. These 30-h runs enabled the verification of model results against the measurements from the precipitation stations in Serbia between July 21, 2014 (06:00 UTC) and July 22, 2014 (06:00 UTC). The first 6 hours of the simulation represent a spinup period. The initial and boundary conditions are obtained from the Global Forecast System model outputs with a 0.5° × 0.5° horizontal resolution. Integration time step was 100 s in the largest computational domain with the utilization of the Runge-Kutta 3rd order time discretization, 2nd order diffusion on coordinate surfaces, and 5th and 3rd order horizontal and vertical advections, respectively, of both momentum and scalars.

The initial concentration of aerosols is obtained from the mean monthly values of the 7-year simulations (2001-2007; Colarco et al. 2010) of the global Goddard

Chemistry Aerosol Radiation and Transport (GOCART) model (Ginoux et al., 2001). These values are provided in a three-dimensional matrix. In the TE14 scheme, aerosols are divided in two categories: (1) water nucleating aerosols or number of water-friendly aerosols (NWFA) and (2) ice nucleating aerosols or number of ice-friendly aerosols (NIFA; TE14). The aerosol input data are included through the mass mixing ratios of sea salts, organic, sulfates, carbon, dust, and black carbon [for more information on black carbon see Shrestha et al. (2010)]. Dust particles larger than 0.5 µm are classified as NIFA, whereas all other species with the exception of black carbon are represented as NWFA (i.e., mixing ratios of sulfates, sea salts and carbon). A two-dimensional matrix is constructed close to the surface in order to represent the sources of these aerosols. Then, advection and turbulence mixing are transporting and dispersing the aerosols in each time step. Note that microphysical processes in clouds represent sinks (condensation, collecting, freezing, colliding/coalescence), as well as sources (evaporation, melting) of aerosols.

3.2.2   Description of test case

The MCS occurred on the afternoon of July 21, 2014 in the Western Balkans. The most severe conditions were observed around Čačak and Gornji Milanovac areas in Serbia (Figure 3.17c,d). Most of the day, the weather above Serbia was nice with weak south winds, the sweltering afternoon heat and temperatures around 33 °C. In the early afternoon, convective clouds started to develop above southwest and west Serbia. Approaching of the cold front and the accompanying increase of moisture led to an intensification of convection, as indicated in Figure 3.18. The Natural Colour RGB channel showed in Figure 3.18 enables a distinction between water and ice clouds due to the difference in absorption between the two. Water clouds appear whitish and ice clouds appear in cyan. The tops of cold cumuliform clouds over the Adriatic Sea and central Mediterranean reached the heights of 14 to 18 km above surface. A cyclone in the Gulf of Genoa and the counterclockwise circulation above the central Mediterranean resulted in the transportation of dust from Sahara Desert

over the Mediterranean and to the Balkans (Figure 3.18). In addition, the advection of warm and moist maritime air takes place ahead of the cold front situated above the Mediterranean (Romanić et al., 2016a).
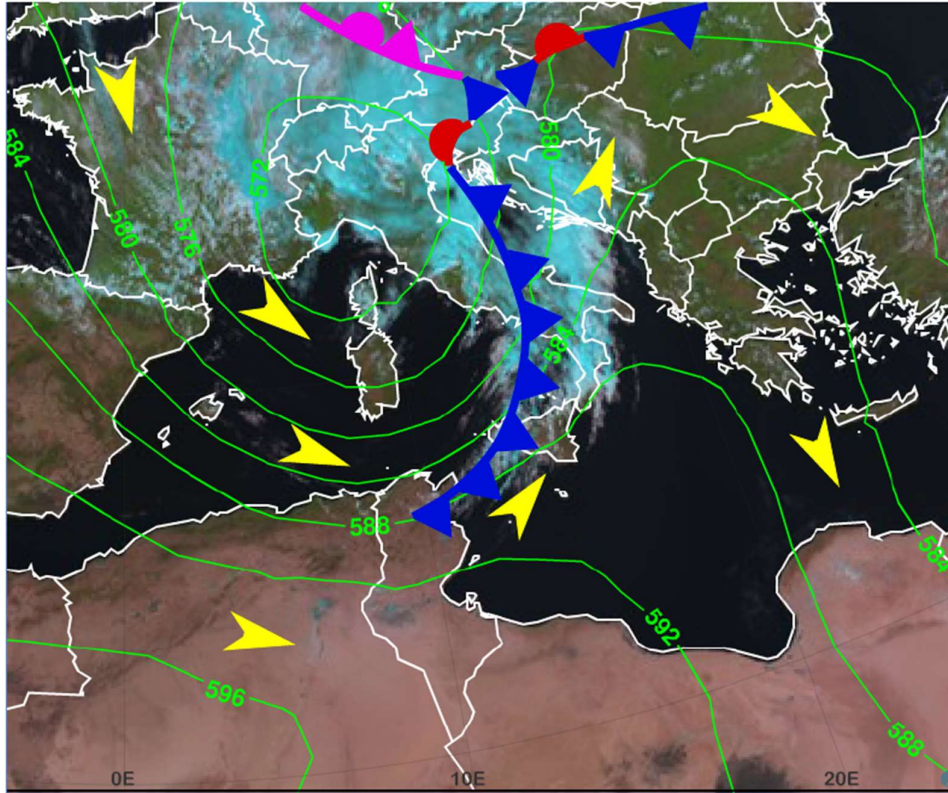
Figure 3.18 Synoptic chart of the parts of Europe and north Africa on July 21, 2014 (12:00 UTC) based on the Meteosat Second Generation satellite imagery obtained using the Natural Colour RGB channel (operated by EUMETSAT: http://www.eumetrain.org/). The emphasis is on the cold front above central Mediterranean and the associated cloud system. The flow direction at 500 hPa and the height of this isobaric surface in decameters are indicated with yellow arrows and green contours, respectively.

Skew-T – log P diagram in Figure 3.19 shows favorable conditions for development of multi-cells or supercells on July 21 around noon in a region around Belgrade.

The Convective Available Potential Energy (CAPE) exceeded 2000 J kg⁻¹, which indicates that updrafts in the thunderstorm might have reached the maximum value of $w_{max} = \sqrt{2 \cdot CAPE} = 66$ m s⁻¹ at the Equilibrium Level (EL). These strong updrafts were accompanied with the high water vapor content in the vertical column of air (32 mm). Convective Condensation Level (CCL) was at 2,200 m (781 hPa), the height of the freezing level (H_0) at 4,240 m, the height of the -10 °C isotherm at $H_{-10} = 5800$ m, the Lifted Condensation Level (LCL) at 816.3 hPa, and the Level of Free Convection (LFC) at 764.7 hPa. Wind shear in the first 6 km above surface was 7 m s⁻¹, and about 12 m s⁻¹ in the layer between 9 and 11 km above surface.
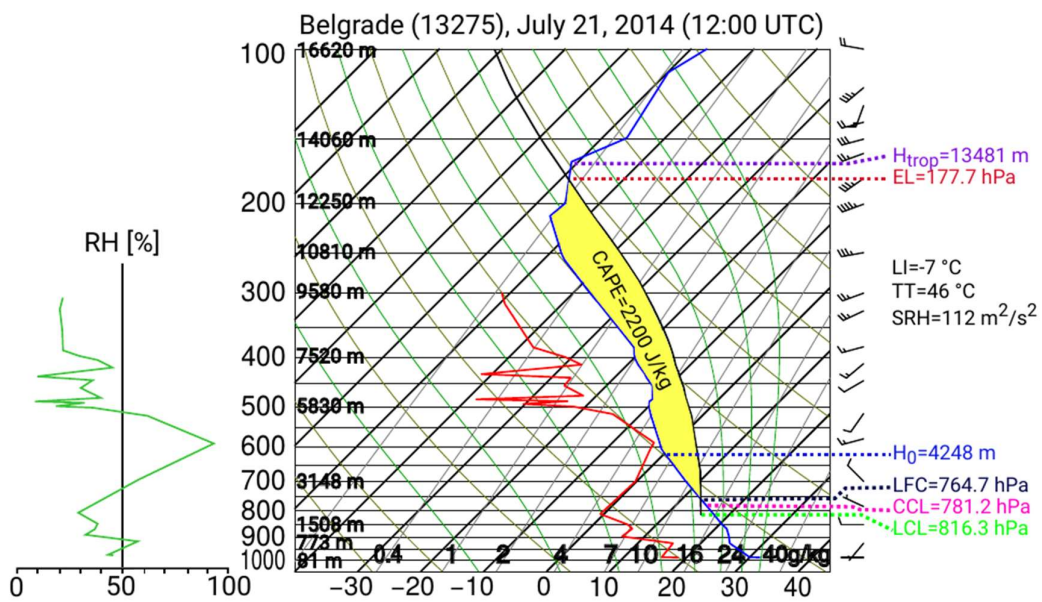
Figure 3.19 Skew-T – logP diagram for the radiosonde weather station in Belgrade (ID: 13275, Košutnjak, Lat 44°46′15.33″ N and Lon 20°25′29.28″ E, see Figure 3.17c) on July 21, 2014 at 12:00 UTC. The full blue and red lines are the vertical profiles of temperature and dew point, respectively. The dashed color lines represent the heights of important levels. The chart on the left and the full green line show the vertical profile of relative humidity.

Consequently, the Storm Relative Helicity (SRH) was 112 m² s⁻² – a value that is considerably smaller than the one observed above the same region under the

stable atmosphere and a strong low-level jet (Romanić et al., 2016b). The conditions described above favor the development of multi-cells or possibly supercells (Peppler, 1988; Rasmussen and Blanchard, 1998) deep enough to penetrate the tropopause. The Lifted Index (LI) of -7 °C and Total Totals (TT) of 46 °C are all precursors of strong convection, heavy rainfall and likelihood of hail development. The resulting precipitation was showery and non-uniformly distributed on the surface. West and central Serbia saw most rainfall, respectively, while the northern and southern parts of the country were not affected by this MSC. The precipitation amounts in Čačak and Gornji Milanovac regions were around 50 mm and the amounts in central Serbia were approximately 20 mm with more than 2,000 lightning strikes registered during the thunderstorm. This region also suffered the worst damage to infrastructure (Figure 3.17d).

In summary, the transport of NIFA from the north Africa to the Balkans complemented with strong convective activity in the central regions of Balkan are the main reasons behind selecting this weather scenario for testing the sensitivity of WRF model to an explicit inclusion of aerosols. Moreover, the dense network of rain gauges in Serbia as well as the availability of radar and satellite products for this MCS enabled various verifications of numerical results.

3.2.3 Aerosols impact assessment on cloud dynamics and precipitation

Forecasted locations of NIFA and cloud cover for July 21 at 12:00 UTC are portrayed in Figure 3.20. WRF-AE accurately recognizes the north Africa as the source area of ice nucleating particles (shown in yellow in Figure 3.20). The northward transportation of NIFA over the Mediterranean and towards the Balkans is clearly depicted. Qualitatively there is a good agreement between the numerical results in Figure 3.20a,b and satellite observations shown in Figure 3.20c,d and Figure 3.18. The simulated locations of cloud systems over the Mediterranean, central Europe and western Balkans closely match the

observations. The major transport of NIFA took place ahead of the cold front situated over the central Mediterranean (Figures 3.18 and 3.20). High reaching thick ice clouds (dark red color in Figure 3.20d) over the Adriatic Sea and east Italy are accurately modelled by WRF-AE (Figure 3.20a,b). The isolated groups of clouds, such as the one above Corsica, are also captured.
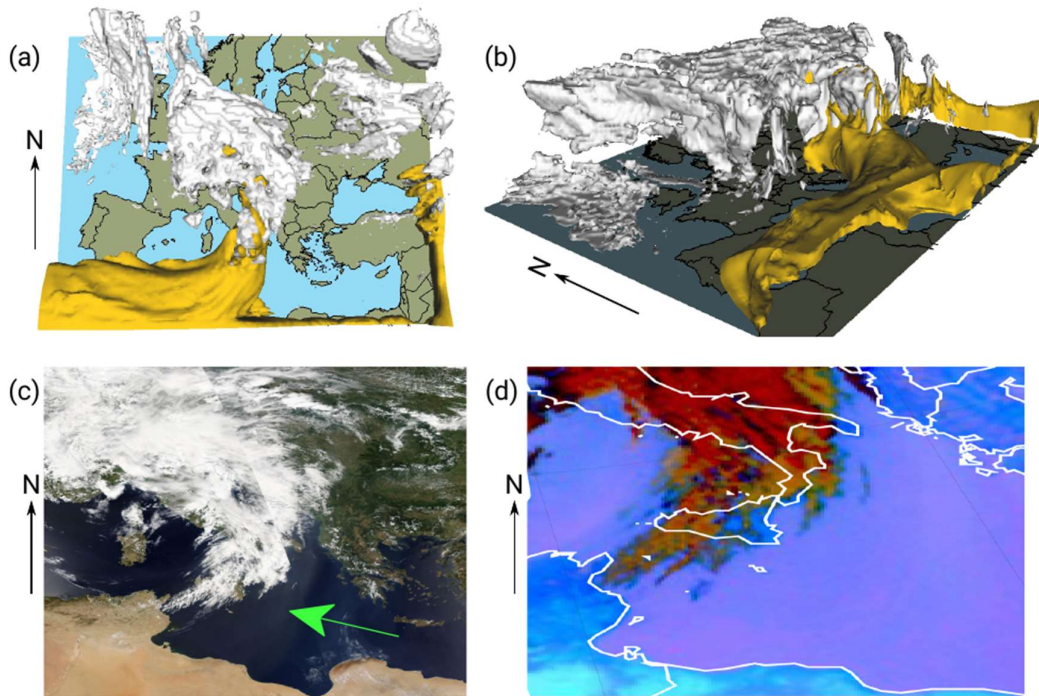
Figure 3.20 In (a) and (b), two different views of WRF-AE simulation of cloud cover (white) and aerosol concentration (yellow) over Europe and north Africa on July 12, 2014 (12:00 UTC). The yellow colour represents 6 hydrophobic aerosols per cm^3. (c) Visible wavelengths leaving the top of the atmosphere and centered at 645 nm (red), 555 nm (green), and 469 nm (blue) - Moderate Resolution Imaging Spectroradiometer (MODIS) bands 1, 4, and 3, respectively. Transport of dust from the Sahara Dessert (ahead of the cold front; see Figure 3.18) is indicated with the green arrow. (d) Zoom in of the Dust RGB channel from the Meteosat Second Generation satellite over the central Mediterranean. This channel is designed to monitor the transport of dust (pink) during both day and night. The Dust RGB is composed from a combination of the Spinning Enhanced Visible & Infrared (SEVIRI) IR8.7, IR10.8 and IR12.0 channels.

Figure 3.21 is a comparison between could dynamics from WRF simulations with and without aerosols (left and middle panels, respectively) and satellite

images (right panels). The satellite imagery corresponds to the IR 10.8 μm channel and the focus is on the convective system in central and southwest Serbia. The observations show a convective activity that kicked off around 14:00 UTC in the Čačak and Gornji Milanovac regions and kept intensifying until 17:00 UTC, when it became an MCS. Both models managed to reconstruct the supercells, but they slightly displaced their locations toward southeast. The cloud system in the north Serbia at 14:00 and 15:00 UTC is captured neither by WRF-AE nor WRF-AI. The differences between WRF-AE and WRF-AI results are not pronounced, but they exist. In the WRF-AI case, the convective cells in the initial stage (14:00 UTC) are smaller and disjointed. That is, four individual cells are clustered in southwest Serbia, while the Cb clouds in the WRF-AE case are smeared out and the individuality of cells in not recognizable. This discrepancy between the WRF-AE and WRF-AI results diminishes with time. In the mature stage of the storm (17:00 UTC), the location and spread of Cb clouds from the WRF-AE run resemble the observations more closely than in the WRF-AI case. Thunderstorms in Bosnia and Herzegovina are visible in both simulations and they match the satellite observations fairly close.

Modelled composite reflectivity is compared against radar observations in Figure 3.22. Once again, the left panels correspond to WRF-AE case, the middle panels are the WRF-AI products and the right panels are observations. The measured echo at 14:45 UTC in the region west of Čačak had a hook-like shape and exceeded 60 dBZ. A strong radar reflectivity (around 50 dBZ) is observed south of Valjevo, as well as in a wide region south of Čačak at 14:45 UTC. The echo in this region was about 40 dBZ and the cell resembles a supercell shape. In the next 15 minutes, the echo south of Valjevo weakened, whereas the reflectivity around Čačak additionally intensified. Finally, at 15:15 UTC, the echo around Valjevo continued weakening (below 35 dBZ), but the convection intensified in the region southwest of Ivanjica where the radar reflectivity reached around 60 dBZ. The supercell at Čačak separated in two isolated cells (Ćurić et al., 2003).
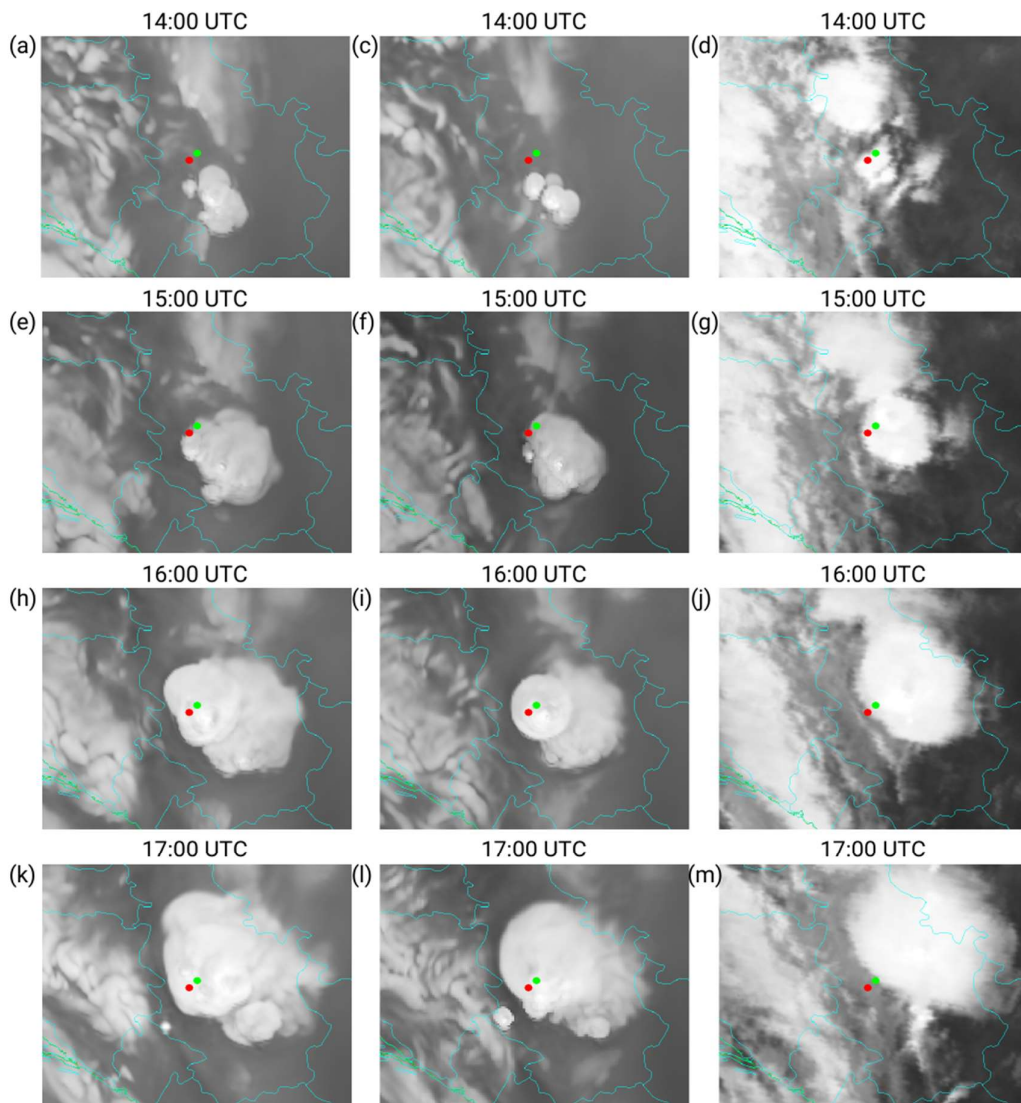
Figure 3.21 Development of supercells above Serbia according to WRF-AE (left panels), WRF-AI (middle panels) and satellite observations (right panels) from the SEVIRI 10.8 µm channel on board the Meteosat Second Generation satellites. The red dots are Čačak and the green dots are Gornji Milanovac.

Figure 3.22 further shows that models missed the zone of pronounced radar reflectivity in the Valjevo region. Both models inaccurately predicted the location of strongest composite reflectivity around Ivanjica, instead of Čačak. Moreover, the maximum reflectivity in the modelled cases are less than 50 dBZ, which is some 10 dBZ below the observed values. Additionally, the modelled reflectivities below approximately 40 dBZ spread over the larger area compared

to the measured echoes. The displacement of this zone to the east is also noticeable. In the WRF-AE case, the echo seem to resemble a hook-like shape, but around Ivanjica instead of Čačak.
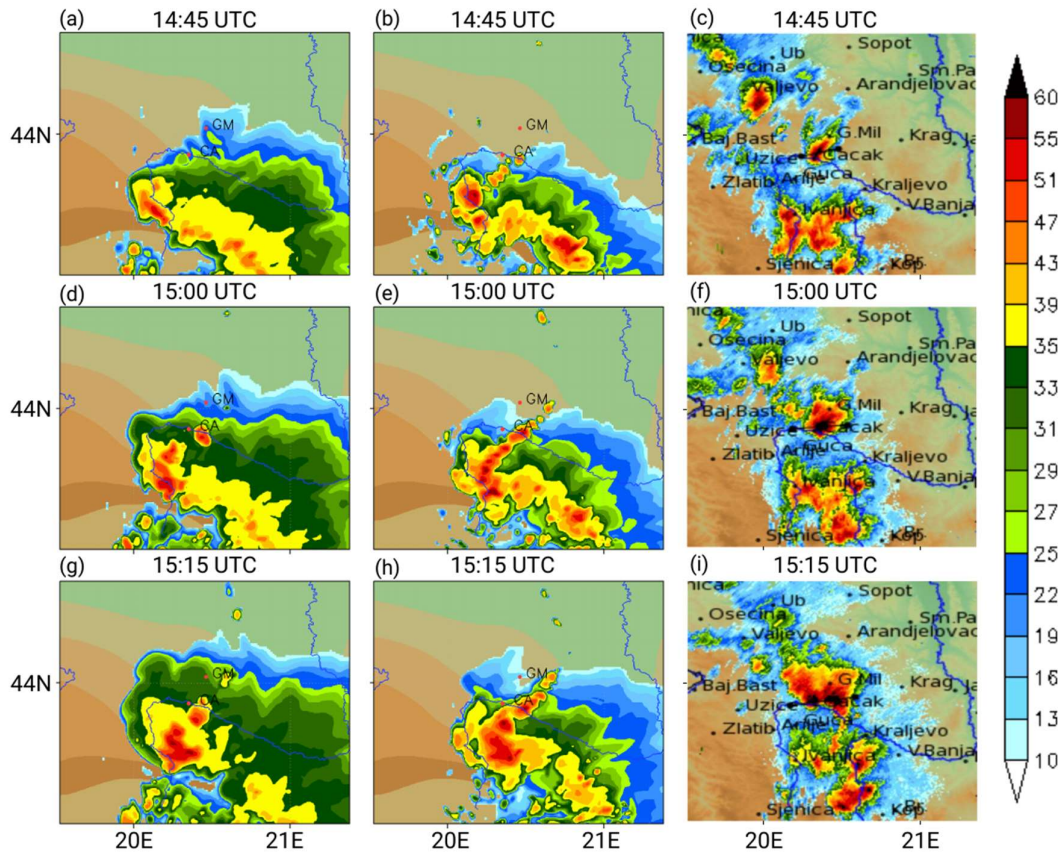
Figure 3.22 Composite radar reflectivity according to WRF-AE (left panels), WRF-AI (middle panels) and radar measurements (right panels) from the Doppler radar located in Jastrebac (see Figure 3.17c).

The WRF-AI simulation, on the other hand, shows the isolated convective cells aligned in the southwest to northeast direction in the region between Ivanjica and Čačak. This pattern of isolated cells in the WRF-AI case is also observed in Figure 3.21.

Figure 3.23 shows the modelled (Figure 3.23a–f) and measured (Figure 3.23g) accumulated precipitation amounts (in mm) over the central and west Serbia.

Measurements from 149 surface stations (Figure 3.17c) are bilinearly interpolated in order to obtain their spatial distribution.
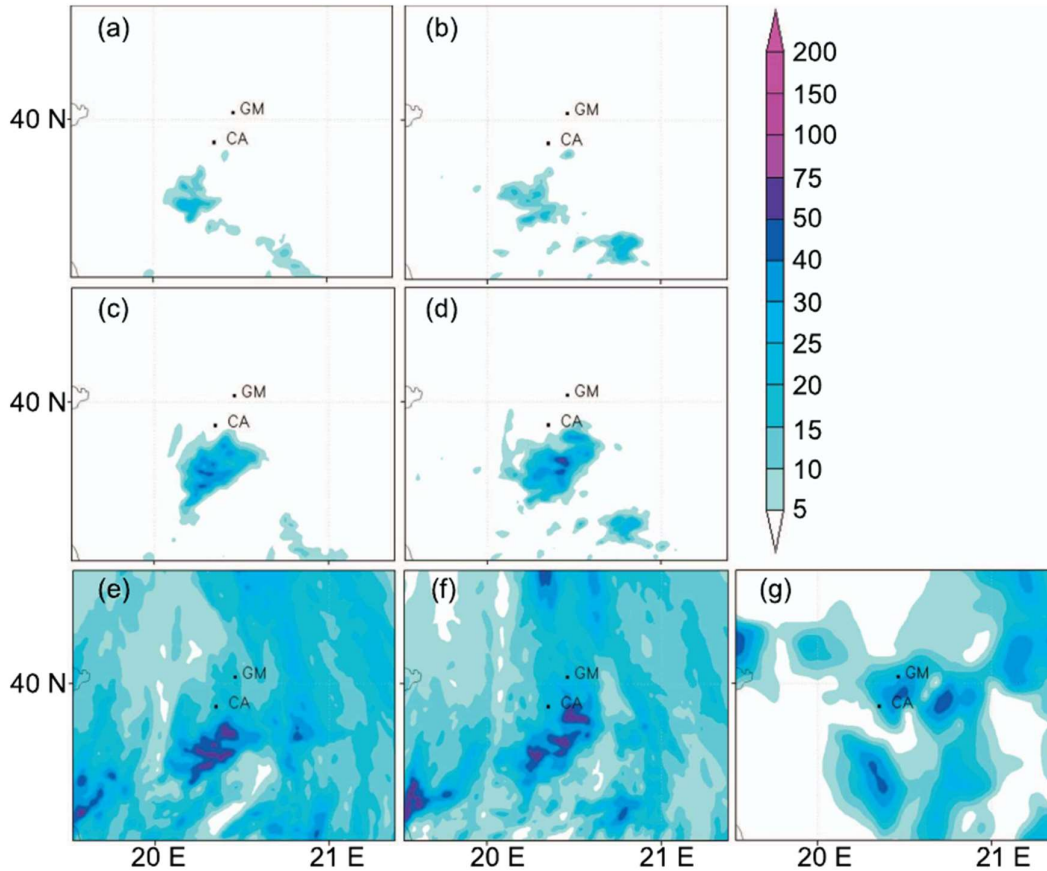
Figure 3.23 In (a) and (b), accumulated precipitation (in mm) between 14:45 and 15:15 UTC based on WRF-AE and WRF-AI simulations, respectively. Note that this time interval corresponds is the same as the time interval of measured radar reflectivity in Figure 3.22c,f,i. In (c) and (d), accumulated precipitation between 15:00 and 16:00 UTC based on WRF-AE and WRF-AI simulations, respectively. 24-h accumulated precipitation between July 21 (06:00 UTC) and July 22 (06:00 UTC) based on (e) WRF-AE, (f) WRF-AI, and (g) surface measurements.

Four zones of accumulated precipitation above 40 mm are noticeable in Figure 3.23g: (1) between Čačak and Gornji Milanovac, (2) east of Čačak, (3) south of Čačak and (4) around Valjevo (west regions in Figure 3.23g). Note that the accumulated precipitation in Figure 3.23a,b correspond to the same time period as the radar reflectivity images in Figure 3.22c,f,i. The comparison between

these two shows that the precipitation zones southwest of Čačak (Figure 3.23a,b) are nicely correlated with the strong radar reflectivity in Figure 3.22c,f and to some extend Figure 3.22i. Both models gave around 20 mm of precipitation between 14:45 and 15:15 UTC (Figure 3.23a,b), with WRFAE producing more intense precipitation in zone (3). It can also be seen that the precipitation areas in Figure 3.23a (WRF-AE) are more compact than in Figure 3.23b (WRF-AI), which is in accordance with the findings of Figure 3.21. However, it seems that both models missed the strong precipitation that occurred between Čačak and Gornji Milanovac, as well as the zone around Valjevo. Interestingly, the zones (2) and (4) are not accompanied with strong radar reflectivity in Figure 3.22c,f,i. Between 15:00 and 16:00 UTC, both models simulated around 50 mm of precipitation (Figure 3.23c,d) and those zones are again nicely correlated with the strong radar reflectivity south of Čačak, although the time periods used in the comparison are now different. The major takeaway from Figure 3.23a–d is that both simulations completely missed the epicenter of the largest damage located between Čačak and Gornji Milanovac. Analyzing the 24-h accumulated precipitation (Figure 3.23e,f,g), the models seem to accurately forecast the precipitation amounts, but their locations are inaccurate. For instance, both models give the accumulated precipitation below 20 mm in the area east of Čačak (zone (2) previously described), whereas the measured values are twice as larger. In the WRF-AE simulation, the zone of accumulated precipitation above 40 mm is concentrated around Ivanjica and north of it, but it does not reach Čačak as observations show. WRF-AI, on the other hand, gives three distinguished patches of large precipitation amounts located between Ivanjica and Čačak. Measurements show that intense precipitation is localized around Ivanjica, Čačak, and Gornji Milanovac, but not along the entire area between these towns, as the forecasts suggest. It seems though the WRF-AI precipitations around Čačak and Gornji Milanovac are in better agreement with the measurements. The WRFAE model forecasted larger total accumulated precipitation in the 24-h simulation period over the region

shown in Figure 3.23 (361,556 mm) than WRF-AI (323,379 mm), but both models overestimated the observations. It can be seen that the largest discrepancies are in the regions with the lightest precipitation, indicating that these zones are the most susceptible to aerosol modelling (TE14).
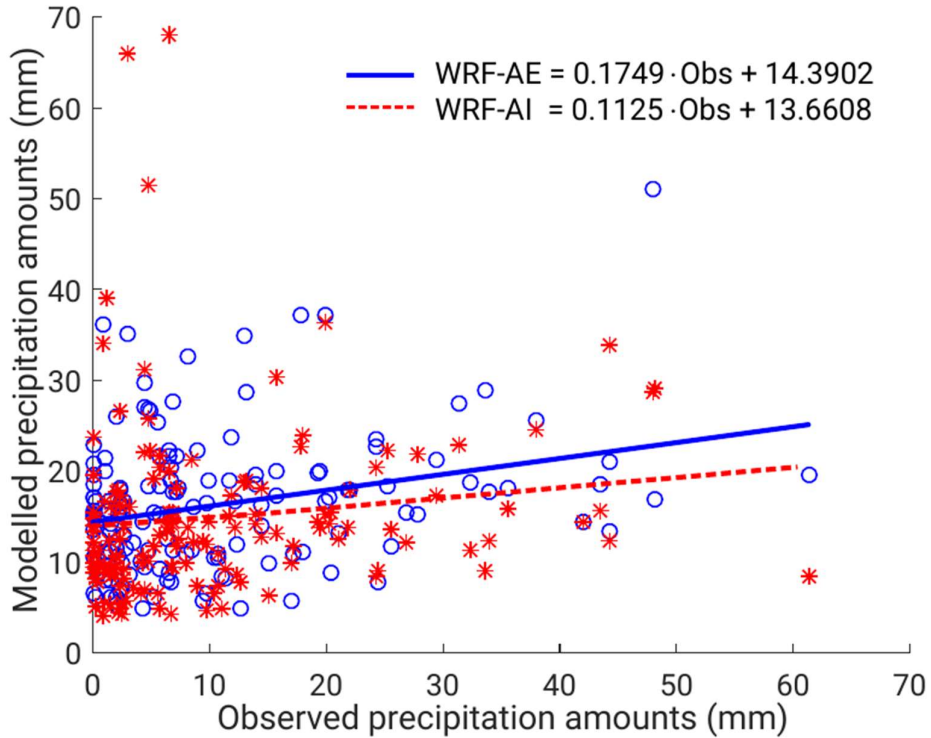
Figure 3.24 Relationship between modelled and measured precipitation for 149 weather stations shown in Figure 3.17c. WRF-AE vs. observations depicted with the blue circles and WRF-AI vs. observations indicated with the red stars. The best linear fits and associated equations are also shown. Note that these linear fits do not possess statistical significance.

A correlation analysis between modelled precipitation amounts and measurements is performed for each of the 149 considered stations and results are shown in Figure 3.24. The modelled results are characterized with large errors and very low correlation with measurements (Hogan, 1990; Fuchs et al., 2001; Ikeda et al., 2010; Rasmussen et al., 2011; TE14). The direct comparison between the modelled and observed convective

precipitation amounts is currently challenging because the reported values contain the errors due to both observations and model and errors tend to add up. Better correlations are typically observed in the cases of stratiform precipitation, comparison of seasonal values (Nieto and Rodríguez-Puebla, 2006) or in some instances relying on ensemble forecasting (He et al., 2013). The WRF-AI results show three pronounced outliers in the top left corner of Figure 3.24. These amounts are more than five times larger than the measured values. Such large overestimations, however, are not observed in the WRF-AE case. Theunder estimation outlier is once again more pronounced in the WRF-AI case. Although WRF-AI gave larger extremes, WRF-AE produced the overall larger amounts of precipitation (see also Figure 3.23). Namely, sums of accumulated precipitation in Figure 3.24 are 2421, 2214 and 1583 mm in the WRF-AE, WRF-AI and observation cases, respectively.

3.2.4 Aerosols impact assessment on cloud microphysics

Due to different treatments of aerosols in the two microphysics schemes, it is reasonable to expect that the largest discrepancies between WRF-AE and WRF-AI results would be for cloud variables such as cloud water and ice content, snow, hail, and rain. As cloud ice concentration highly depends on NIFA, so does the formation of hail and indirectly rain. Figure 3.25 shows the column integrated cloud ice concentration over the analyzed area. Both models identified the region southwest from Čačak as an epicenter of cloud ice formation at 15:00 UTC. The forecasts for 15:00 UTC are similar to each other, but the discrepancies start to be noticeable in the next 30 min. In the WRF-AE case, cloud ice is concentrated over relatively small areas south of Čačak and around Čačak. WRF-AI, on the other side, spreads the cloud ice over a larger area. The concentrations of cloud ice at 16:00 UTC above Čačak dropped approximately two times from the values at 15:30 UTC. Although the hailstorm was intense around Gornji Milanovac, both models gave small concentrations of cloud ice in that area (about 4 ice crystals per cm3 at 15:30 UTC).
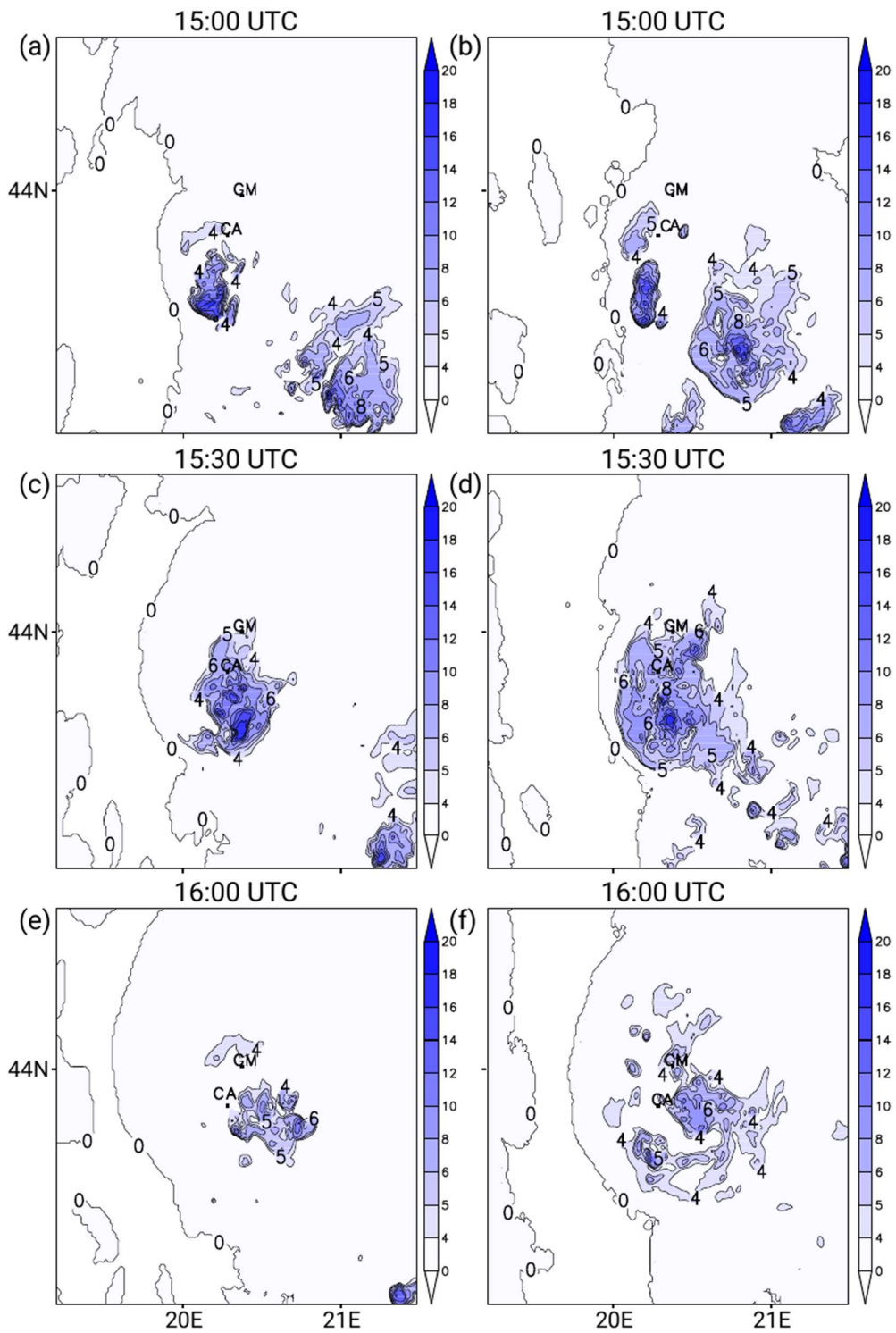
Figure 3.25 Time evolution of column-integrated cloud ice concentration (number of ice crystals per cm³) over central and west Serbia according to WRF-AE (left panels) and WRF-AI (right panels).

These findings are in accordance with the results in Figure 3.22, where both models greatly under-predicted the composite radar reflectivity in that area.
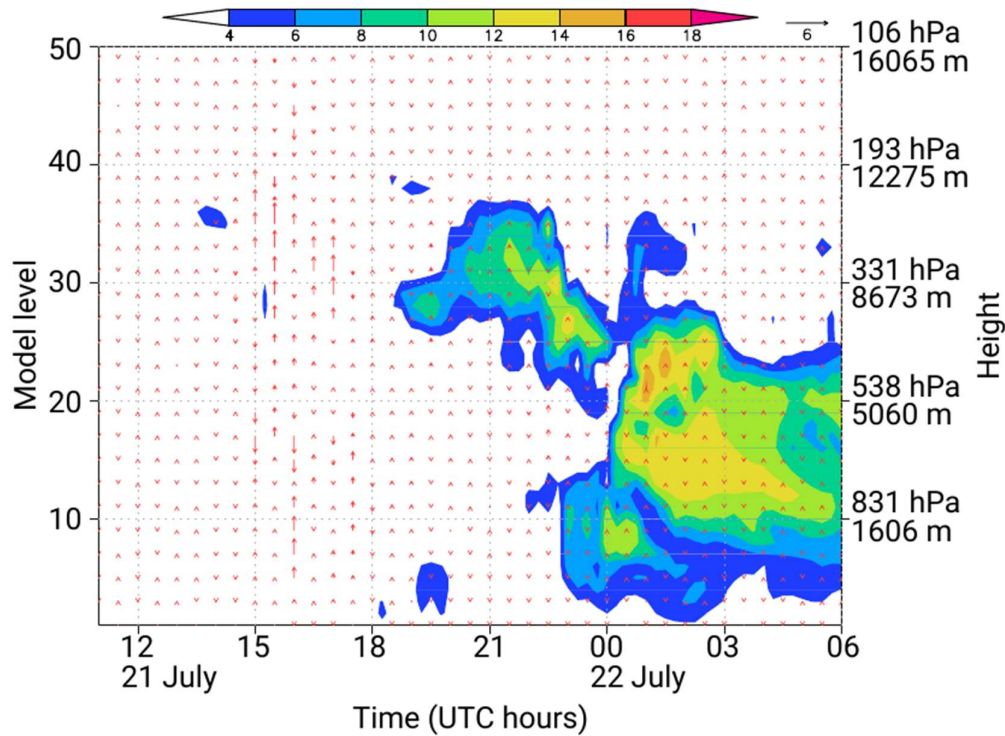
Figure 3.26 Time evolution of NIFA concentrations above Čačak between July 21 (11:00 UTC) and July 22 (06:00 UTC) based on the WRF-AE run. The primary y-axis shows the model levels, the secondary y-axis shows the corresponding geometric height and pressure, the red arrows indicate the vertical velocities in m s⁻¹ and the colors represent different concentrations of NIFA particles per cm³.

An 18-h long evolution of NIFA concentrations above Čačak is depicted in Figure 3.26. The concentration of NIFA close to the surface is around 2 particles per cm³ at all times. Until 15:00 UTC, the NIFAs were scarce at all levels (with the exception of a small higher-concentration area at approximately 10 km above surface). The intensification of convection between 15:00 and 18:00 UTC lifted the aerosols to upper levels of the troposphere (up to about 12 km).

However, this influx of NIFAs did not contribute to any significant precipitation due to the lack of convection at that time (Figure 3.26).

Figure 3.27 contains two views at the supercell storm at times when maximum damage was reported in Čačak and Gornji Milanovac regions. It can be seen that WRF-AI tends to produce ice in the west areas of the domain as well as in the south zones of the supercell. Although this cloud ice is not present in the WRF-AE simulation, the overall structure of the supercell are similar in both cases. The existence of ice phase in the upper regions of the cloud and well-developed thunderstorms are anticipated based on the satellite images in Figure 3.20d (deep convectiveand cold front at 12:00 UTC).
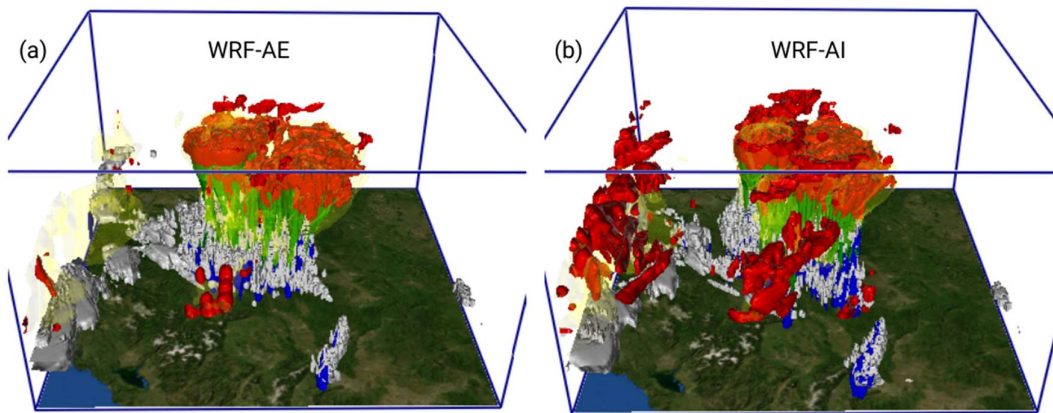
Figure 3.27 A view of the thunderstorm from south at 15:30 UTC according to (a) WRF-AE and (b) WRF-AI. Mixing ratios of cloud ice (red), cloud water (grey), snow (yellow) and rain (blue) are represented by the volume rendered field in VAPOR software (Clyne et al., 2007). Yellow color is set transparent and therefore may appear green when in front of blue (i.e. indicates the existence of snow in front of rain).

Advection of NIFA from west and southwest is shown in Figure 3.28a. These results are in accordance with the satellite observations in Figures 3.18 and 3.20. Figure 3.28a shows that large amounts of NIFA were located west of the supercell at the time of the maximum thunderstorm intensity. As showed earlier in Figure 3.26, these NIFA arrived in central Serbia after the strong convection and therefore marginally contributed to precipitation. At 15:00 UTC,

NIFA occupied large volumes of supercell, including the lower levels of the cloud. This abundance of NIFA at all levels is not visible in Figure 3.26, which indicates that NIFA concentrations close to the surface are highly localized and depend on topography. The increase o NIFA concentrations with height is also evident in Figure 3.28a (a transition from pink to purple color, i.e. from 2 to 7 NIFA per cm^3); in particular in the southwest corner of the domain. Trajectories in Fig. 3.28b show that WRF-AE accurately replicated the dynamics of this supercell. The precipitation zone is located in the northeast side of thunderstorm with the storm front underneath. The entrainment of moist air (rich with NIFAs) from the Adriatic Sea over the storm front is also visible. The orientation of the cloud top with an anvil-like shape is in the direction of the prevailing wind at upper levels (Figure 3.28).
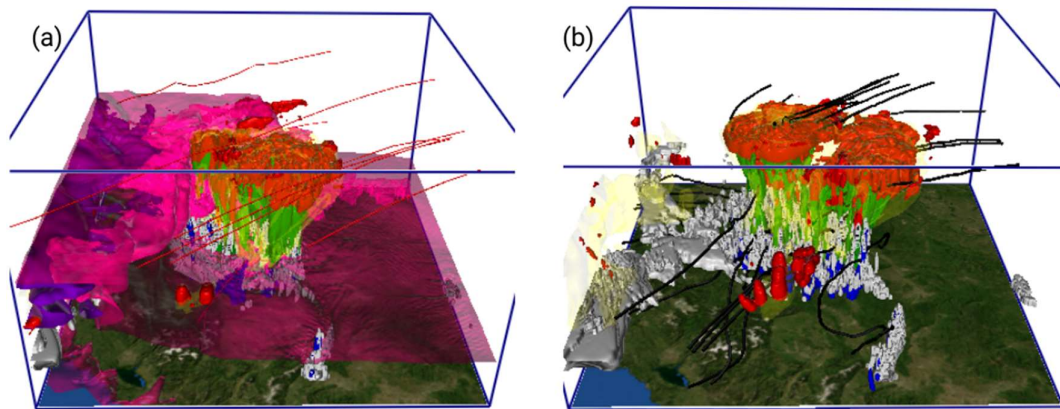
Figure 3.28 (a) Advection of NIFA at 15:00 UTC in WRF-AE is represented with pink color (2 NIFA particles per cm^3) and purple color (7 NIFA particles per cm^3). Air parcel streamlines are shown with the red lines. (b) The black lines depict several three-dimensional streamlines in WRF-AE at 15:45 UTC. Other colors as in Figure 3.27.

While both models captured the mesoscale dynamics of the analyzed event (Figure 3.20a,b), the differences on the smaller scales are noticeable. Compared to the WRF-AE case, the convective cells in the WRF-AI simulation are smaller and individually identifiable in Figure 3.21. This discrepancy between WRF-AE and WRF-AI results is probably caused by the explicitly modelled influx of NIFA in the WRF-AE case that enabled faster growth of Cb clouds. This intense

growth resulted in merging of individual cloud cells. The unsteady winds (in both speed and direction) and different microphysics processes in clouds tend to smear out the incoming aerosols (TE14) and therefore cloud cover in the WRF-AE case. The implicitly-modelled aerosols in the WRF-AI run lack this time dependent afflux of NIFA particles. As a result, the cloud cells are smaller than and not as developed in horizontal plane as in the WRF-AE case. Note that the merged cloud cover from WRF-AE run in Figure 3.21 resembles the satellite observations more closely than WRF-AI.

Both models shifted the locations of thunderstorms to the southeast from their satellite- and radar-identified locations in west and central Serbia (Figures 3.21 and 3.22). This difference is probably not caused by different treatment of aerosols, but inaccurate dynamics of WRF model in rugged regions of central Serbia. Ćurić et al. (2003, 2007) reported large differences between simulated Cb clouds in flat and complex terrains over Serbia. They concluded that orography plays a major role in cloud propagation over central Serbia. Crude mountains in WRF tend to underestimate the orography-induced drag and often result in overestimations of wind speeds in boundary layer (Milton and Wilson, 1996; Rontu, 2006; Jiménez and Dudhia, 2011). Under these circumstances clouds might be shifted in the downwind direction compared to observations (Ćurić et al., 2003). Coupling the TE14 microphysics with different PBL and/or land surface schemes might mitigate some of these errors (Cintineo et al., 2013). Interestingly, Cintineo and her colleagues reported the largest differences in cloud dynamics due to different PBL schemes in the afternoon. Our study confirms that the differences between forecasts and observations are larger than the differences between the two forecasts (TE14). Although surface precipitation measurements, radar calibration and satellite products contain a certain degrees of uncertainty, in the analyzed case, however, these uncertainties are arguably smaller than models inaccuracy. Figure 3.23 shows that WRF-AE gives more accumulated precipitation than WRF-AI, but the errors are not evenly distributed (Figure 3.29). Namely, WRF-AE greatly under-

predicts very light precipitation (0–12.3 mm in simulation period) and over-predicts light to moderate precipitation (12.4–24.5 mm in simulation period). WRF-AI shows better agreement with measurements for these two bins. Heavy precipitation, on the other hand, seem to be better forecasted by WRF-AE. WRF-AE errors in the forecasts of light precipitation have previously been reported by Qian et al. (2009), Sorooshian et al. (2010) and TE14. According to Sorooshian et al. (2010), WRF-AI produces thicker clouds which augment accretion of cloud drops by small raindrops and this characteristic of WRF-AI might be a reason for larger amounts of light precipitation. Also, an increase of aerosol concentrations generally tends to decrease and hinder precipitation in hallow clouds (Ackerman et al., 2003; Rosenfeld, 2006; Rosenfeld et al., 2008).
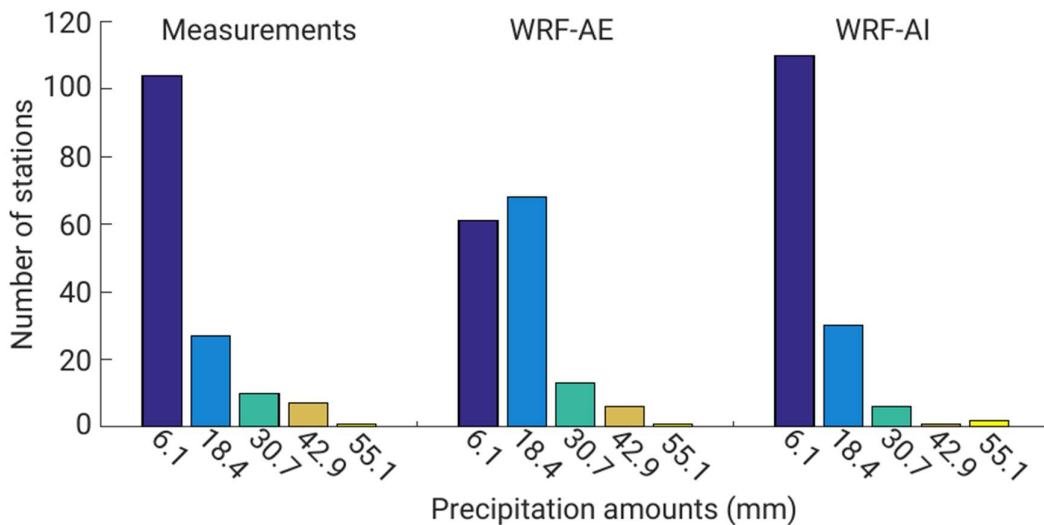
Figure 3.29 A count of total precipitation over the 24-h simulation for 149 stations in Fig. 1c. The width of bins is 12.3 mm and the bin centers are indicated on the horizontal axis.

Figure 3.30 sheds more light on the physical reasons behind the observed differences between WRF-AE and WRF-AI results. This discussion shall be focused on the time period between approximately 14:00 and 18:00 UTC (July 21). WRF-AE produced smaller amount of cloud water at 15:00 UTC, but larger amounts at around 17:00 UTC as well as delayed it for an hour compared to WRF-AI (Figure 3.30a). Both under-prediction and delay of formation of cloud

ice are also observed in Figure 3.30b, but the rain amounts, as previously mentioned, are larger in the WRF-AE case (Figure 3.30c). The vertical distributions of these water phases in the cloud are shown in Figures 3.27 and 3.28. These peculiar results might be explained as follows. The fewer ice crystals in the WRF-AE case (Figure 3.28b) result in their bigger size, which consequently increases their riming and aggregation efficiencies and produces more snow (Figure 3.30d). Similar results were reported in TE14.
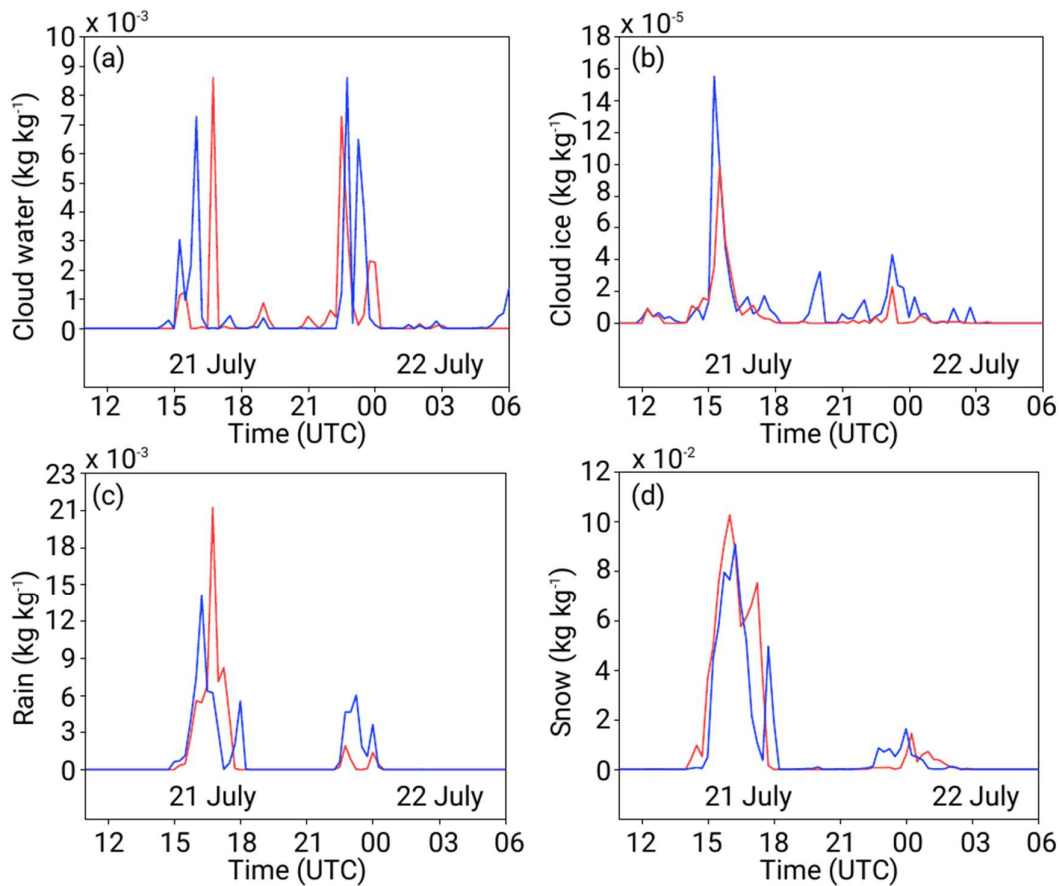
Figure 3.30 Mixing ratios (in kg kg−1) of (a) cloud water, (b) cloud ice, (c) rain and (d) snow in a vertical column of air above Čačak during the 18-h runs of WRF-AE (red lines) and WRF-AI (blue lines).

Aggregation, however, also increases with an increase of ice concentration (Hobbs et al., 1974) which prevented even larger differences between the modelled snows in these two cases. Moreover, effectiveness of the Wegener–

Bergeron–Findeisen process in mixed clouds increases with the decrease of the number of ice crystals, which also favored larger precipitation in the WRF-AE simulation. Since riming and collision are the most efficient processes in the formation of precipitation (e.g., Pruppacher and Klet, 2010), their increased effectiveness in the WRF-AE case resulted in more rain and hail. Note that strong updrafts in the supercell favored the development of large hailstones (Figure 3.17d). The above hypotheses, however, should not be straightforwardly applied to all cases as, for example, WRF-AI gave more precipitation than WRF-AE at around 23:00 UTC (July 21; Fig. 4c). Such diversity of results was also reported in TE14 and previously discussed by Tao et al. (2012). Explicit modelling of aerosols is a physically realistic approach.

As demonstrated in Figures 3.27 and 3.28 to some extent, this method enables reconstruction of aerosol concentrations in and around the cloud, the entrainment of aerosols in cloud, as well as their downwash with precipitation. With an increase of accuracy of this microphysics scheme and higher grid resolution in the smallest domain, such numerical products might be of practical significance for weather modification and hail suppression in particular.

CHAPTER 4

4 Methodology

4.1 1D MCSE model

4.1.1   Introduction

In this thesis, we developed a one-dimensional (1D) model for cloud seeding experiments (1D MCSE) with low computational cost. A bulk microphysics scheme developed by TE08 and TE14 for a NWP model WRF-ARW is modified by introducing two hygroscopic reagents: (1) sodium chloride (NaCl) and (2) core/shell NaCl/titanium dioxide (TiO$_2$) nanostructure (hereafter shell structured TiO$_2$/NaCl). Dynamics core of the 1D convective cloud model used in this study is adopted from Ćurić and Janc (1990) and Ćurić and Janc (1993a), and it is coupled with the TE14 scheme. One of the objectives here is to investigate the formation of microscopic cloud droplets on these two reagents and their further growth. The nucleation phase is described using a bin parcel model which integrates a system of five differential equations that describe evolution of an adiabatically lifted parcel (Pruppacher and Klet, 2010). Similar models are developed by Cooper et al. (1997), Saleeby and Cotton (2004), Drofa et al. (2010) and Rothenberg and Wang (2015). Then, the further growth of cloud droplets through the processes such as collision and coalescence is characterized using the double-moment microphysics scheme by TE14. At the end, accumulated surface precipitation is calculated for three cases: (1) no reagent added and the nucleation only takes place on the natural cloud condensation nuclei (CCN) explicitly modelled using the TE14 scheme (i.e., base case), (2) cloud seeded with NaCl particles plus natural aerosols, and (3) cloud seeded with the shell structured TiO$_2$/NaCl (novel) reagent plus natural

aerosols. Accumulated surface precipitations are calculated for these three cases and compared.

One approach to seeding parameterization is based on the treatment of a new seeding material as aerosols whose activation characteristics are derived from the results of the bin parcel model and experimental work by T17. Formation of cloud droplets by process of nucleation is explicitly treated. In the proposed model, the number of activated CCN is function of environmental temperature, vertical velocity, relative humidity, number of CCN in ascending volume of air, their geometry, and hygroscopic characteristics measured by a κ (kappa) parameter, which, in turn, is based on the κ–Köhler theory (Petters and Kreidenweis, 2007; Reutter et al., 2009; Ward et al., 2010). For non-hygroscopic particles $\kappa = 0$. If hygroscopic particles collect surrounding water vapor and locally decrease required supersaturation for activation of aerosol, then $\kappa > 0$. For instance, κ values are in the interval 0.5–1.4 for highly active salts such as NaCl (Petters and Kreidenweis, 2007).

The seeding particles of the shell structured $TiO_2/NaCl$ and the pure NaCl in the numerical experiments in this thesis had the initial diameter of 1.4 μm.

4.1.2 Model construction

1D MCSE model is result of coupling the dynamics of the 1D model proposed by Ćurić and Janc (1990) and Curić and Janc (1993a) with the TE14 microphysics model developed for WRF-ARW.

The TE14 microphysics scheme accounts for the heterogeneous nucleation evaluating the number of activated CCNs on natural aerosols in the atmosphere. The fraction of activated aerosols is calculated using the bin parcel model (zero-dimensional model) that provides the rate of change of the size of cloud drops that were formed on the natural aerosols, as well as the time evolution of the other meteorological variables in the rising parcel of air. At the end of the integration period, it is possible to determine the activated fraction of

aerosols that served as CCNs. Since the parcel model is rather computationally expensive to run in every integration step and in all grid points in the computational domain, the scheme uses the lookup tables for the number of activated aerosols as the function of ambient temperature, vertical velocity, relative humidity, and the number of naturally occurring aerosols in the atmosphere. This coupling between the microphysics scheme and the parcel model, as well as their further coupling with the dynamic core of 1D model proposed by Ćurić and Janc (1990) and Curić and Janc (1993a) is schematically portrayed in Figure 4.1.
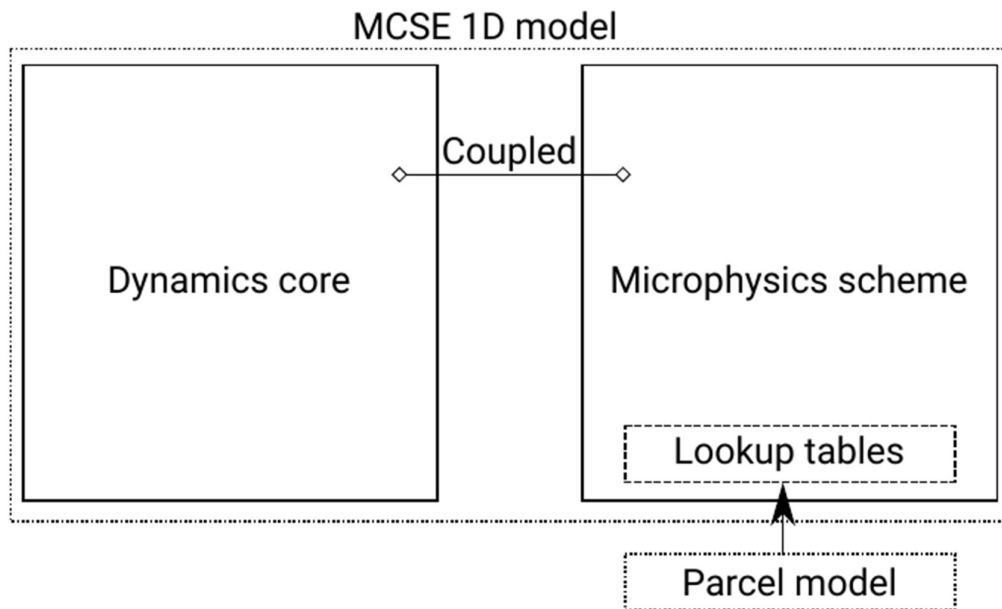
Figure 4.1 MSCE 1D model framework.

The vertical velocity in 1D MCSE model is calculated as in Ćurić and Janc (1990) and Curić and Janc (1993). The model also implements the forcing of vertical velocity in the first ten levels (i.e., first 2000 m) in a form of a positive branch of the sinusoidal curve (e.g., Ćurić, 1980; Curić and Janc, 1993a; Lompar et al., 2018). The dynamics, thermodynamics and continuity equations from Ćurić and Janc (1990) and Curić and Janc (1993a) are coupled with the microphysics of TE14.

4.1.3 Numerical experiments

Two numerical experiments were conducted with the goal to evaluate the performances of the 1D MCSE model and the microphysics characteristics of novel seeding reagent in comparison to pure NaCl.
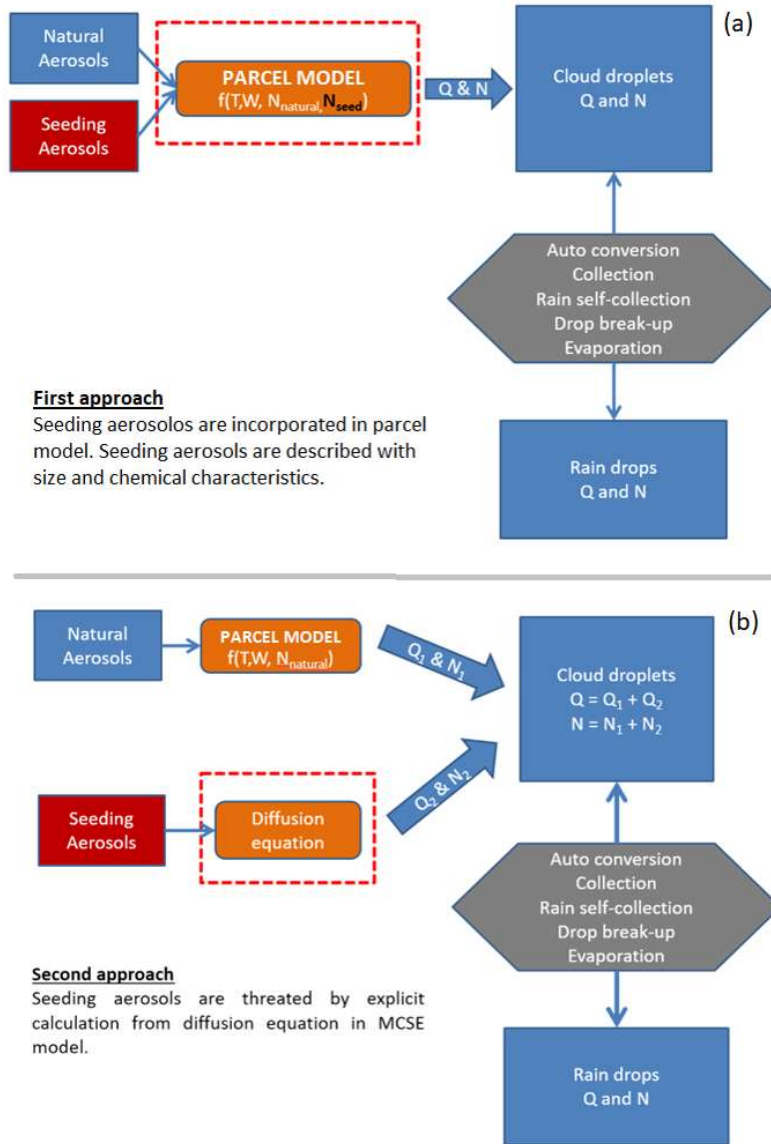
Figure 4.2 Flowcharts of two approaches used to numerically model shell structured TiO_2/NaCl and pure NaCl (seeding) aerosol in the MSCE 1D model.

The methodologies behind these two numerical experiments differ significantly and therefore they deserve further clarification. Figure 4.2 shows a flow chart of these two methods used to investigate the inclusion of the shell structured $TiO_2/NaCl$ reagent in the MSCE 1D model.

The first approach follows the methodology that deploys the parcel model in the TE14 scheme to evaluate the characteristics of the new reagent using lookup tables. This time, however, the lookup tables needed to account for the presence of both natural and artificial aerosols. It would be, of course, inaccurate to independently investigate the activation of natural from artificial aerosols (or vice versa) in the parcel model as both species of aerosols simultaneously compete for the available water vapor in the ascending parcel of air.
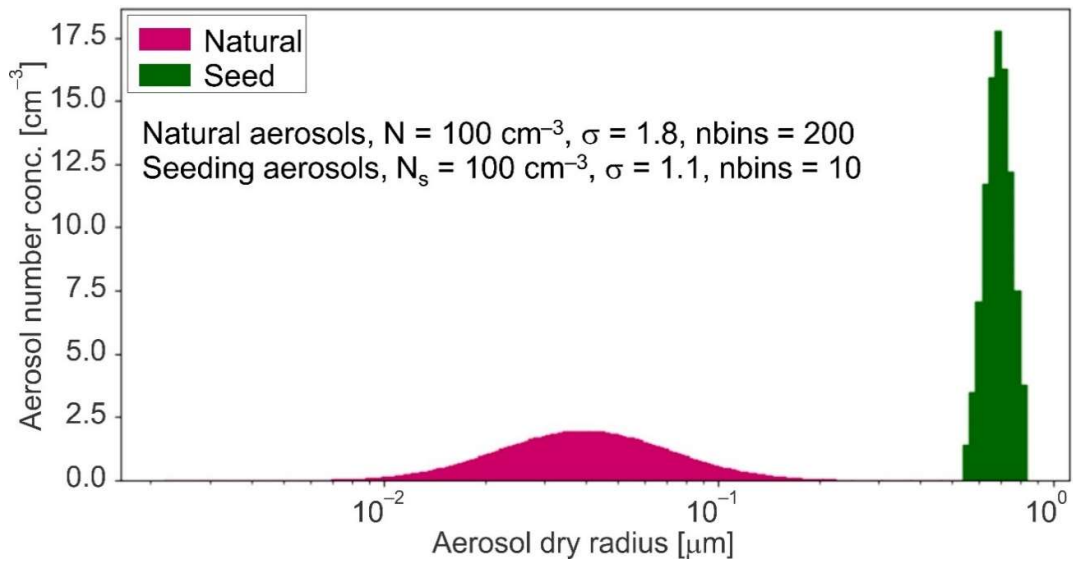
Figure 4.3 Distributions of natural and seeded aerosols in the parcel model for the same value of aerosol concentrations.

Therefore, the parcel model had to be re-run with the inclusion of the novel aerosols. As the result, new lookup tables were constructed that show the activated fraction (A) of natural and artificial aerosols. The size distribution of natural aerosols is typically described using some form of lognormal distribution (e.g., Junge, 1955; Twomey and Severynse, 1963), while the artificial

aerosols all have the similar (practically the same) and known size of 1.4 ± 0.3 µm in diameter (Tai et al., 2017). An example of these two distributions is shown in Figure 4.3, while the control parameters in the lookup tables are given in Table 2.

Table 2 Control parameters in the lookup tables in the used parcel model. N and N_s are the concentrations of natural and seeded aerosols, respectively, V is the ascending velocity of the parcel of air and T is the air temperature. Note that $N = N_s$.

N [cm^{-1}]	10	31.6	100	316	1000	3160	10000	–	–
V [m s^{-1}]	0.01	0.0316	0.1	0.316	1	3.16	10	31.6	100
T [K]	243.15	254.15	263.15	273.15	283.15	293.15	303.15	–	–
N_s [cm^{-1}]	10	31.6	100	316	1000	3160	10000	–	–

As evident from Table 2, all control parameters are considered in a wide range of values with the goal to construct lookup tables that can be applied in all areas around the world. Two lookup tables were constructed in order to distinguish between activation characteristics of natural and seeding aerosols in microphysics module. In addition, both lookup tables were formulated as three-dimensional matrices which required the usage of trilinear rather than bilinear interpolation for defining the activation function $A = f(T, V, N, N_s)$, where A takes values between 0 and 1.

The second approach to investigate the activation properties of the novel aerosol is depicted in the lower part of Figure 4.2. Recently, T17 showed that the unique physical-chemical characteristics of the shell structured TiO$_2$/NaCl make this seeding reagent superior to NaCl in unsaturated environments in particular. Despite this important characteristics of the novel aerosol, the activation properties of aerosols in the parcel method (Approach 1 in Figure 4.2), however, are calculated for the high values of relative humidity (~ 98%), which eventually exceeds 100% due to the adiabatic cooling in the ascending

air. For this reason, the second approach (Figure 4.2) to numerically analyze the performances of the shell structured TiO_2/NaCl considers the injection (i.e., seeding) of this aerosol in an unsaturated environment underneath the cloud. Recently, an airborne study of natural aerosols underneath cloud base was conducted by Semeniuk et al. (2014). This numerical approach is more accurate at evaluating the advantages of the novel reagent when compared to NaCl, or any other artificial aerosol for that matter, which only activates in the conditions close to saturation. Here, natural aerosols and the number of activated CCNs are treated as in the original TE14 scheme, while the activation of the novel reagent is calculated separately utilizing the diffusion growth equation in the 1D MSCE model and the data from laboratory experiments (T17). The diffusion growth in the 1D MSCE model for the shell structured TiO_2/NaCl and the pure NaCl is in the form:

$$\frac{dr}{dz} = C_1 V^{C_2} (RH - C_3)^{C_4} \tag{4.1}$$

where r is the droplet radius, z is the height, and RH is the relative humidity.

Table 3 The values of constants in the diffusion growth equation [Eq. (4.1)] obtained from the laboratory experiments of T17.

	NaCl	Shell structured TiO_2/NaCl
C_1	2.5×10^{-7} m/s	5×10^{-7} m/s
C_2	–1	–1
C_3	0.75	0.70
C_4	1.74	2.13

The values of constants and coefficients in Eq. (4.1) are determined form the laboratory experiments of T17 and are they are included in Table 3. Since $C_2 = -1$, Eq. (4.1) shows that the $\frac{dr}{dz}$ decreases with increasing the updraft speed. This

dependency is expected as the droplets have less time to grow in the strong updrafts. The physical meaning behind the coefficient C_4 is to implicitly depict the higher growth rate for higher values of relative humidity. The constant C_3 is the hygroscopic point of the two aerosols (T17). Lastly, the empirical constant C_1 represents the differences in the growth of the shell structured $TiO_2/NaCl$ and the pure NaCl, as obtained from Figure 3f in T17.

The κ parameter for the shell structured $TiO_2/NaCl$ is determined following the method proposed by Petters and Kreidenweis (2007):

$$\kappa = 1 - GF^3 + \frac{GF^3 - 1}{RH} e^{\frac{4 \cdot \sigma_s \cdot M_w}{R \cdot T \cdot \rho_w \cdot D \cdot GF}} \tag{4.2}$$

where $GF = \frac{D(RH)}{D_d}$ is the growth factor of the novel aerosol obtained by T17 in cloud chamber, $D(RH)$ is the droplet diameter as the function of relative humidity (RH), D_d is the dry dimeter of the aerosol, $T = 278.15$ K is the air temperature, $\rho_w = 1000$ kg m^{-3} is the density of water, σ_s is the surface tension on the solution (aerosol solution to air, 0.15 N m^{-1} for the novel aerosol), $R = 8.314$ J mol^{-1} K^{-1} is the universal gas constant, and $M_w = 18.01 \times 10^{-3}$ kg mol^{-1} is the molecular weight of water. Note that all investigated aerosols in the work by Petters and Kreidenweis (2007) had $\kappa < 2$. The laboratory experiments in cloud chamber conducted by T17 showed that $\kappa = 20$ for the shell structured $TiO_2/NaCl$. Obviously, the novel aerosol is an exceptionally hydroscopic substance with κ being one order of magnitude above the values of all previously known natural and artificial aerosols. The further investigation of chemical and physical properties of the shell structured $TiO_2/NaCl$ is beyond the scope of this thesis and the interested reader is referred to the recently published article by T17.

4.2 3D MCSE model

4.2.1 Introduction

Main goal of this thesis was to develop a 3D numerical model which will be capable to simulate weather modification process due to seeding with human made aerosols. Experiments with 1D MCSE has yielded promising results in the field of precipitation enhancement with novel seeding material, but it also had some drawbacks. The biggest drawback was insufficiently realistic representation of cloud dynamics related to the nature of 1D cloud models. The simplified dynamics in 1D MCSE reflected on the formation of precipitations through its impact on cloud microphysics. In addition, one can ask how applicable are results obtained from 1D model in reality. To overcome this limit, we developed the 3D MCSE version of the model. It is based on the WRF model. We made choice to use ARW variant of the model and to incorporate into it the knowledge we have gained working with 1D MCSE model.

Changing the model requires a lot of work and customization. Especially change from 1D to 3D model. Experiments conducted with 3D MCSE can be divided into idealized experiments, which purpose was to test model and verify that algorithm and methodology developed in 1D MCSE is successfully transferred into 3D MCSE and into real experiments, which purpose was to give answers to main questions of weather modification in realistic environmental conditions.

4.2.2 Model construction

To be able to simulate seeding experiments, a new 3D variable was added into 3D MCSE model following requirements of the model. It is variable which represents seeding material and is named seed aerosol number concentration (QNSEED). Its unit is kg^{-1}.

In order for the new variable to be transported and spread according to the model's dynamics, new variable was included in the same class of variables as

natural aerosols are included in TE14. To be able to use new variable in microphysical package dozens of model subroutines were changed. Seeding parameters for model run are provided through new constructed namelist.

Nucleation of natural aerosols in 3D MCSE is done using lookup tables. As a result of nucleation of natural CCN we have change in mixing ratio of cloud water and change in number concentration of cloud water droplets. Seeding aerosols are activated and grow according to diffusional equation which is based on laboratory measurements like in 1D MCSE model. Nucleation on seeding aerosols also change mixing ratio of cloud water and number concentration of cloud water droplets but rate of change depends weather salt or novel reagent is being used.

4.2.3 Numerical experiments

Idealized numerical experiments were conducted to test model and verify that algorithm and methodology developed in 1D MCSE, is successfully transferred into 3D MCSE. In order to conduct idealized tests we had to provide initial soundings and to initialize cloud formation with warm bubble, like the experiment with idealized three-dimensional quarter-circle shear supercell simulation which is a present option for the WRF–ARW model (Skamarock et al., 2008; Morrison and Milbrandt, 2010; Kalina et al., 2014; Zhao et al., 2015).

Idealized tests were conducted mainly to verify that artificial seeding material is transported in 3D MCSE model according to cloud dynamics and to verify that microphysical processes related to cloud seeding are well described in the model.

Real case experiments were conducted in order to test efficiency of seeding material in realistic conditions. The initial and boundary conditions for real case experiments are obtained from the Global Forecast System (GFS) model outputs with a 0.5° × 0.5° horizontal resolution for same test case as described in section 3.2 (Figure 3.17a) of this thesis. In order to simulate seeding process, instead of

one-way online nesting on all 4 domains, first 3 domains were run with one-way online nesting, and finest resolution domain (Figure 3.17b) was run as offline nest.

One of the important results from 1D MCSE model was consequence that seeding material should be introduced below the cloud base and that novel material has advantage over salt in the process of uplift in non-saturated environment as it is shown in the laboratory and past numerical experiments.

Basic idea in real case experiments was that seeding will be done by a plane flying beneath the cloud base and releasing new seeding particles. Than complex cloud dynamics will drag in into cloud new cloud droplets which were formed on seeding material. Seeding material was introduced into finest resolution domain. Seeding area was 400 square kilometers and material was released in layer from 800 to 1000 meters height in period of 10 minutes starting at 13 UTC. Seeding are is set over the (ČA) and (GM) regions (Figure 3.17c).

Analysis of accumulated precipitation and cloud ice were made to verify influence of seeding material in realistic conditions. Comparison of results gained by using NaCl and shell structured TiO_2/NaCl as seeding material was done.

CHAPTER 5

5 Results

5.1 1D MCSE model results

5.1.1 First numerical experiment

In this experiment, the performances of the 1D MSCE model are evaluated only for the case of natural and the shell structured $TiO_2/NaCl$ aerosols. Figure 5.1 shows the performances of the parcel model with the novel aerosol. The initial values at the beginning of the ascent are specified above the top panel in Figure 5.1. The air parcel started its ascent at a height where the supersaturation is –2% (i.e., relative humidity of 98%) and continues to rise for 800 s (total distance of 256 m). It is important to emphasize here that Figure 5.1 shows one seldom example from the lookup tables that contain 3087 entries.

Two panels in Figure 5.1 show the time evolution of mixing ratios of cloud water (Q_c) and water vapor (Q_w). As expected, Q_c grows with time (and height) and this growth is accompanied with the simultaneous decrease in Q_w due to the mass conservation restrictions imposed by the continuity equation for water vapor. These graphs demonstrates that the 1D MSCE model accurately preserves the total amount of water in the domain and is numerically stable for the inclusion of artificial aerosols with large values of κ, such as the shell structured $TiO_2/NaCl$. At the end of integration period of 800 s, the number of activated aerosols is 77 and 10 for natural and shell structured $TiO_2/NaCl$ aerosols, respectively. In other words, the activation efficiency of natural

aerosols for the given initial conditions is 7.7%, whereas the activated fraction of the seeded reagent is 100%.
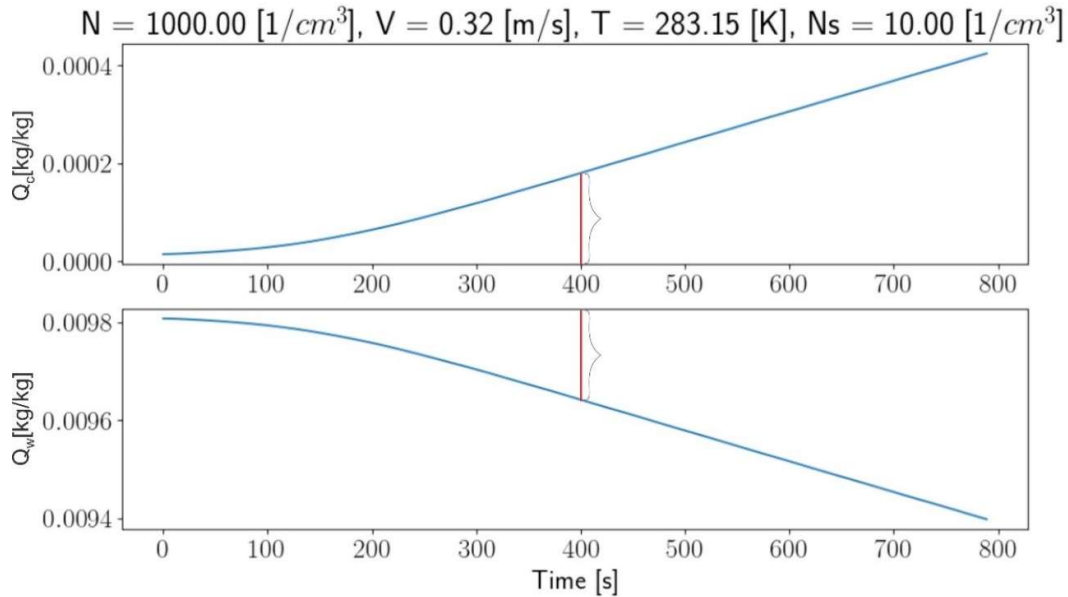
Figure 5.1 An example of time evolution of mixing ratios of cloud water (Q_c, top) and water vapor (Q_w, bottom) in the parcel model with the initial conditions shown above the top panel. The vertical red lines (same length) demonstrate that the MSCE 1D model preserves the total amount of water.

The growing diameter of droplets in the rising parcel of air is portrayed in Figure 5.1. In the investigated example, although the lognormal distribution has 200 bins (see Figure 4.3), Figure 5.2 depicts the growth of droplets in every 20th bin for simplicity. All shell structured $TiO_2/NaCl$ aerosol particles have almost the same dimeter of 1.4 µm and therefore they are represented with a single bin. Figure 5.2 shows that the growth of droplets is not uniform and depends on the initial CCN size. The smallest aerosols have the same size throughout the ascent (left part of Figure 5.2), whereas the larger aerosols increase their size as observed through the shift of the growth curves to the right. Figure 5.2 also demonstrates the double logarithmic growth of droplets larger than approximately 0.0115 µm in radius at the initial height. This rapid regime of growth is observed in the layer between 100 m and 150 m. As a consequence of this pronounced dependency between the growth efficiency and the initial

radius of aerosols, only 7.7% of the natural aerosols is activated. Once again, the activation rate for the introduced novel aerosol is 100%. In addition, Figure 5.2 demonstrates a narrowing of the drop size distribution as the growth proceeds with height. This separation of the lines in Figure 5.2 (with pronounced gap between the growth lines above the height of 125 m) is known as bifurcation.
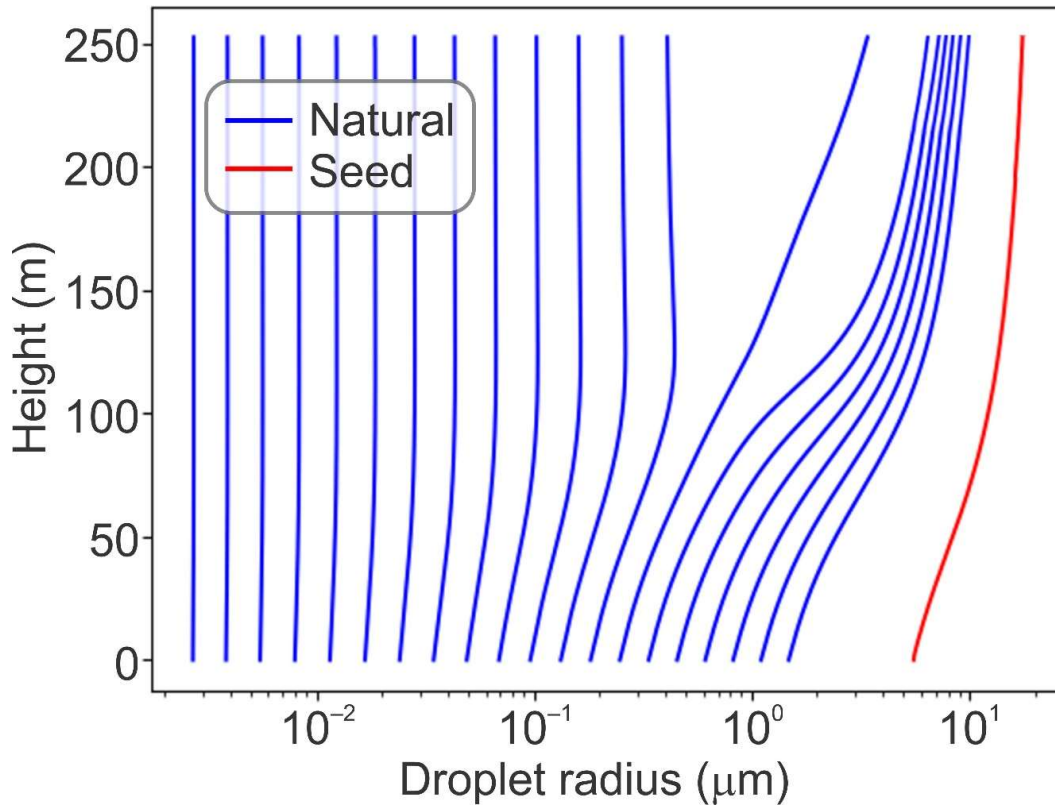
Figure 5.2 The dependency of droplet size on height in the ascending parcel of air for natural aerosols (blue) and the shell structured TiO2/NaCl (red). The initial conditions are specified in Figure 5.1.

Figure 5.3 shows the activation of CCNs in the 1D MSCE model as the function of N, N_s V, and T. It should be noted here that these results are a sample of three experiments extracted from the series of thousands of numerical experiments performed under various conditions. Figure 5.3a demonstrates that for the fixed values of N, N_s and V, all shell structured $TiO_2/NaCl$ aerosols are activated regardless of T. Air temperature, however, plays an important role in activation of natural aerosols.

(a) $N = 1000.0/cm^3, V = 0.32m/s, Ns = 10.0/cm^3$

(b) $N = 10.0/cm^3, T = 283.15C, Ns = 10.0/cm^3$

(c) $N = 1000.0/cm^3, T = 283.15C, Ns = 316.0/cm^3$
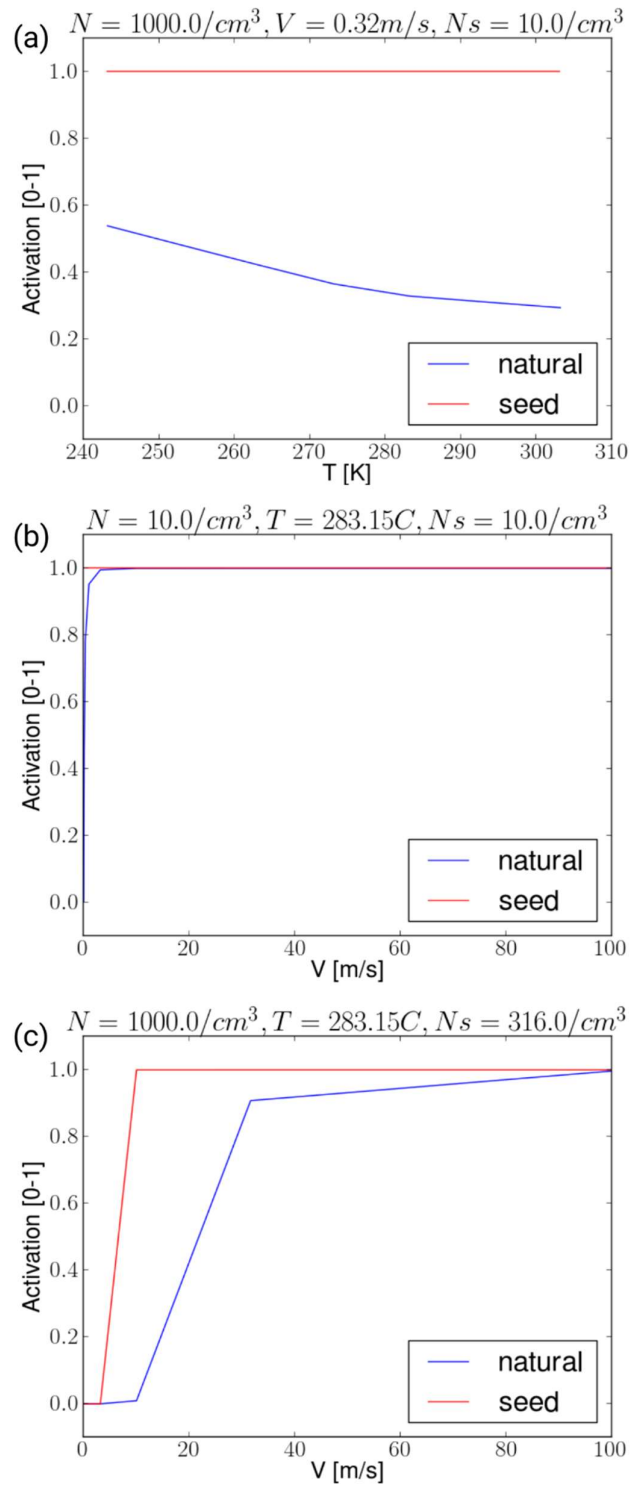
Figure 5.3 Activation fraction of natural (blue) and the shell structured TiO2/NaCl (red) aerosols as function of air temperature (a) and updraft velocity (b, c) for various initial conditions indicated above each figure.

Similar to this finding, Figure 5.3b further shows the clear activation independency of the shell structured $TiO_2/NaCl$ aerosol on vertical velocity. The complete activation of natural aerosols, on the other hand, is achieved only when the updraft velocity exceeds approximately 10 m s^{-1}. Overall, it can be concluded that for low concentration of natural and seeding aerosols (10 cm^{-1}) and high updraft velocities (above 10 m s^{-1}), the activation fraction of all aerosols is 1. Figure 5.3c describes the case with large number of both natural and seeding aerosols. Once again, the high activation efficiency of the novel aerosol is clearly shown when compared to natural aerosols. In this example, all natural aerosols activated only in the unrealistic conditions when the updraft velocity is around 100 m s^{-1}, whereas the shell structured $TiO_2/NaCl$ reagent is fully activated at approximately 10 m s^{-1}. The rapid growth of natural aerosols for the updraft velocities between 11 m s^{-1} and 30 m s^{-1} is also noticeable. To sum up, Figure 5.3 shows overall higher activation of novel aerosol than natural aerosols in all circumstances. A large number of similar numerical experiments (not shown), but with different combinations initial conditions for N, N_s V, and T has been conducted and the supremacy of the shell structured $TiO_2/NaCl$ over the natural aerosols has always been observed.

Determining the values of κ parameter for different aerosols and chemical compounds in laboratories is an experimental procedure (Petters and Kreidenweis, 2007; Irwin et al., 2010). Such an experiment was designed in order to determine $\kappa = 20$ for the shell structured $TiO_2/NaCl$ aerosol in T17.

Figure 5.4 numerically replicates this laboratory procedure for the wider set of conditions using the 1D MSCE model. In numerical model, the air parcel starts its ascent at the level where relative humidity is 10% and with the air temperature as in the cloud chamber ($T = 278.15$ K). The ascent continues until the level where the relative humidity is 85%. Figure 5.4 shows the GF of NaCl and a number of hypothetical aerosols with κ between 1.2 (NaCl) and 20 (shell structured $TiO_2/NaCl$). The novel seeding aerosol shows the superior GF

characteristics when compared to the traditional NaCl reagent. The enhanced *GF*-related performances of the shell structured TiO_2/NaCl to the pure NaCl were also demonstrated by T17.
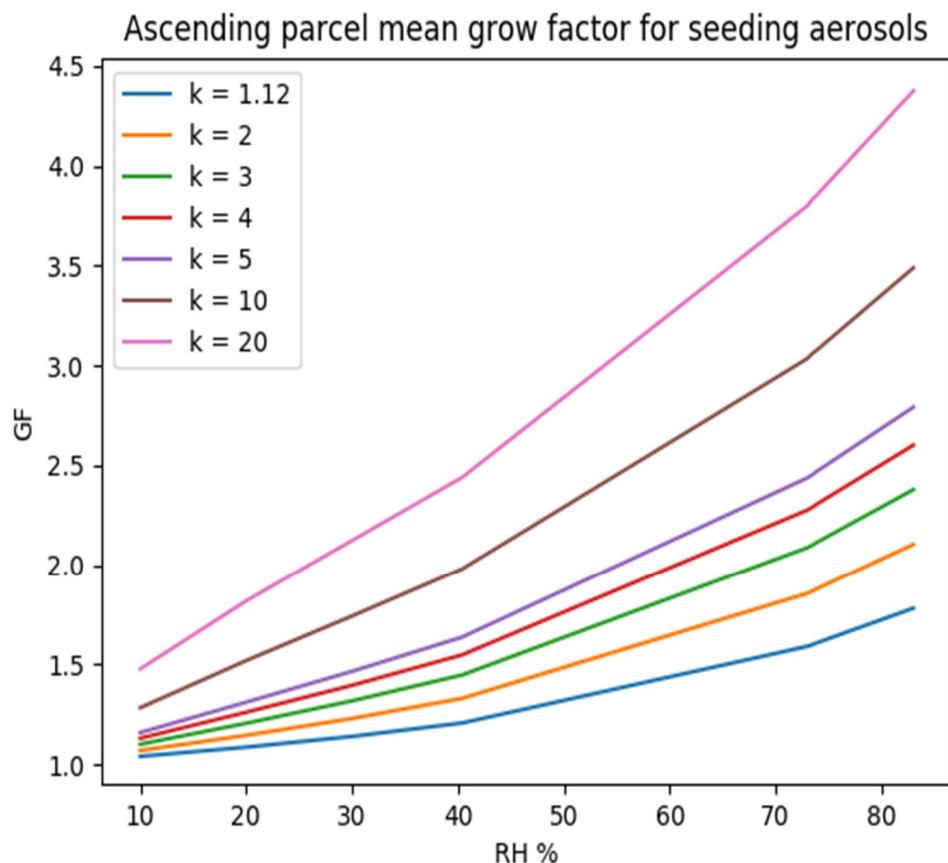
Figure 5.4 Growth factor (GF) as a function of relative humidity (RH) for different seeding aerosols. The novel aerosol (top pink line with κ=20) shows rapid growth in comparison with pure NaCl (bottom blue line with κ=1.12).

5.1.2   Second numerical experiment

As explicitly demonstrated in T17, the shell structured TiO_2/NaCl aerosol is particularly efficient in the sub-saturated environments where the relative humidity is around 75% (T17). For these reasons, a set of numerical experiments was performed using the approach schematically depicted in Figure 4.2 (Approach 2). In this approach, the shell structured TiO_2/NaCl is injected

underneath the cloud and naturally brought in the cloud within the updraft (i.e., not indirectly resolved in the parcel model as in the first approach). Following the experimental results of T17, it is expected that the novel aerosol and the pure NaCl have similar microphysics characteristics in the layers below the cloud where the relative humidity is less than approximately 50%. Between 50% and 70% of relative humidity, the new substance should grow faster, but not more than about 1.5 times faster than the pure NaCl. However, for the relative humidity of around 75% and above, the shell structured $TiO_2/NaCl$ should experience a threefold difference in the growth rate compared to NaCl.
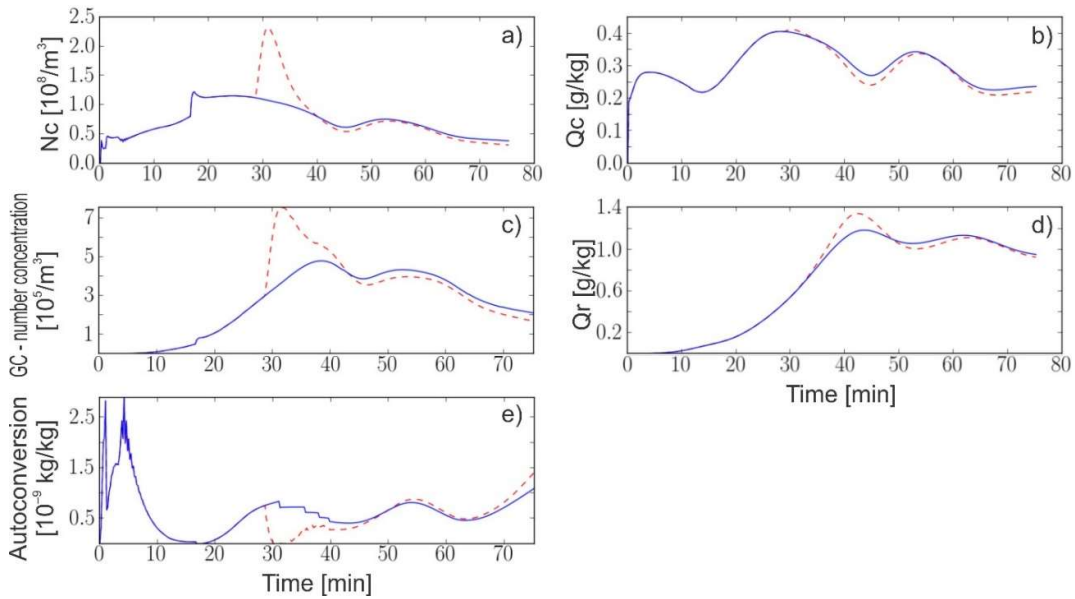
Figure 5.5 Evolution of different characteristics of cloud water (subscript c), rain water (subscript r), autoconversion and gravitational collection in 75 min of simulation with 1D MSCE model. The blue (full) lines represent the unseeded case and the red (dashed) lines correspond to the seeded case (shell structured TiO2/NaCl). These results correspond to the height of 2000 m above the lower cloud base.

Figure 5.5 shows the evolution of different cloud properties for unseeded and seeded cases. Note that the seeded case also contains the natural aerosols (as in the unseeded case) together with the shell structured $TiO_2/NaCl$. In this simulation, the seeding material is introduced 5 min after the simulation started

($t = 0$ s). It can be seen that the seeded (red lines) and the unseeded (blue lines) cases overlap until approximately $t \cong 35$ min when the deviations between the two cases become obvious. The initial overlap is due to the time that is needed for the seeding material to reach the cloud base. Underneath the cloud, the novel aerosol was already activated as CCN and the droplets were growing as a function of relative humidity until reaching the cloud base. At that moment, the droplets that grew on the artificial aerosol were added to the number of droplets that nucleated on the natural CCNs. As a consequence of this sudden increase in the number of cloud droplets close to the cloud base, the deviation between the unseeded and seeded cases is observed, as demonstrated in Figure 5.5 through the separation of blue and red curves.

In addition, it is observed that after $t \cong 35$ min the mixing ratio of cloud water (Q_c) first marginally increases and then slightly decreases compared to the base case (Figure 5.5b). However, the number of cloud droplets (N_c, Figure 5.5a) first increases significantly and then declines to approximately the level of the unseeded case. At the same time, the gravitation collection has increased profoundly, as shown in Figure 5.5c, which means that the rain drops have started to collect small cloud droplets and consequently the mixing ratio of rain (Q_r) increases too (Figure 5.5d). Also note that mixing ratio of autoconversion (Figure 5.5e) is lower in the seeded cases.

As demonstrated in Figure 5.6, the arrival of activated CCNs in cloud in the seeded case considerably increases the concentration of cloud droplets (N_c). This increase is predominantly observed close to the lower base of the cloud as seen in Figure 5.6a,b (e.g., Figure 5.6a shows a twofold increase of N_c). As a consequence of this rapid increase of N_c, the spectra of the size of cloud droplets also gets altered (Figure 5.6b). This broadening of droplet size distribution at the cloud base is not simultaneously observed at a height of 1 km above the cloud base as the activated cloud droplets on seeding aerosols have not yet been raised through the updraft to that level (Figure 5.6c). The width of the spectra

increases towards the small droplets which ultimately contributes to the increase of the diameter of rain drop through the process of gravitational collection.
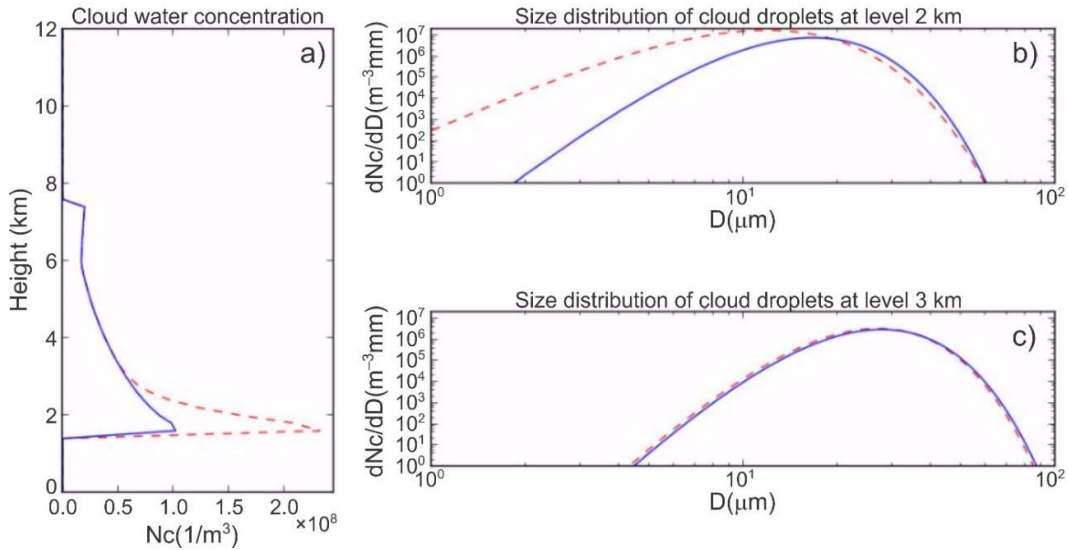
Figure 5.6 (a) Vertical profile of cloud droplet concentration at $t = 28$ min for natural (blue) and novel (red) aerosols and their size distributions at clod base (b) and 1 km above cloud base (c).

This dependency is demonstrated by observing the abrupt increase of the number concentration of gravitational collection in Figure 5.5c, which in the time domain follows the arrival of activated CCNs at the cloud base (Figure 5.6b,a). Moreover, this causal relationship is further reflected as the decrease of Q_c (Figure 5.5b) and the increase of Q_r (Figure 5.5d). The autoconversion of the remaining cloud droplets decreases in the seeded case because the remaining droplets (the one that were not gravitationally collected) are very small for the process of autoconversion to be efficient.

Figure 5.7 is a typical output of the 1D MSCE model and shows the evolution of the accumulated surface precipitation over time. In the two seeded cases, the number of introduced artificial aerosols is 10,000 cm^{-3} per integration time step (12 s). The seeding is conducted in the time window between 4 min and 8 min from the start of the simulations. The seeding height is 200 m above the ground

and the seeding material is injected in the updraft below the modelled cloud. It can be seen that the pure NaCl also contributes to precipitation enhancement, as has previously been demonstrated in the number of studies (Kristensen et al., 2014; Neukermans et al., 2014). However, the novel seeding material significantly increases surface precipitation when compared to pure NaCl case.
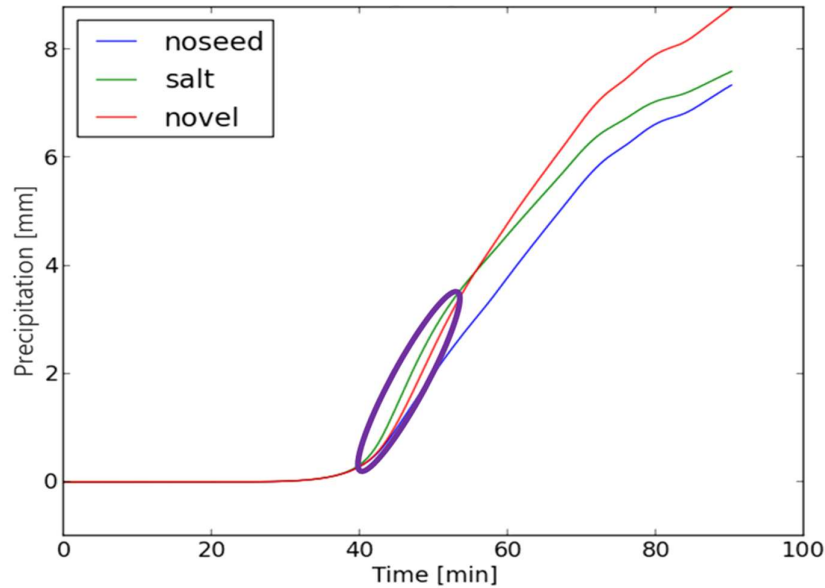
Figure 5.7 Evolution of the accumulated surface precipitation for the unseeded case (blue) and two seeded cases: (1) pure NaCl (green), and (2) shell structured TiO2/NaCl (red).

At the end of simulation ($t = 90$ min), the shell structured $TiO_2/NaCl$ produced approximately 3 and 4 mm m^{-2} more surface precipitation than the pure NaCl and unseeded cases, respectively. Interestingly, in the first 15 min after the precipitation started (40–55 min of integration time; circled area in Figure 5.7), the seeding with pure NaCl results in more surface precipitation, but afterward the novel reagent increases the accumulated precipitation significantly. The reason for this initial increase of precipitation in the NaCl case is further investigated in the next paragraph. It should be noted that similar results are observed when the same experiment is repeated with the reduced number of seeding material from 10,000 cm^{-3} to 1,000 cm^{-3} (not shown).

When looked through the microscope, aerosol particles in the atmosphere have widely variable shapes (e.g., Sinha and Friedlander, 1985; Wise et al., 2007) and the relationship between the aerosol activation and its shape is a complicated one (e.g., Lazaridis et al., 1992; Lin et al., 1993; Lazaridis et al., 2000). As demonstrated above and by T17, NaCl is not particularly active at the low values of relative humidity and therefore the aerosol preserves the cubical or irregular shape in the updraft for a long time. The shell structured $TiO_2/NaCl$, on the other hand, is highly active aerosol at the values of relative humidity for which the pure salt is inactive. Due to this high activation efficiency of the novel seeding material, this aerosol acquires spherical shape because of the thin film of water encapsulating it after the activation. Drag coefficient for three-dimensional cubes is about 2.3 times higher than for spheres (Potter et al., 2016), in the cases when the Reynolds number is above 10^4. Due to the larger drag, the pure NaCl gets transferred into the cloud faster than the shell structured $TiO_2/NaCl$ and, as the result, it starts enhancing precipitation before the novel aerosol. This shape dependency is parametrized in the 1D MSCE model as:

$$V_t = kD^c \tag{5.1}$$

where k is the shape parameter (150 and 350 for NaCl and the shell structured $TiO_2/NaCl$, respectively), D is the aerosol diameter and $c = 0.31$ is an empirical constant. Note that the ratio of the values of k (i.e., 2.3) correspond to ratio of the drag coefficients for the cube and sphere, as discussed above. determine the best height at which the seeding material will be dispersed in the environment, as well as the right interval of time over which the seeding will be conducted. This dependency is known as the spatiotemporal windows.

Figure 5.8 portrays three windows with the spatial variability of the release of the seeding material (i.e., 200, 400 and 600 m above ground). In all cases, the introduced amount of seeding material is 1,000 particles cm^{-3} per integration time step (12 s). In time domain, the seeding window starts with the width of 4

min (from 4 to 8 min into simulation) and increases accordingly as shown in Figure 5.8. The surface precipitation after 90 min of simulation time is compared between the three investigated cases.
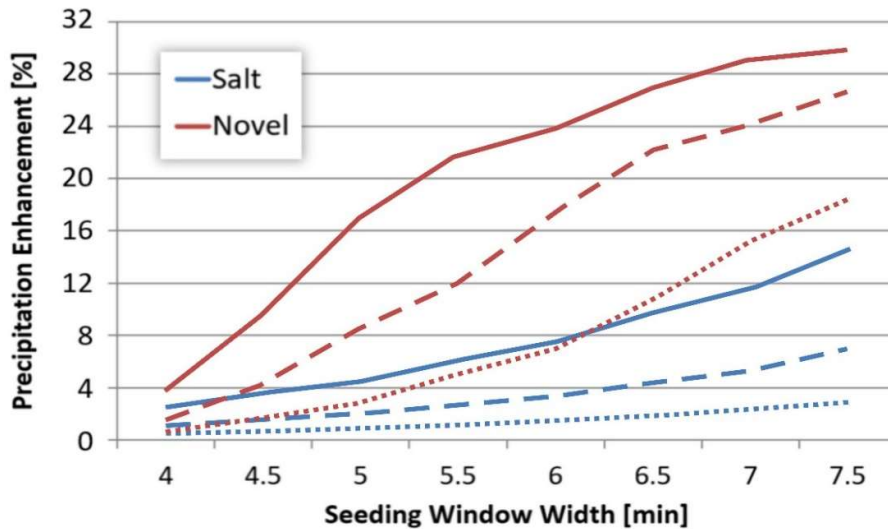
Figure 5.8 Precipitation enhancement as a function of spatiotemporal windows for pure NaCl (blue) and shell structured TiO2/NaCl (red) aerosols. The seeded particles are injected at 200 m (full lines), 400 m (dashed lines) and 600 m (dotted lines) levels.

One of the most important factors for the successful cloud seeding is to For example, the pure NaCl enhanced the accumulated surface precipitation for approximately 2%, whereas the increase of about 4% is observed for the novel aerosol when the time window is 4 min and the seeding height is 200 m (the first points on precipitation lines in Figure 5.8). Analyzing the same case, but increasing the time window from 4 to 4.5 min results in an increase of precipitation of 4% and 10% for pure NaCl and the shell structured TiO_2/NaCl, respectively. When the aerosols are released at 200 m for 7.5 min, the overall increase of surface precipitation by using the novel aerosols is more than 15% compared to the pure NaCl and about 30% more than in natural case.

Further analysis of all other cases depicted in Figure 5.8 show exponential (full red line in Figure 5.8) and logarithmic (dashed red line in Figure 5.8) trends of

precipitation enhancement using the novel seeding aerosol. This trend clearly shows the benefits of injecting the novel aerosols at lower levels. The increase of surface precipitation for NaCl is always linear, as well as for the shell structured TiO_2/NaCl when the reagent is injected at 400 m, but the slope of the linear line associated with the novel aerosol is approximately five times larger. Moreover, it should be noted that the increase of the height from 200 m to either 400 m or 600 m respectively diminishes the efficiency of precipitation enhancement because the seeding material has less time to grow in the updraft. The higher the layer at which the seeding material is released, the smaller the differences between the accumulated precipitations enhanced using the novel aerosol and pure NaCl. Lastly, it should also be pointed out that the increase of the time window is directly proportional to the amount of used seeding material, which consequently would increases the economic costs of the precipitation enhancement project.

5.2 3D MCSE model results

5.2.1   Idealized case results

To verify that the model can be used for seeding experiments in real atmosphere, we first verified complexity of cloud dynamics in 3D MCSE model and then verified that the model credibly simulates the transport and the spread of the reagent as a passive substance. We conducted several experiments with idealized version of 3D MCSE model. Atmosphere was initialized with synthetic soundings and cloud was initialized with warm bubble initialization method. It is obvious that we got real cloud dynamics by looking at relative vorticity in the cloud and in streamlines.

Figure 5.9a represents magnitude of 3D relative vorticity in the cloud. Process of splitting can be observed and it happens because of vertical wind shear in the input sounding. Figure 5.9b represents 3D flow with streamlines and we can see strong uplift in the cloud.
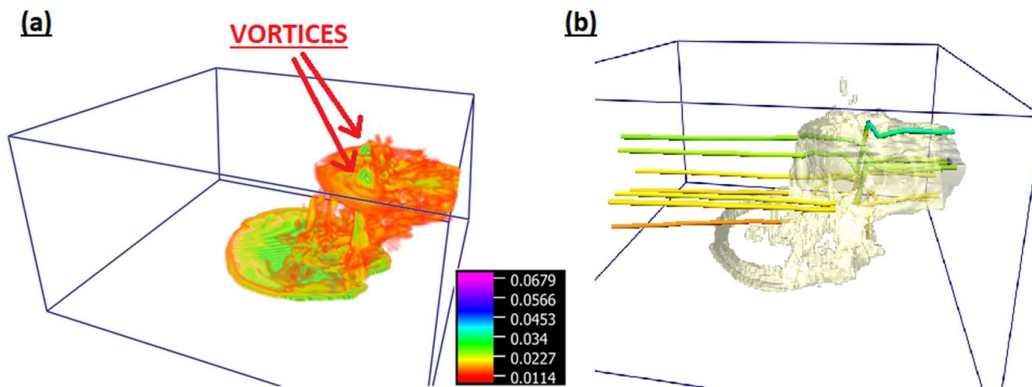
Figure 5.9 (a) Magnitude of relative vorticity in 3D MCSE model 1 hour and 10 minutes after start of simulation. (b) Flow represented by streamlines colored by temperature.

In the following experiments seeding material was introduced into the model as a trail of seeding material in front of the cloud, perpendicular to the direction of the cloud movement. This way we simulated airplane flight and releasing of material (Figure 5.10).
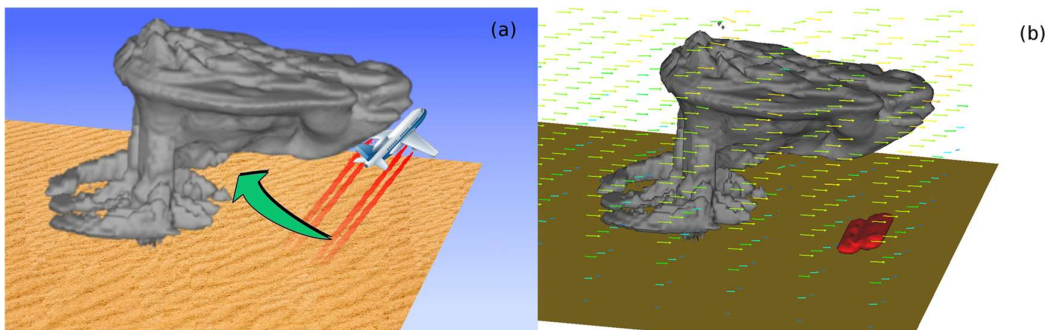
Figure 5.10 (a) Cloud seeding with airplane – scheme, (b) seeding material in model (red color) few minutes after airplane passed.

Figure 5.11 represents the process of cloud development, and transportation and spreading of seeding material for the passive case. Passive case means seeding material cannot interact with microphysical components and is just transported and spread with model dynamics. Seeding material is introduced in front of the cloud system and as time passes, we see that wind spreads seeding material (40 minutes after start of the experiment, until 90 minutes of the experiment), until cloud's updraft zone does not catch the reagent. When cloud's updraft zone catches reagent we have fast and strong uplift of reagent

into cloud and spreading at the cloud top due to divergence (period 90 minutes from start of the experiment, until 110 minutes of the experiment).
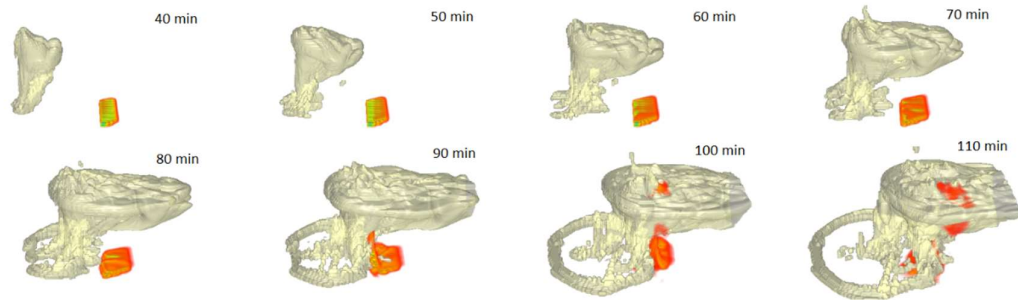
Figure 5.11 Development of the supercell cloud (grey color is cloud fraction isoline value 0.3), and transport and spreading of seeding material as passive substance.

An experiment was conducted to show that seeding material is spent in the process of cloud nucleation. Same microphysical algorithm was used as in 1D MCSE, to be able to compute nucleation of cloud droplets on new seeding material. In Figure 5.12 we can notice that seeding material is spread with horizontal wind until cloud's updraft zone catches seeding material as before, but then material is lifted through the cloud base and then it has converted to cloud droplets.
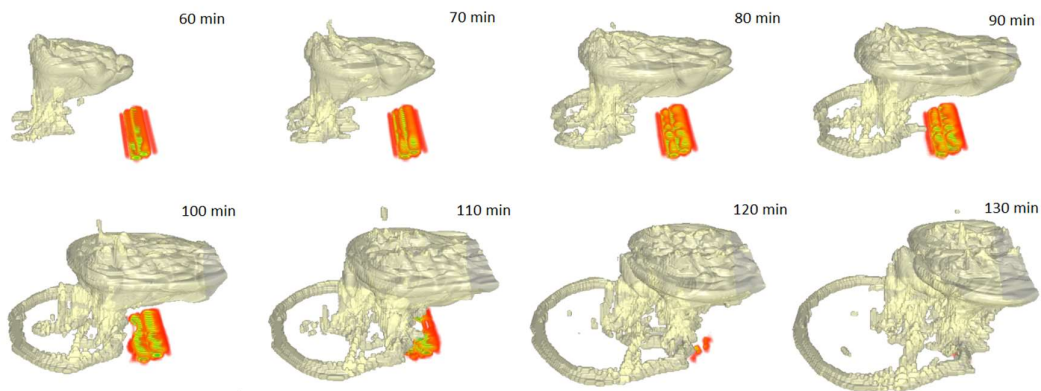
Figure 5.12 Development of the supercell cloud and transport and spreading of seeding material as active substance (same as Figure 5.11).

Changes in microphysical parameters are also examined due to process of nucleation of cloud droplets on novel seeding material in idealized case (Figure 5.13).
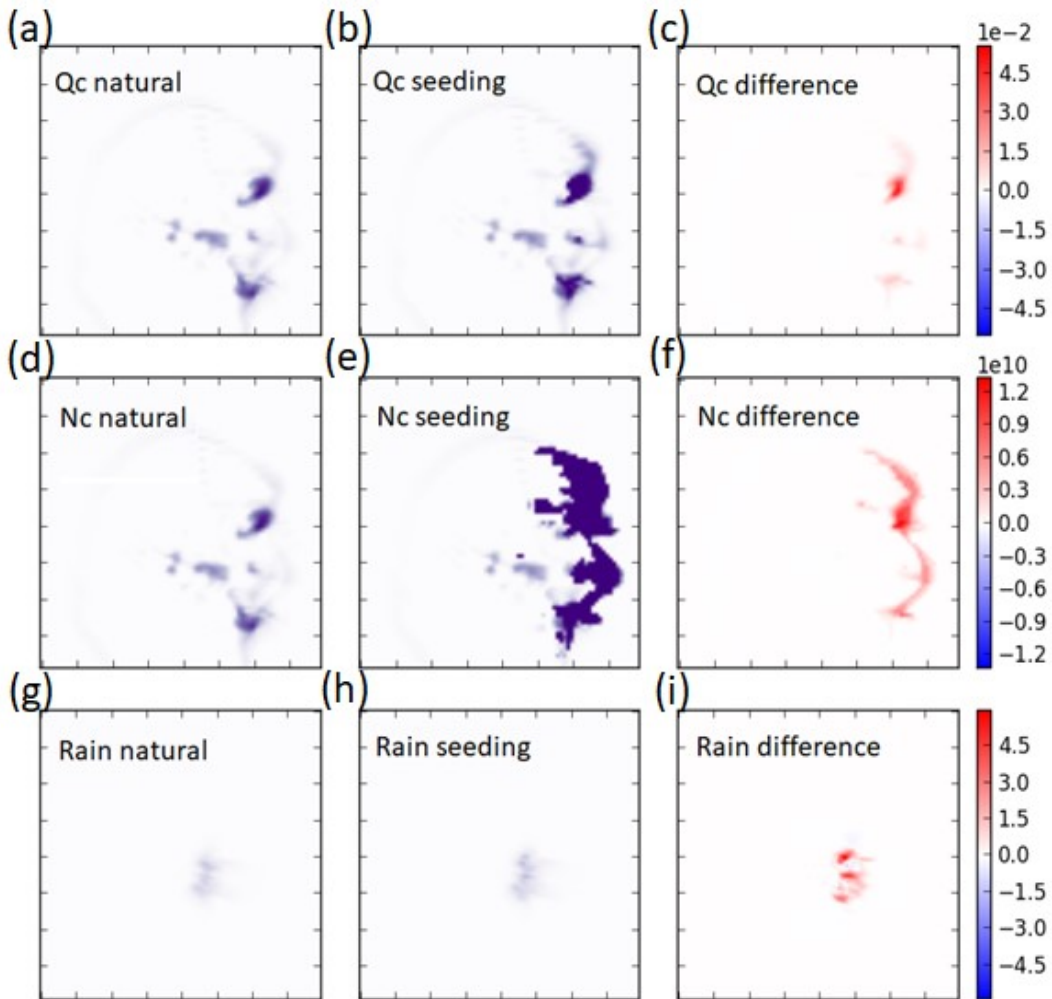
Figure 5.13 Panel of column integrated cloud water mixing ratio Q_c, column integrated number concentration of cloud droplets N_c and Accumulated rain in: unseeded (natural) experiment, seeded experiment and difference of two experiments after 90 minutes of model run.

Figure 5.13a is sum of cloud water mixing ratio in vertical column in unseeded experiment (Qc natural), Figure 5.13b represents same variable for seeded experiment (Qc seeding) and 5.13c is difference of those two variables (Qc difference). We can observe slight increase in cloud water mixing ratio in model due to seeding process. Figure 5.13d represents sum of number concentration of cloud droplets in vertical column in unseeded experiment (Nc natural), Figure

5.13e represents same variable for seeded experiment (Nc seeding) and 5.13f is difference of those two experiments (Nc difference). We have significant increase in number concentration of cloud droplets due to seeding process (darker color mean greater number and greater area coverage is noticeable). Figure 5.13g represents accumulated rain in unseeded experiment (Rain natural), Figure 5.13h represents same variable for seeded experiment (Rain seeding) and Figure 5.13i is difference of those two experiments (Rain difference). Increase in accumulated precipitation (red color) is obvious.

5.2.2   Real case results

Three experiments were conducted to show influence of NaCl and CSNT seeding materials on rain formation process. First experiment is only with natural aerosols (unseeded experiment) and is used as base for comparison with seeded experiments. In the second experiment natural aerosols and NaCl as seeding material were used, and in third experiment natural aerosols and CSNT material are used. Seeding was done over area of 400 square kilometers and material was released in layer from 800 to 1000 meters height in period of 10 minutes starting at 13 UTC. Seeding are is set over the (ČA) and (GM) regions (black rectangle on Figure 5.14).

Figure 5.14 represents accumulated precipitation and difference of accumulated precipitation for July 21, 2014 for period from 00 to 18 UTC for all three experiments. Figure 5.14a represents accumulated precipitation for unseeded experiment. It is noticeable that most rain felt on western part of computation domain. After inclusion of NaCl reagent as seeding material widening of precipitation area can be observed north of seeding area (5.14b) and same can be seen on accumulated rain difference plot (Figure5.14c) where red color represents increase in precipitation due to seeding process and blue color represents decrease in precipitation.

Accumulated rain due to CSNT seeding (Figure 5.14d), covers nearly same area as with NaCl (Figure 5.14b) but increase in precipitation can be observed in Figure5.14e where darker red color means more precipitation was formed.

Looking at difference of accumulated precipitation (Figure 5.14c,e) once can notice that there are areas with decrease of precipitation due to seeding process.

Pattern of light blue and light red colors signifies same intensities and they shows displacement of rain in southern part of domain.
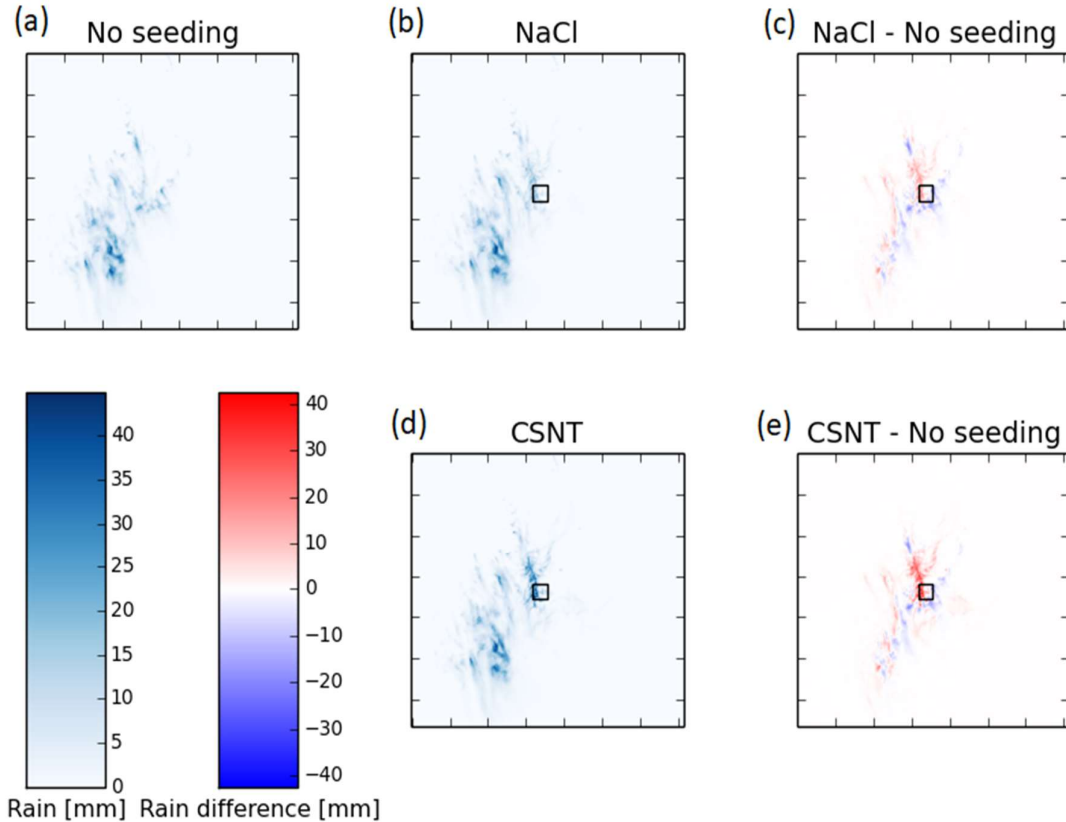
Figure 5.14 Accumulated precipitation for July 21, 2014 for forecast period 00-18 UTC for unseeded experiment (a), for NaCl seeded experiment (b), for CSNT seeded experiment (d), difference of accumulated precipitation for NaCl seeded experiment versus unseeded experiment (c) and for CSNT seeded experiment versus unseeded experiment (e). Black square represents seeding area.

Detailed comparison of accumulated rain for NaCl seeded and CSNT seeded experiments can be seen on Figure 5.15. More precipitations is formed due to use of CSNT as seeding material instead of pure NaCl. Maximal difference in precipitation is 15 litres per square meter in this forecasted period. Results obtained with 3D MCSE are in agreement with the results from 1D MCSE where we also obtained more precipitation in seeded experiments, and better performance was achieved with use of CSNT as seeding material.
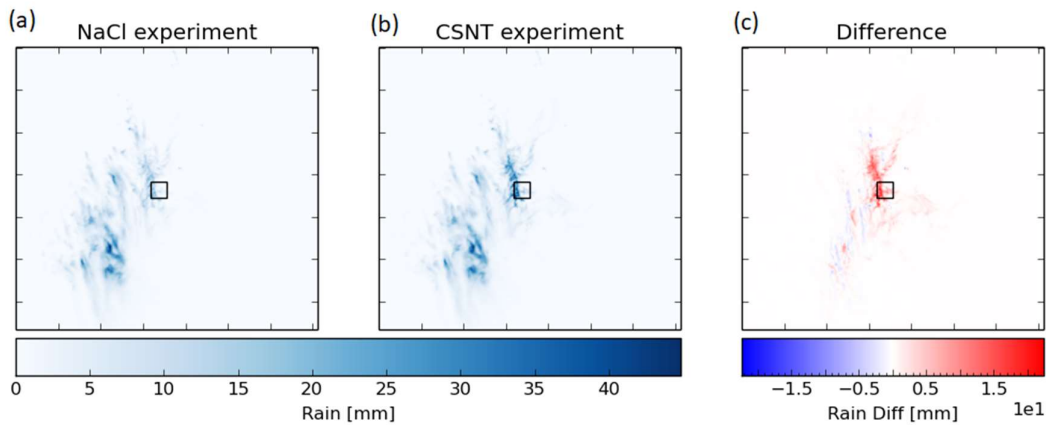
Figure 5.15 Comparison of accumulated precipitations for NaCl and CSNT experiments. (a) NaCl experiment, (b) CSNT experiment, (c) Difference of CSNT and NaCl experiment precipitations.

Time evolution of sum of accumulated precipitations over domain d4 in all three experiments is shown in Figure 5.16. The rain started after 12 UTC, and seeding material was introduced into model at 13 UTC. After seeding material is introduced we can see increase in precipitations. It is obvious that CSNT produced more rain and this is in agreement with 1D MCSE model.
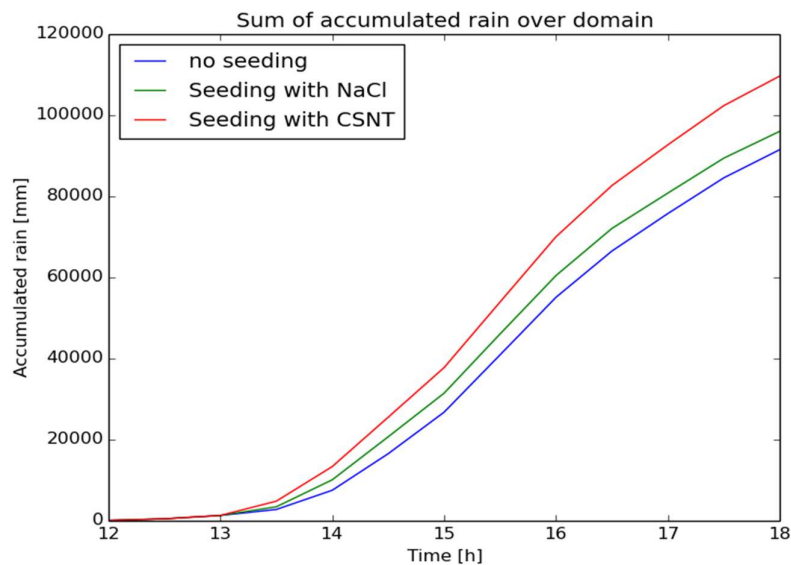
Figure 5.16 Sum of accumulated precipitations over domain d4. Blue line represents unseeded experiment, green line is NaCl seeded experiment and red line is CSNT seeded experiment.

Precipitation increase due to seeding is not evenly distributed. Precipitation footprint in the case of NaCl seeding and CSNT seeding is larger than in unseeded experiment. That can be observed through decrease in area without rain (<0.01 L). Increase in light, moderate and heavy precipitations is noticeable for both NaCl and CSNT seeding material. The greatest increase is within light precipitations area but increase in all categories is noticeable.
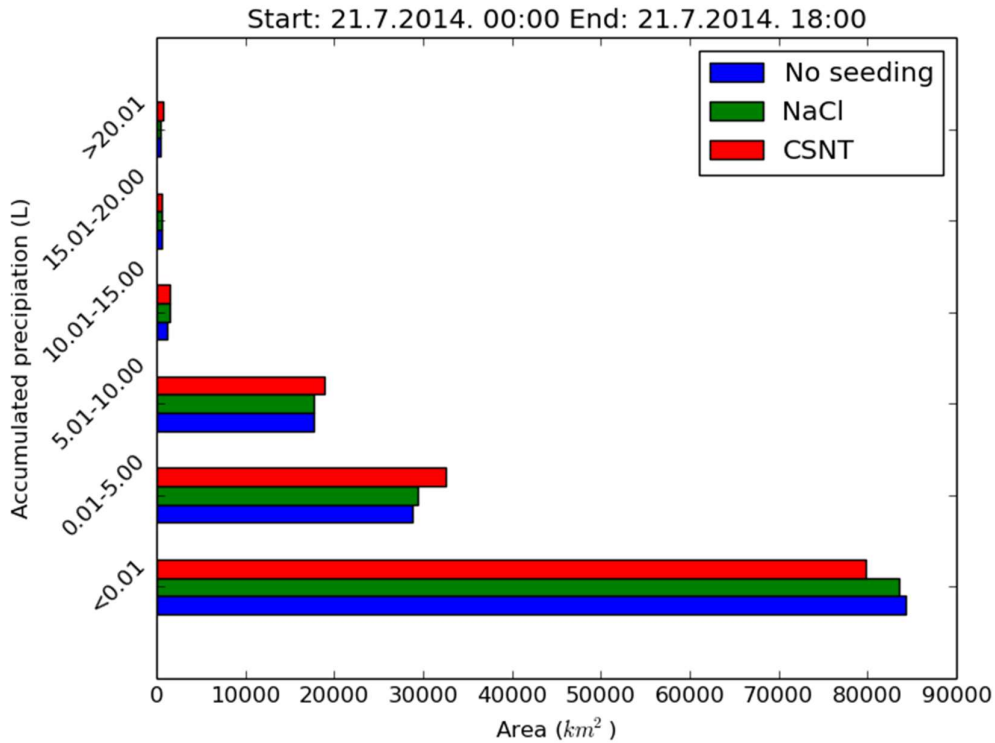
Figure 5.17 Histogram of different precipitation amounts in the case with unseeded (blue), NaCl seeded (green) and CSNT seeded (red) experiments.

Even NaCl and CSNT serves as CCN aerosols that does not mean that ice phase will not be modified. It is well known that microphysical interactions in a cloud are very complex and changes in cold type precipitations are expected. Column integrated cloud ice concentration for July 21, 2014 at 15 UTC for unseeded experiment is shown in Figure 5.18a. Figure 5.18b and Figure 5.18d are column integrated cloud ice concentration for NaCl seeded and CSNT seeded experiments respectively. Blue color in Figures 5.18c and 5.18e means decrease in cloud ice concentration and red means increase in cloud ice concentration. The plot legend indicates that local decrease and increase of cloud ice

concentration is of the same magnitude as total column concentration in unseeded experiment (Figure 5.18a) which means we have displacement of cloud ice due to complex microphysical interactions and due to phase change influence on cloud dynamics.
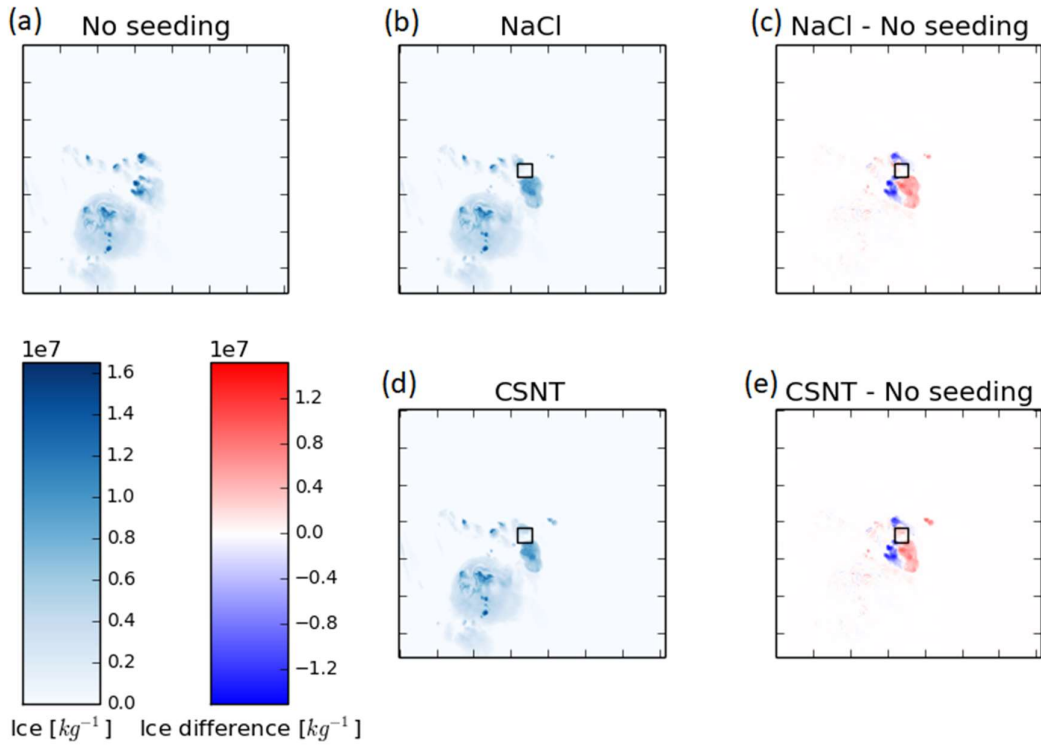
Figure 5.18 Column integrated cloud ice concentration for July 21, 2014 at 15 UTC for unseeded experiment (a), for NaCl seeded experiment (b), for CSNT seeded experiment (d), difference of accumulated precipitation for NaCl seeded experiment versus unseeded experiment (c) and for CSNT seeded experiment versus unseeded experiment (e). Black square represents seeding area.

CHAPTER 6

6 Conclusions

WRF–ARW scheme of the periodic collapse of the gust front head was proposed in this thesis. A number of theoretical and observational studies (e.g., Simpson, 1972; Charba, 1974; Goff, 1975; Mitchell and Hovermale, 1977; Ćurić, 1977; 1980; Curić and Janc, 1993; Ćurić et al., 2003; Geerts et al., 2006) showed the existence of this cyclic collapse of the head caused by the surface friction and the fact that cold air is heavier than the warm air. This interesting feature of the gust front was parameterized through the periodic forcing of the vertical velocity 8 km ahead of the precipitation zone underneath the cloud, and in the lowest eight WRF levels. The propagation velocity of the cloud was estimated as the mean wind speed and direction in the upper half of the troposphere. The implemented scheme was tested on an ideal case of the supercell cumulonimbus (Cb) cloud (Weisman and Klemp, 1982; 1984; 1986) as well as against the observations of intense cumuliform clouds above the United Arab Emirates on 17 July 2009.

The parameterization of the gust front in the idealized case resulted in more precipitation and different lifecycle of the parent cloud. Firstly, the growth of new cumuliform cells ahead of the parent Cb cloud due to the periodic forcing of vertical velocity was observed in the parameterized case. The newly formed cells tend to merge with the parent cloud over the time. Secondly, the parameterization of the gust front results in more precipitation on the surface. After careful examination of the precipitation distribution, it was concluded that the increase of precipitation was in the areas characterized with light precipitation. Interestingly, the under-prediction of light precipitation was one of the main drawbacks of the microphysics scheme with the explicit treatment of aerosols, reported in the recent studies by Lompar et al. (2017), Thompson and Eidhammer (2014), Sorooshian et al. (2010) and Qian et al. (2009). Thirdly,

the inclusion of the developed scheme altered the mixing ratios of cloud water and rain, and snow to some extent in the later stages of cloud development. The mixing ratios of ice and graupel, however, were the same between the two runs. Similarly, the concentration of rain droplets increases in the parameterized case, whereas the concentration of ice particles stayed unchanged. Fourthly, the overall could dynamics of the idealized Cb cloud was preserved (e.g., the locations of updraft and downdrafts), but the intensities of both the updraft and downdrafts increased.

In the real case, the WRF simulation with the gust front parameterization scheme produced more convective clouds than the WRF run without the gust front scheme. Both simulations, however, gave less convection that the amount observed in satellite images. The scheme was accurately deployed only on cumuliform clouds and the stratiform convection was not influenced by the included scheme.

The differences between an explicit and implicit treatment of aerosols in WRF-ARW model were also investigated. The two considered microphysical schemes are (Thompson and Eidhammer, 2014; TE14) for the explicit modelling (WRF-AE) and (Thompson et al., 2008; T08) for the implicit inclusion (WRF-AI) of aerosols. The analyzed case study is a severe mesoscale convective system with supercells that occurred in the afternoon of July 21, 2014 in central and western Serbia. The differences between the modelled results are further compared against the satellite imaging, Doppler radar measurements and surface observations. The following conclusions are drawn.

- WRF-AE accurately predicted the position and momentum of the NIFA cloud of dust particles that were transported on July 21 from the north Africa to the Balkans. The frontal system including the associated deep clouds ahead of the cold front located in the Mediterranean are captured by both models.

- Convective clouds in the WRF-AE case are wider and more spread out (also more merged) than in the WRF-AI case where individuality of convective cells is evident. This difference is particularly noticeable in the initial stage of cloud development.

- Both models under-predicted the composite radar reflectivity and displaced the clouds downwind from their satellite- and radar-inferred locations. This inaccuracy is probably due to the crude representation of orography in WRF model.

- Both models over-predicted surface precipitation, but in two different manners. Namely, WRF-AE under-predicted very light precipitation and greatly over-predicted the light to moderate precipitations (Figures 3.23 and 3.29). WRF-AI, on the other hand, over-predicted the heavy precipitation and also produced larger outliers (Figure 3.24). The WRF-AI forecasts of light precipitation are in good accordance with measurements.

- WRF-AE results demonstrated the necessity of simultaneous presence of aerosols and strong convection for developments of deep clouds with heavy precipitation and hail (Figure 3.26).

- Flux of NIFA into the supercell from southwest and west is evident in the WRF-AE simulation (Figure 3.28a). Such numerical products, which are not obtainable through the traditional implicate treatment of aerosols, could of particular interest in weather modification and hail suppression.

A few advantages of explicit modelling of aerosols in numerical weather prediction models were shown. However, results also show that this method, although being more physically realistic, does not necessarily provide more accurate results in all instances. All numerical simulations are susceptible to shortcoming and contain uncertainties. When it comes to microphysics, one of the main sources of uncertainties in our simulation is most likely the initial field

of aerosols obtained from the global model. The initial concentrations are retrieved from the 7-year runs of the GOCART model. Instead, a more appropriate solution might be to use meteorological analyses with assimilated aerosols. Such products have become available in the last 8 or so years from the European Center for Medium-Range four-dimensional assimilations (Benedetti et al., 2009) as part of the Global and regional Earth-system Monitoring using Satellite and in-situ data project. It should be noted, however, that the cloud of NIFA and their advection from the north Africa to the Balkans are accurately captured relying only on the initial concentrations from the climatological means (Figure 3.20). Yet another, and most simplistic, option for the initial concentrations of aerosols is to assume the same exponential profile of NIFA and NWFA in all model points. Such an experiment were conduced and the results (not shown) were substantially more inaccurate. Namely, the NIFA concentrations in the Balkans were greatly over-predicted and the discrepancies in the modelled precipitations were massive. For instance, high concentrations of NIFA particles were found even above the Alps. These errors were due to the high initial concentration of aerosols and inability of the model to disperse and transport them effectively throughout the domain.

The next uncertainty of this approach is associated with the parameterization of different microphysical processes and their connection with aerosols. The TE14 scheme is based on the TE08 bulk microphysics with five water species. An upgrade on the existing scheme would be to classify aerosol types and chemical composition in multiple categories based on their physical and chemical (i.e. activation) properties. In this approach, for example, the hygroscopicity parameter would be varied for different aerosols species (Petters and Kreidenweis, 2007) instead of the fixed value (0.4) used in TE14 and our study. This improvement, however, comes with an increase of computational time. Currently, the explicit approach slightly increases the computational expense (for about 15%), which is mainly due to the additional advection of aerosols in model dynamics. Next, the TE14 scheme should be modified to accounting for

entrainment of subsaturated air into the rising parcel (Feingold and Heymsfield, 1992). This addition to the scheme would decrease the liquid water content in clouds (Heymsfield et al., 1991) and therefore correct, at least to some extent, the observed over-predictions of WRF-AE surface precipitation. Lastly, the explicate inclusion of aerosols in numerical weather prediction models is a relatively new method which requires more research; in particular the specific case studies such as the one in this thesis, as well as more idealized cases with controlled environments such as the one investigated in TE14. Microphysical characteristics of clouds, aerosol concentrations and their physical and chemical properties differ from region to region. For these reasons, case studies should focus at different parts of world and an additional emphasis should be placed on the zones characterized with light precipitation.

This thesis introduces a new One-Dimensional (1D) Model for Cloud Seeding Experiments (1D MCSE) and tests its performances through the investigation of a novel seeding material proposed for the precipitation enhancement applications. The proposed model contains the dynamics core of the 1D model by Ćurić and Janc (1990) and Curić and Janc (1993a), while the microphysics processes are modelled using the microphysics scheme with explicit treatment of aerosols, developed by Thompson and Eidhammer (2014). This microphysics package is one of the options for microphysics scheme in the WRF model. The 1D MCSE model can simulate droplet growth on the natural population of aerosols and on different seeding materials. Moreover, the model is very flexible and can be used to investigate droplet activation and their sensitivity to external factors, such as relative humidity, updraft velocity, and temperature. The internal factors such as chemical and geometric characteristics of aerosols can also be varied. Moreover, the model simulates the quintessential processes in precipitation formation such as the beginning of coalescence and the production of rain through the processes of autoconversion of cloud droplets, gravitational collection, rain self-collection, drop break-up, and evaporation. The proposed model accounts for multicomponent and multimodal population of aerosols that is particularly important when investigating different scenarios of precipitation modification. In addition, the model is computationally

efficient, flexible, and easily extendable to three-dimensional cloud model and real atmospheric conditions.

The novel aerosol investigated in this thesis—the shell structured $TiO_2/NaCl$—has recently been developed by Tai et al. (2017) and it showed the superior performances over the pure NaCl in the laboratory conditions. In this thesis, the characteristics of this aerosol are numerically investigated using the 1D MCSE model. Two numerical approaches are utilized in the analysis of the characteristics of the shell structured $TiO_2/NaCl$. Firstly, the activation characteristics of this artificial aerosol are investigated using the parcel model in order to create the lookup tables for this seeding material (similar to the existing lookup tables for different seeding reagents). Secondly, the activation characteristics of the shell structured $TiO_2/NaCl$ are investigated by injecting the aerosol underneath the cloud and allowing it to grow in the updraft. That is, the activation characteristics and growth of the seeding material are explicitly modelled. The following conclusions are drawn:

- Similar to the laboratory experiments by Tai et al. (2017), the numerical experiments in this thesis demonstrated profoundly better hygroscopic characteristics of the shell structured $TiO_2/NaCl$ over the pure NaCl.

- The kappa parameter (κ) of the shell structured $TiO_2/NaCl$ is around 20 which is approximately twenty times larger than for the pure NaCl.

- A variety of different numerical experiments showed the substantial increase in the accumulated surface precipitation when the shell structured $TiO_2/NaCl$ is used instead of pure NaCl. For instance, if both seeding materials are injected for 4.5 min into the updraft at a height of 200 m above ground, the observed increase in the surface precipitation is 4% and 10% for NaCl and the shell structured $TiO_2/NaCl$, respectively. However, when the particles are released at the same height (200 m), but the time window is increased to 7.5 min, the novel aerosols enhances precipitation for over 15% when compared to the increase obtained from injecting the pure NaCl and approximately 30% more than in natural case.

- The supremacy of the novel aerosol grows with increasing the time window of seeding, but it tends to decreases with increasing the seeding height above ground.

The most important thing this thesis has made available is the 3D numerical model for cloud seeding experiments which is based on WRF-ARW model, 1D MCSE model and laboratory results. This switch from 1D MCSE to 3D MCSE model enabled detailed analysis of cloud seeding process in realistic conditions and enabled spatiotemporal analysis of precipitations. 3D MCSE model was tested on an ideal case of the supercell cumulonimbus (Cb) cloud (Weisman and Klemp, 1982; 1984; 1986) and on MCS occurred on the afternoon of July 21, 2014 in the Western Balkans. The most severe conditions were observed around Čačak and Gornji Milanovac areas in Serbia (Figure 3.17c,d) and that area was chosen to be seeded with NaCl and CSNT material. Main conclusions are:

- Similar to the laboratory experiments by Tai et al. (2017) and numerical experiments with 1D MCSE, numerical experiments in 3D MCSE model demonstrated profoundly better hygroscopic characteristics of the shell structured $TiO_2/NaCl$ over the pure NaCl. For instance, if both seeding materials are injected for 10 min into the updraft in layer from 800 to 1000 m height above ground, the observed increase in the surface precipitation is 5% and 19% for NaCl and the shell structured $TiO_2/NaCl$, respectively.
- Precipitation footprint in the case of NaCl seeding and CSNT seeding is larger than in unseeded experiment. Precipitation increase due to seeding is not evenly distributed. The greatest increase is within light precipitations area but increase in all categories is noticeable.
- Even NaCl and CSNT serves as CCN aerosols changes in cloud ice concentration due to seeding is observed. Cloud ice displacement is the main type of change.

This thesis investigated numerical modelling of warm and cold type rain modification process from a new perspective. All results presented in this thesis

are a unique contribution to the understanding of weather modification modelling process. All of the open questions stated in the research proposal have been addressed and results presented. Applicability of the new tools developed in this thesis for research and development of new seeding materials was shown. Finally this research offers inexhaustible and ecologically acceptable solution to provision of drinking water.

The results presented in this thesis are published in the leading peer-reviewed meteorological journal – Atmospheric Research.

References

Abulikemu, A., Xu, X., Wang, Y., Ding, J., Zhang, S., Shen, W., 2016. A modeling study of convection initiation prior to the merger of a sea-breeze front and a gust front. Atmospheric Res. 182, 10–19. doi:10.1016/j.atmosres.2016.07.003

Ackerman, A.S., Toon, O.B., Stevens, D.E., Coakley, J.A., 2003. Enhancement of cloud cover and suppression of nocturnal drizzle in stratocumulus polluted by haze. Geophys. Res. Lett. 30, 1381. doi:10.1029/2002GL016634

Alonso, M., Alguacil, F.J., 2006. Thin coating on ultrafine aerosol particles. Atmospheric Res., 16th International Conference on Nucleation and Atmospheric Aerosols 82, 605–609. https://doi.org/10.1016/j.atmosres.2006.02.016.

Atkins, N.T., Wakimoto, R.M., 1991. Wet microburst activity over the southeastern United States: Implications for forecasting. Weather Forecast. 6, 470–482. doi:10.1175/1520-0434(1991)006<0470:WMAOTS>2.0.CO;2

Ball, F.K., 1960. A theory of fronts in relation to surface stress. Q. J. R. Meteorol. Soc. 86, 51–66. doi:10.1002/qj.49708636704

Benedetti, A., Morcrette, J.-J., Boucher, O., Dethof, A., Engelen, R.J., Fisher, M., Flentje, H., Huneeus, N., Jones, L., Kaiser, J.W., Kinne, S., Mangold, A., Razinger, M., Simmons, A.J., Suttie, M., 2009. Aerosol analysis and forecast in the European Centre for Medium-Range Weather Forecasts Integrated Forecast System: 2. Data assimilation. J. Geophys. Res. Atmospheres 114, D13205. doi:10.1029/2008JD011115

Blunden, J., Arndt, D.S., 2016. State of the climate in 2015. Bull. Am. Meteorol. Soc. 97, Si-S275. https://doi.org/10.1175/2016BAMSStateoftheClimate.1.

Bringi, V.N., Williams, C.R., Thurai, M., May, P.T., 2009. Using Dual-Polarized Radar and Dual-Frequency Profiler for DSD Characterization: A Case Study from Darwin, Australia. J. Atmospheric Ocean. Technol. 26, 2107–2122. doi:10.1175/2009JTECHA1258.1

Britter, R.E., Simpson, J.E., 1978. Experiments on the dynamics of a gravity current head. J. Fluid Mech. 88, 223–240. doi:10.1017/S0022112078002074

Brooks, H.E., Lee, J.W., Craven, J.P., 2003. The spatial distribution of severe thunderstorm and tornado environments from global reanalysis data. Atmospheric Res., European Conference on Severe Storms 2002 67–68, 73–94. doi:10.1016/S0169-8095(03)00045-0

Bruintjes, R.T., 1999. A review of cloud seeding experiments to enhance precipitation and some new prospects. Bull. Am. Meteorol. Soc. 80, 805–820. https://doi.org/10.1175/1520-0477(1999)080<0805:AROCSE>2.0.CO;2.

Bunkers, M.J., Klimowski, B.A., Zeitler, J.W., Thompson, R.L., Weisman, M.L., 2000. Predicting supercell motion using a new hodograph technique. Weather Forecast. 15, 61–79. doi:10.1175/1520-0434(2000)015<0061:PSMUAN>2.0.CO;2

Burlando, M., Romanić, D., Solari, G., Hangan, H., Zhang, S., 2017. Field data analysis and weather scenario of a downburst event in Livorno, Italy, on 1 October 2012. Mon. Weather Rev. 145, 3507–3527. doi:10.1175/MWR-D-17-0018.1

Charba, J., 1974. Application of gravity current model to analysis of squall-line gust front. Mon. Weather Rev. 102, 140–156. doi:10.1175/1520-0493(1974)102<0140:AOGCMT>2.0.CO;2

Chay, M.T., Albermani, F., Wilson, R., 2006. Numerical and analytical simulation of downburst wind loads. Eng. Struct. 28, 240–254. doi:10.1016/j.engstruct.2005.07.007

Cintineo, R., Otkin, J.A., Xue, M., Kong, F., 2013. Evaluating the Performance of Planetary Boundary Layer and Cloud Microphysical Parameterization Schemes in Convection-Permitting Ensemble Forecasts Using Synthetic GOES-13 Satellite Observations. Mon. Weather Rev. 142, 163–182. doi:10.1175/MWR-D-13-00143.1

Clyne, J., Mininni, P., Norton, A., Rast, M., 2007. Interactive desktop analysis of high resolution simulations: application to turbulent plume dynamics and current sheet formation. New J. Phys. 9, 301. doi:10.1088/1367-2630/9/8/301

Cohuet, J.B., Romero, R., Homar, V., Ducrocq, V., Ramis, C., 2011. Initiation of a severe thunderstorm over the Mediterranean Sea. Atmospheric Res., 5th European Conference on Severe Storms 100, 603–620. doi:10.1016/j.atmosres.2010.11.002

Colarco, P., da Silva, A., Chin, M., Diehl, T., 2010. Online simulations of global aerosol distributions in the NASA GEOS-4 model and comparisons to satellite and ground-based aerosol optical depth. J. Geophys. Res. Atmospheres 115, D14207. doi:10.1029/2009JD012820

Cooper, W.A., Bruintjes, R.T., Mather, G.K., 1997. Calculations pertaining to hygroscopic seeding with flares. J. Appl. Meteorol. 36, 1449–1469. https://doi.org/10.1175/1520-0450(1997)036<1449:CPTHSW>2.0.CO;2.

Cotton, W.R., Bryan, G., Heever, S.C. van den, 2010. Storm and Cloud Dynamics, 2nd ed. Academic Press, Amsterdam.

Csirmaz, K., Simon, A., Pistotnik, G., Polyánszky, Z., Neštiak, M., Nagykovácsi, Z., Sokol, A., 2013. A study of rotation in thunderstorms in a weakly- or moderately-sheared environment. Atmospheric Res., 6th European Conference on Severe Storms 2011. Palma de Mallorca, Spain 123, 93–116. doi:10.1016/j.atmosres.2012.09.017

Ćurić, M., 1980. Dynamics of a cold air outflow from the base of the thunderstorm. A simple model. J. Rech. Atmos. 14, 493–498.

Ćurić, M., 1977. A model for the calculation of the appearance of frontal profiles and of the vertical velocity of air at a front. Arch. Für Meteorol. Geophys. Bioklimatol. Ser. A 26, 13–19. doi:10.1007/BF02246531

Ćurić, M., 2001. Mikrofizika oblaka. Republički hidrometeorološki zavod Srbije

Ćurić, M., 2001. Modifikacija vremena. Republički hidrometeorološki zavod Srbije

Ćurić, M., Janc, D., 1987. On the influence of entrainment and forced lifting on some products of a 1-D model of a Cb cloud. Atmospheric Res. 21, 151–169. doi:10.1016/0169-8095(87)90005-6

Ćurić, M., Janc, D., 1990. Numerical study of the cloud seeding effects. Meteorol. Atmospheric Phys. 42, 145–164. https://doi.org/10.1007/BF01041762.

Curić, M., Janc, D., 1993a. Predictive capabilities of a one-dimensional convective cloud model with forced lifting and a new entrainment formulation. J. Appl. Meteorol. 32, 1733–1740. https://doi.org/10.1175/1520-0450(1993)032<1733:PCOAOD>2.0.CO;2.

Ćurić, M., Janc, D., 1993b. Dependence of the simulated seeding effects of Cb cloud on the types of the AgI agents. Meteorol. Atmospheric Phys. 52, 91–100. https://doi.org/10.1007/BF01025755.

Ćurić, M., Janc, D., Vujović, D., Vučković, V., 2003. The effects of a river valley on an isolated cumulonimbus cloud development. Atmospheric Res. 66, 123–139. doi:10.1016/S0169-8095(02)00144-8

Ćurić, M., Janc, D., Vučković, V., 2007. Numerical simulation of Cb cloud vorticity. Atmospheric Res., European Conference on Severe Storms 2004ECSS 2004European Conference on Severe Storms 2004 83, 427–434. doi:10.1016/j.atmosres.2005.10.024

Ćurić, M., Janc, D., 2010. Comparison of Modeled and Observed Accumulated Convective Precipitation in Mountainous and Flat Land Areas. J. Hydrometeorol. 12, 245–261. doi:10.1175/2010JHM1259.1

DeFelice, T.P., Axisa, D., 2017. Modern and prospective technologies for weather modification activities: Developing a framework for integrating autonomous unmanned aircraft systems. Atmos. Res. 193, 173–183. https://doi.org/10.1016/j.atmosres.2017.04.024.

De Gaetano, P., Repetto, M.P., Repetto, T., Solari, G., 2014. Separation and classification of extreme wind events from anemometric records. J. Wind Eng. Ind. Aerodyn. 126, 132–143. doi:10.1016/j.jweia.2014.01.006

Del Genio, A.D., Wu, J., Chen, Y., 2012. Characteristics of mesoscale organization in WRF simulations of convection during TWP-ICE. J. Clim. 25, 5666–5688. doi:10.1175/JCLI-D-11-00422.1

Dessens, J., Sánchez, J.L., Berthet, C., Hermida, L., Merino, A., 2016. Hail prevention by ground-based silver iodide generators: Results of historical and modern field projects. Atmos. Res. 170, 98–111. https://doi.org/10.1016/j.atmosres.2015.11.008.

Droegemeier, K.K., Wilhelmson, R.B., 1987. Numerical simulation of thunderstorm outflow dynamics. Part I: Outflow sensitivity experiments and turbulence dynamics. J. Atmospheric Sci. 44, 1180–1210. doi:10.1175/1520-0469(1987)044<1180:NSOTOD>2.0.CO;2

Drofa, A.S., Eran'kov, V.G., Ivanov, V.N., Shilin, A.G., Iskevich, G.F., 2013. Experimental investigations of the effect of cloud-medium modification by salt powders. Izv. Atmospheric Ocean. Phys. 49, 298–306. https://doi.org/10.1134/S0001433813030043.

Drofa, A.S., Ivanov, V.N., Rosenfeld, D., Shilin, A.G., 2010. Studying an effect of salt powder seeding used for precipitation enhancement from convective clouds. Atmos. Chem. Phys. 10, 8011–8023. https://doi.org/10.5194/acp-10-8011-2010.

Dudhia, J., 1989. Numerical study of convection observed during the winter monsoon experiment using a mesoscale two-dimensional model. J. Atmospheric Sci. 46, 3077–3107. doi:10.1175/1520-0469(1989)046<3077:NSOCOD>2.0.CO;2

Duffourg, F., Nuissier, O., Ducrocq, V., Flamant, C., Chazette, P., Delanoë, J., Doerenbecher, A., Fourrié, N., Di Girolamo, P., Lac, C., Legain, D., Martinet, M., Saïd, F., Bock, O., 2016. Offshore deep convection initiation and maintenance during the HyMeX IOP 16a heavy precipitation event. Q. J. R. Meteorol. Soc. n/a-n/a. doi:10.1002/qj.2725

Efstathiou, G.A., Melas, D., Zoumakis, N., Kassomenos, P.A., 2013a. Evaluation of WRF-ARW Model in Reproducing a Heavy Rainfall Event Over Chalkidiki, Greece: The Effect of Land-Surface Features on Rainfall, in: Helmis, C.G.,

Nastos, P.T. (Eds.), Advances in Meteorology, Climatology and Atmospheric Physics, Springer Atmospheric Sciences. Springer Berlin Heidelberg, pp. 65–71. doi:10.1007/978-3-642-29172-2_10

Efstathiou, G.A., Zoumakis, N.M., Melas, D., Lolis, C.J., Kassomenos, P., 2013b. Sensitivity of WRF to boundary layer parameterizations in simulating a heavy rainfall event using different microphysical schemes. Effect on large-scale processes. Atmospheric Res. 132–133, 125–143. doi:10.1016/j.atmosres.2013.05.004

Eidhammer, T., DeMott, P.J., Kreidenweis, S.M., 2009. A comparison of heterogeneous ice nucleation parameterizations using a parcel model framework. J. Geophys. Res. Atmospheres 114, D06202. doi:10.1029/2008JD011095

Ek, M.B., Mitchell, K.E., Lin, Y., Rogers, E., Grunmann, P., Koren, V., Gayno, G., Tarpley, J.D., 2003. Implementation of Noah land surface model advances in the National Centers for Environmental Prediction operational mesoscale Eta model. J. Geophys. Res. Atmospheres 108, 8851. doi:10.1029/2002JD003296

Feingold, G., Heymsfield, A.J., 1992. Parameterizations of Condensational Growth of Droplets for Use in General Circulation Models. J. Atmospheric Sci. 49, 2325–2342. doi:10.1175/1520-0469(1992)049<2325:POCGOD>2.0.CO;2

French, J.R., Friedrich, K., Tessendorf, S.A., Rauber, R.M., Geerts, B., Rasmussen, R.M., Xue, L., Kunkel, M.L., Blestrud, D.R., 2018. Precipitation formation from orographic cloud seeding. Proc. Natl. Acad. Sci. 201716995. https://doi.org/10.1073/pnas.1716995115.

Fujita, T.T., 1985. The downburst: microburst and macroburst. Satellite and Mesometeorology Research Project, Dept. of the Geophysical Sciences, University of Chicago, Chicago, IL, United States.

Fujita, T.T., 1981. Tornadoes and downbursts in the context of generalized planetary scales. J. Atmospheric Sci. 38, 1511–1534. doi:10.1175/1520-0469(1981)038<1511:TADITC>2.0.CO;2

Fujita, T.T., 1976. Spearhead echo and downburst near the approach end of a John F. Kennedy Airport runway, New York City (Technical Report No. NASA-CR-146561). Chicago University; Deptment of Geophysical Sciences, Chicago, IL, United States.

Gascón, E., Merino, A., Sánchez, J.L., Fernández-González, S., García-Ortega, E., López, L., Hermida, L., 2015. Spatial distribution of thermodynamic conditions of severe storms in southwestern Europe. Atmospheric Res. 164–165, 194–209. doi:10.1016/j.atmosres.2015.05.012

Geerts, B., Damiani, R., Haimov, S., 2006. Finescale vertical structure of a cold front as revealed by an airborne Doppler radar. Mon. Weather Rev. 134, 251–271. doi:10.1175/MWR3056.1

Ginoux, P., Chin, M., Tegen, I., Prospero, J.M., Holben, B., Dubovik, O., Lin, S.-J., 2001. Sources and distributions of dust aerosols simulated with the GOCART model. J. Geophys. Res. Atmospheres 106, 20255–20273. doi:10.1029/2000JD000053

Goff, R.C., 1976. Vertical structure of thunderstorm outflows. Mon. Weather Rev. 104, 1429–1440. doi:10.1175/1520-0493(1976)104<1429:VSOTO>2.0.CO;2

Goff, R.C., 1975. Thunderstorm-outflow kinematics and dynamics, NOAA Tech. Memo. NOAA-ERL-NSSL.

Gunter, W.S., Schroeder, J.L., 2015. High-resolution full-scale measurements of thunderstorm outflow winds. J. Wind Eng. Ind. Aerodyn. 138, 13–26. doi:10.1016/j.jweia.2014.12.005

Heymsfield, A.J., Miloshevich, L.M., Slingo, A., Sassen, K., Starr, D.O., 1991. An Observational and Theoretical Study of Highly Supercooled Altocumulus. J. Atmospheric Sci. 48, 923–945. doi:10.1175/1520-0469(1991)048<0923:AOATSO>2.0.CO;2

Hjelmfelt, M.R., 1988. Structure and life cycle of microburst outflows observed in Colorado. J. Appl. Meteorol. 27, 900–927. doi:10.1175/1520-0450(1988)027<0900:SALCOM>2.0.CO;2

Holmes, J.D., Hangan, H.M., Schroeder, J.L., Letchford, C.W., Orwig, K.D., 2008. A forensic study of the Lubbock-Reese downdraft of 2002. Wind Struct. 11, 137–152. doi:10.12989/was.2008.11.2.137

Hobbs, P.V., Chang, S., Locatelli, J.D., 1974. The dimensions and aggregation of ice crystals in natural clouds. J. Geophys. Res. 79, 2199–2206. doi:10.1029/JC079i015p02199

Hoose, C., Kristjánsson, J.E., Burrows, S.M., 2010. How important is biological ice nucleation in clouds on a global scale? Environ. Res. Lett. 5, 024009. doi:10.1088/1748-9326/5/2/024009

Holmes, J.D., Oliver, S.E., 2000. An empirical model of a downburst. Eng. Struct. 22, 1167–1172. doi:10.1016/S0141-0296(99)00058-9

Hong, S.-Y., Noh, Y., Dudhia, J., 2006. A new vertical dffusion package with an explicit treatment of entrainment processes. Mon. Weather Rev. 134, 2318–2341. doi:10.1175/MWR3199.1

Huggins, A.W., Rodi, A.R., 1985. Physical response of convective clouds over the Sierra Nevada to seeding with dry ice. J. Clim. Appl. Meteorol. 24, 1082–1098. https://doi.org/10.1175/1520-0450(1985)024<1082:PROCCO>2.0.CO;2.

Irwin, M., Good, N., Crosier, J., Choularton, T.W., McFiggans, G., 2010. Reconciliation of measurements of hygroscopic growth and critical supersaturation of aerosol particles in central Germany. Atmos. Chem. Phys. 10, 11737–11752. https://doi.org/10.5194/acp-10-11737-2010.

Järvi, L., Punkka, A.-J., Schultz, D.M., Petäjä, T., Hohti, H., Rinne, J., Pohja, T., Kulmala, M., Hari, P., Vesala, T., 2007. Micrometeorological observations of a microburst in southern Finland. Bound.-Layer Meteorol. 125, 343–359. doi:10.1007/s10546-007-9204-7

Jiménez, P.A., Dudhia, J., 2011. Improving the Representation of Resolved and Unresolved Topographic Effects on Surface Wind in the WRF Model. J. Appl. Meteorol. Climatol. 51, 300–316. doi:10.1175/JAMC-D-11-084.1

Junge, C., 1955. The size distribution and aging of natural aerosols as determined from electrical and optical data on the atmosphere. J. Meteorol. 12, 13–25. https://doi.org/10.1175/1520-0469(1955)012<0013:TSDAAO>2.0.CO;2.

Kain, J.S., 2004. The Kain–Fritsch Convective Parameterization: An Update. J. Appl. Meteorol. 43, 170–181. doi:10.1175/1520-0450(2004)043<0170:TKCPAU>2.0.CO;2

Kalina, E.A., Friedrich, K., Morrison, H., Bryan, G.H., 2014. Aerosol effects on idealized supercell thunderstorms in different environments. J. Atmospheric Sci. 71, 4558–4580. doi:10.1175/JAS-D-14-0037.1

Khain, A.P., Beheng, K.D., Heymsfield, A., Korolev, A., Krichak, S.O., Levin, Z., Pinsky, M., Phillips, V., Prabhakaran, T., Teller, A., van den Heever, S.C., Yano, J.-I., 2015. Representation of microphysical processes in cloud-resolving models: Spectral (bin) microphysics versus bulk parameterization. Rev. Geophys. 53, 2014RG000468. https://doi.org/10.1002/2014RG000468.

Khain, A., Ovtchinnikov, M., Pinsky, M., Pokrovsky, A., Krugliak, H., 2000. Notes on the state-of-the-art numerical modeling of cloud microphysics. Atmos. Res. 55, 159–224. https://doi.org/10.1016/S0169-8095(00)00064-8.

Kovačević, N., Ćurić, M., 2015. Influence of drop size distribution function on simulated ground precipitation for different cloud droplet number concentrations. Atmospheric Res. 158–159, 36–49. doi:10.1016/j.atmosres.2015.02.004

Kovačević, N., Ćurić, M., 2013. The impact of the hailstone embryos on simulated surface precipitation. Atmospheric Res. 132–133, 154–163. doi:10.1016/j.atmosres.2013.05.013

Kristensen, T.B., Prisle, N.L., Bilde, M., 2014. Cloud droplet activation of mixed model HULIS and NaCl particles: Experimental results and κ-Köhler theory. Atmos. Res. 137, 167–175. https://doi.org/10.1016/j.atmosres.2013.09.017.

Lazaridis, M., Hov, Ø., Eleftheriadis, K., 2000. Heterogeneous nucleation on rough surfaces: implications to atmospheric aerosols. Atmos. Res. 55, 103–113. https://doi.org/10.1016/S0169-8095(00)00059-4.

Lazaridis, M., Kulmala, M., Gorbunov, B.Z., 1992. Binary heterogeneous nucleation at a non-uniform surface. J. Aerosol Sci. 23, 457–466. https://doi.org/10.1016/0021-8502(92)90017-P.

Letchford, C.W., Chay, M.T., 2002. Pressure distributions on a cube in a simulated thunderstorm downburst. Part B: moving downburst observations. J. Wind Eng. Ind. Aerodyn. 90, 733–753. doi:10.1016/S0167-6105(02)00163-0

Levin, Z., Cotton, W.R. (Eds.), 2009. Aerosol Pollution Impact on Precipitation: A Scientific Review. Springer Netherlands, Dordrecht.

Lim, K.-S.S., Hong, S.-Y., 2009. Development of an Effective Double-Moment Cloud Microphysics Scheme with Prognostic Cloud Condensation Nuclei (CCN) for Weather and Climate Models. Mon. Weather Rev. 138, 1587–1612. doi:10.1175/2009MWR2968.1

Lin, F.Y.H., Li, D., Neumann, A.W., 1993. Effect of surface roughness on the dependence of contact angles on drop size. J. Colloid Interface Sci. 159, 86–95. https://doi.org/10.1006/jcis.1993.1300.

Lompar, M., Ćurić, M., Romanic, D., 2017. Simulation of a severe convective storm using a numerical model with explicitly incorporated aerosols. Atmospheric Res. 194, 164–177. doi:10.1016/j.atmosres.2017.04.037

Lompar, M., Ćurić, M., Romanic, D., 2018. Implementation of a gust front head collapse scheme in the WRF numerical model. Atmos. Res. 203, 231–245. https://doi.org/10.1016/j.atmosres.2017.12.018.

Maddox, R.A., 1976. An evaluation of tornado proximity wind and stability data. Mon. Weather Rev. 104, 133–142. doi:10.1175/1520-0493(1976)104<0133:AEOTPW>2.0.CO;2

Maddox, R.A., 1980. Meoscale Convective Complexes. Bull. Am. Meteorol. Soc. 61, 1374–1387. doi:10.1175/1520-0477(1980)061<1374:MCC>2.0.CO;2

Mahoney, W.P., 1988. Gust front characteristics and the kinematics associated with interacting thunderstorm outflows. Mon. Weather Rev. 116, 1474–1492. doi:10.1175/1520-0493(1988)116<1474:GFCATK>2.0.CO;2

Mahović, N.S., Horvath, A., Csirmaz, K., 2007. Numerical simulation of severe convective phenomena over Croatian and Hungarian territory. Atmospheric Res., European Conference on Severe Storms 2004ECSS 2004European Conference on Severe Storms 2004 83, 121–131. doi:10.1016/j.atmosres.2005.09.011

Mather, G.K., Terblanche, D.E., Steffens, F.E., Fletcher, L., 1997. Results of the South African cloud-eeeding experiments using hygroscopic flares. J. Appl. Meteorol. 36, 1433–1447. https://doi.org/10.1175/1520-0450(1997)036<1433:ROTSAC>2.0.CO;2.

McConville, A.C., Sterling, M., Baker, C.J., 2009. The physical simulation of thunderstorm downbursts using an impinging jet. Wind Struct. 12, 133–149. doi:10.12989/was.2009.12.2.133

Mertes, S., Schwarzenböck, A., Laj, P., Wobrock, W., Pichon, J.-M., Orsi, G., Heintzenberg, J., 2001. Changes of cloud microphysical properties during the transition from supercooled to mixed-phase conditions during CIME. Atmos. Res. 58, 267–294. https://doi.org/10.1016/S0169-8095(01)00095-3.

Milton, S.F., Wilson, C.A., 1996. The Impact of Parameterized Subgrid-Scale Orographic Forcing on Systematic Errors in a Global NWP Model. Mon. Weather Rev. 124, 2023–2045. doi:10.1175/1520-0493(1996)124<2023:TIOPSS>2.0.CO;2

Mitchell, K.E., Hovermale, J.B., 1977. A numerical investigation of the severe thunderstorm gust front. Mon. Weather Rev. 105, 657–675. doi:10.1175/1520-0493(1977)105<0657:ANIOTS>2.0.CO;2

Mlawer, E.J., Taubman, S.J., Brown, P.D., Iacono, M.J., Clough, S.A., 1997. Radiative transfer for inhomogeneous atmospheres: RRTM, a validated correlated-k model for the longwave. J. Geophys. Res. Atmospheres 102, 16663–16682. doi:10.1029/97JD00237

Morel, C., Senesi, S., 2002. A climatology of mesoscale convective systems over Europe using satellite infrared imagery. I: Methodology. Q. J. R. Meteorol. Soc. 128, 1953–1971. doi:10.1256/003590002320603485

Morrison, H., Milbrandt, J.A., 2010. Comparison of two-moment bulk microphysics schemes in idealized supercell thunderstorm simulations. Mon. Weather Rev. 139, 1103–1130. doi:10.1175/2010MWR3433.1

Mueller, C.K., Carbone, R.E., 1987. Dynamics of a thunderstorm outflow. J. Atmospheric Sci. 44, 1879–1898. doi:10.1175/1520-0469(1987)044<1879:DOATO>2.0.CO;2

Munich Re, 2016. Loss review for the first half of 2016: Storms and earthquakes drive losses up (Press release). Munich Re, München, Germany.

Murakami, M., 1990: Numerical modeling of dynamical and microphysical evolution of an isolated convective cloud-The 19 july 1981 CCOPE cloud. J. Meteor.
Soc. Japan, 68, 107-128

Murray, B.J., O'Sullivan, D., Atkinson, J.D., Webb, M.E., 2012. Ice nucleation by particles immersed in supercooled cloud droplets. Chem. Soc. Rev. 41, 6519–6554. doi:10.1039/C2CS35200A

Newton, C.W., Fankhauser, J.C., 1975. Movement and propagation of multicellular convective storms. Pure Appl. Geophys. 113, 747–764. doi:10.1007/BF01592957

Newton, C.W., Fankhauser, J.C., 1964. On the movements of convective storms, with emphasis on size discrimination in relation to water-budget requirements. J. Appl. Meteorol. 3, 651–668. doi:10.1175/1520-0450(1964)003<0651:OTMOCS>2.0.CO;2

Neukermans, A., Cooper, G., Foster, J., Gadian, A., Galbraith, L., Jain, S., Latham, J., Ormond, B., 2014. Sub-micrometer salt aerosol production intended for marine cloud brightening. Atmos. Res., The 16th International Conference on Clouds and Precipitation 142, 158–170. https://doi.org/10.1016/j.atmosres.2013.10.025.

Nugent, A.D., Watson, C.D., Thompson, G., Smith, R.B., 2016. Aerosol Impacts on Thermally Driven Orographic Convection. J. Atmospheric Sci. 73, 3115–3132. doi:10.1175/JAS-D-15-0320.1

Orville, H.D., 1996. A review of cloud modeling in weather modification. Bull. Am. Meteorol. Soc. 77, 1535–1555. https://doi.org/10.1175/1520-0477(1996)077<1535:AROCMI>2.0.CO;2.

Oseguera, R.M., Bowles, R.L., 1988. A simple, analytic 3-dimensional downburst model based on boundary layer stagnation flow, NASA technical memorandum. National Aeronautics and Space Administration, Langley Research Center, Hampton, Va.

Park, S.-U., Sikdar, D.N., 1982. The evolution of a sub-cloud layer structure associated with a severe storm—a case study. Tellus 34, 429–439. doi:10.1111/j.2153-3490.1982.tb01832.x

Peppler, R.A., 1988. A Review of Static Stability Indices and Related Thermodynamic Parameters (Technical Report No. MP-104), ISWS Miscellaneous Publication MP-104. Illinois State Water Survey, Illinois, United States.

Petters, M.D., Kreidenweis, S.M., 2007. A single parameter representation of hygroscopic growth and cloud condensation nucleus activity. Atmos Chem Phys 7, 1961–1971. doi:10.5194/acp-7-1961-2007

Pistotnik, G., Holzer, A.M., Kaltenböck, R., Tschannett, S., 2011. An F3 downburst in Austria—A case study with special focus on the importance of real-time site surveys. Atmospheric Res., 5th European Conference on Severe Storms 100, 565–579. doi:10.1016/j.atmosres.2010.10.011

Potter, M., Wiggert, D., Ramadan, B., 2016. Mechanics of Fluids. Thomson-Engineering.

Proctor, F.H., 1988. Numerical simulations of an isolated microburst. Part II: Sensitivity experiments. J. Atmospheric Sci. 46, 2143–2165. doi:10.1175/1520-0469(1989)046<2143:NSOAIM>2.0.CO;2

Pruppacher, H.., Klet, J.., 2010. Microphysics of Clouds and Precipitation, 2nd ed, Atmospheric and Oceanographic Sciences Library. Springer Netherlands.

Qian, Y., Gong, D., Fan, J., Leung, L.R., Bennartz, R., Chen, D., Wang, W., 2009. Heavy pollution suppresses light rain in China: Observations and modeling. J. Geophys. Res. Atmospheres 114, D00K02. doi:10.1029/2008JD011575

Rasmussen, E.N., Blanchard, D.O., 1998. A baseline climatology of sounding-derived supercell and tornado forecast parameters. Weather Forecast. 13, 1148–1164. doi:10.1175/1520-0434(1998)013<1148:ABCOSD>2.0.CO;2

Rasmussen, R., Baker, B., Kochendorfer, J., Meyers, T., Landolt, S., Fischer, A.P., Black, J., Thériault, J.M., Kucera, P., Gochis, D., Smith, C., Nitu, R., Hall, M., Ikeda, K., Gutmann, E., 2011. How Well Are We Measuring Snow: The NOAA/FAA/NCAR Winter Precipitation Test Bed. Bull. Am. Meteorol. Soc. 93, 811–829. doi:10.1175/BAMS-D-11-00052.1

Reuge, N., Fede, P., Berthoumieu, J.-F., Foucoin, F., Simonin, O., 2016. Modeling of the denebulization of warm fogs by hygroscopic seeding: Effect of various operating conditions and of the turbulence intensity. J. Appl. Meteorol. Climatol. 56, 249–261. https://doi.org/10.1175/JAMC-D-16-0151.1.

Reutter, P., Su, H., Trentmann, J., Simmel, M., Rose, D., Gunthe, S.S., Wernli, H., Andreae, M.O., Pöschl, U., 2009. Aerosol- and updraft-limited regimes of cloud droplet formation: influence of particle number, size and hygroscopicity on the activation of cloud condensation nuclei (CCN). Atmos. Chem. Phys. 9, 7067–7080. https://doi.org/10.5194/acp-9-7067-2009.

Rohe, D.M.M., Battersby, R.V., Wolf, H.U., 2014. Zinc Compounds. Ullmann's Encyclopedia of Industrial Chemistry, in: Ullmann's Encyclopedia of Industrial Chemistry. Wiley-VCH Verlag GmbH & Co. KGaA, pp. 1–8. https://doi.org/10.1002/14356007.a28_537.pub2.

Romanić, D., Ćurić, M., Lompar, M., Jovičić, I., 2016a. Contributing factors to Koshava wind characteristics. Int. J. Climatol. 36, 956–973. doi:10.1002/joc.4397

Romanić, D., Ćurić, M., Zarić, M., Lompar, M., Jovičić, I., 2016b. Investigation of an extreme Koshava wind episode of 30 January–4 February 2014. Atmospheric Sci. Lett. 17, 199–206. doi:10.1002/asl.643

Romero, R., Ramis, C., Homar, V., 2015. On the severe convective storm of 29 October 2013 in the Balearic Islands: observational and numerical study. Q. J. R. Meteorol. Soc. 141, 1208–1222. doi:10.1002/qj.2429

Rontu, L., 2006. A study on parametrization of orography-related momentum fluxes in a synoptic-scale NWP model. Tellus A 58, 69–81. doi:10.1111/j.1600-0870.2006.00162.x

Rosenfeld, D., 2006. Aerosols, Clouds, and Climate. Science 312, 1323–1324. doi:10.1126/science.1128972

Rosenfeld, D., Lohmann, U., Raga, G.B., O'Dowd, C.D., Kulmala, M., Fuzzi, S., Reissell, A., Andreae, M.O., 2008. Flood or Drought: How Do Aerosols Affect Precipitation? Science 321, 1309–1313. doi:10.1126/science.1160606

Rothenberg, D., Wang, C., 2015. Metamodeling of droplet activation for global climate models. J. Atmospheric Sci. 73, 1255–1272. https://doi.org/10.1175/JAS-D-15-0223.1.

Saleeby, S.M., Cotton, W.R., 2004. A large-droplet mode and prognostic number concentration of cloud droplets in the Colorado State University Regional Atmospheric Modeling System (RAMS). Part I: Module descriptions and supercell test simulations. J. Appl. Meteorol. 43, 182–195. https://doi.org/10.1175/1520-0450(2004)043<0182:ALMAPN>2.0.CO;2.

Sarkadi, N., Geresdi, I., Thompson, G., 2016. Numerical simulation of precipitation formation in the case orographically induced convective cloud: Comparison of the results of bin and bulk microphysical schemes. Atmos. Res. 180, 241–261. https://doi.org/10.1016/j.atmosres.2016.04.010.

Schaefer, V.J., 1946. The production of ice crystals in a cloud of supercooled water droplets. Science 104, 457–459. https://doi.org/10.1126/science.104.2707.457.

Segal, Y., Khain, A., Pinsky, M., Rosenfeld, D., 2004. Effects of hygroscopic seeding on raindrop formation as seen from simulations using a 2000-bin spectral cloud parcel model. Atmos. Res., Weather Modification 71, 3–34. https://doi.org/10.1016/j.atmosres.2004.03.003.

Semeniuk, T.A., Bruintjes, R.T., Salazar, V., Breed, D.W., Jensen, T.L., Buseck, P.R., 2014. Individual aerosol particles in ambient and updraft conditions below

convective cloud bases in the Oman mountain region. J. Geophys. Res. Atmospheres 119, 2013JD021165. https://doi.org/10.1002/2013JD021165.

Seo, Y.-K., Yoon, J.W., Lee, J.S., Hwang, Y.K., Jun, C.-H., Chang, J.-S., Wuttke, S., Bazin, P., Vimont, A., Daturi, M., Bourrelly, S., Llewellyn, P.L., Horcajada, P., Serre, C., Férey, G., 2012. Porous materials: Energy-efficient dehumidification over hierachically porous metal–organic frameworks as advanced water adsorbents (Adv. Mater. 6/2012). Adv. Mater. 24, 710–710. https://doi.org/10.1002/adma.201290026.

Sherman, D.J., 1987. The passage of a weak thunderstorn downburst over an instrumented tower. Mon. Weather Rev. 115, 1193–1205. doi:10.1175/1520-0493(1987)115<1193:TPOAWT>2.0.CO;2

Shrestha, G., Traina, S.J., Swanston, C.W., 2010. Black Carbon's Properties and Role in the Environment: A Comprehensive Review. Sustainability 2, 294–320. doi:10.3390/su2010294

Simpson, J.E., 1972. Effects of the lower boundary on the head of a gravity current. J. Fluid Mech. 53, 759–768. doi:10.1017/S0022112072000461

Simpson, J.E., 1969. A comparison between laboratory and atmospheric density currents. Q. J. R. Meteorol. Soc. 95, 758–765. doi:10.1002/qj.49709540609

Sinha, M.P., Friedlander, S.K., 1985. Real-time measurement of sodium chloride in individual aerosol particles by mass spectrometry. Anal. Chem. 57, 1880–1883. https://doi.org/10.1021/ac00286a019.

Skamarock, W.C., Klemp, J.B., Dudhia, J., Gill, D.O., Barker, D.M., Duda, M., Huang, X.-Y., Wang, W., Powers, J.G., 2008. A Description of the Advanced Research WRF Version 3 (NCAR TECHNICAL NOTE No. NCAR/TN–475+STR). National Center for Atmospheric Research, Boulder, Colorado, USA.

Sorjamaa, R., Svenningsson, B., Raatikainen, T., Henning, S., Bilde, M., Laaksonen, A., 2004. The role of surfactants in Köhler theory reconsidered. Atmos. Chem. Phys. 4, 2107–2117. https://doi.org/10.5194/acp-4-2107-2004.

Sorooshian, A., Feingold, G., Lebsock, M.D., Jiang, H., Stephens, G.L., 2010. Deconstructing the precipitation susceptibility construct: Improving methodology for aerosol-cloud precipitation studies. J. Geophys. Res. Atmospheres 115, D17201. doi:10.1029/2009JD013426

Straka, J.M., 2009. Cloud and Precipitation Microphysics: Principles and Parameterizations. Cambridge University Press.

Tao, W.-K., Chen, J.-P., Li, Z., Wang, C., Zhang, C., 2012. Impact of aerosols on convective clouds and precipitation. Rev. Geophys. 50, RG2001. doi:10.1029/2011RG000369

Tai, Y., Liang, H., Zaki, A., El Hadri, N., Abshaev, A.M., Huchunaev, B.M., Griffiths, S., Jouiad, M., Zou, L., 2017. Core/shell microstructure induced synergistic effect for efficient water-droplet formation and cloud-seeding application. ACS Nano 11, 12318–12325. https://doi.org/10.1021/acsnano.7b06114.

Thaveau, B., Serpolay, R., Piekarski, S., 1987. Influence of surfactants on droplet growth by water vapor condensation on NaCl particles: experimental investigations and theoretical implications. Atmos. Res. 21, 83–96. https://doi.org/10.1016/0169-8095(87)90019-6.

Thompson, G., Eidhammer, T., 2014. A study of aerosol impacts on clouds and precipitation development in a large winter cyclone. J. Atmospheric Sci. 71, 3636–3658. doi:10.1175/JAS-D-13-0305.1

Thompson, G., Field, P.R., Rasmussen, R.M., Hall, W.D., 2008. Explicit forecasts of winter precipitation using an improved bulk microphysics scheme. Part II: Implementation of a new snow parameterization. Mon. Weather Rev. 136, 5095–5115. doi:10.1175/2008MWR2387.1

Tompkins, A.M., 2001. Organization of tropical convection in low vertical wind shears: The role of cold pools. J. Atmospheric Sci. 58, 1650–1672. doi:10.1175/1520-0469(2001)058<1650:OOTCIL>2.0.CO;2

Thompson, G., Tewari, M., Ikeda, K., Tessendorf, S., Weeks, C., Otkin, J., Kong, F., 2016. Explicitly-coupled cloud physics and radiation parameterizations and subsequent evaluation in WRF high-resolution convective forecasts. Atmospheric Res. 168, 92–104. doi:10.1016/j.atmosres.2015.09.005

Tudurí, E., Ramis, C., 1997. The Environments of Significant Convective Events in the Western Mediterranean. Weather Forecast. 12, 294–306. doi:10.1175/1520-0434(1997)012<0294:TEOSCE>2.0.CO;2

Twomey, S., Severynse, G.T., 1963. Measurements of size distributions of natural aerosols. J. Atmospheric Sci. 20, 392–396. https://doi.org/10.1175/1520-0469(1963)020<0392:MOSDON>2.0.CO;2.

Twomey, S., 1974. Pollution and the planetary albedo. Atmos. Environ. 8, 1251–1256. https://doi.org/10.1016/0004-6981(74)90004-3

Vicroy, D.D., 1991. A simple, analytical, axisymmetric microburst model for downdraft estimation (Technical Report No. NASA-TM-104053). NASA Langley Research Center, Hampton, VA, United States.

Vonnegut, B., 1947. The nucleation of ice formation by silver iodide. J. Appl. Phys. 18, 593–595. https://doi.org/10.1063/1.1697813.

Vujović, D., Protić, M., 2017. The behavior of the radar parameters of cumulonimbus clouds during cloud seeding with AgI. Atmos. Res. 189, 33–46. https://doi.org/10.1016/j.atmosres.2017.01.014.

Wakimoto, R.M., 1982. The life cycle of thunderstorm gust fronts as viewed with Doppler radar and rawinsonde data. Mon. Weather Rev. 110, 1060–1082. doi:10.1175/1520-0493(1982)110<1060:TLCOTG>2.0.CO;2

Wakimoto, R.M., Bringi, V.N., 1988. Dual-polarization observations of microbursts associated with intense convection: The 20 July storm during the MIST Project. Mon. Weather Rev. 116, 1521–1539. doi:10.1175/1520-0493(1988)116<1521:DPOOMA>2.0.CO;2

Ward, D.S., Eidhammer, T., Cotton, W.R., Kreidenweis, S.M., 2010. The role of the particle size distribution in assessing aerosol composition effects on simulated droplet activation. Atmos. Chem. Phys. 10, 5435–5447. https://doi.org/10.5194/acp-10-5435-2010.

Weisman, M.L., Klemp, J.B., 1986. Characteristics of isolated convective storms, in: Ray, P.S. (Ed.), Mesoscale Meteorology and Forecasting. American Meteorological Society, pp. 331–358. doi:10.1007/978-1-935704-20-1_15

Weisman, M.L., Klemp, J.B., 1984. The structure and classification of numerically simulated convective stormsin directionally varying wind shears. Mon. Weather Rev. 112, 2479–2498. doi:10.1175/1520-0493(1984)112<2479:TSACON>2.0.CO;2

Weisman, M.L., Klemp, J.B., 1982. The dependence of numerically simulated convective storms on vertical wind shear and buoyancy. Mon. Weather Rev. 110, 504–520. doi:10.1175/1520-0493(1982)110<0504:TDONSC>2.0.CO;2

Wilhelmson, R.B., Klemp, J.B., 1978. A numerical study of storm splitting that leads to long-lived storms. J. Atmospheric Sci. 35, 1974–1986. doi:10.1175/1520-0469(1978)035<1974:ANSOSS>2.0.CO;2

Williams, E., Nathou, N., Hicks, E., Pontikis, C., Russell, B., Miller, M., Bartholomew, M.J., 2009. The electrification of dust-lofting gust fronts ('haboobs') in the Sahel. Atmospheric Res., 13th International Conference on Atmospheric ElectricityICAE 2007 91, 292–298. doi:10.1016/j.atmosres.2008.05.017

Wind Science and Engineering Centre, 2006. A Recommendation for an Enhanced Fujita scale (EF-Scale) (No. 79409–1023). Texas Tech University, Lubbock, Texas.

Wise, M.E., Semeniuk, T.A., Bruintjes, R., Martin, S.T., Russell, L.M., Buseck, P.R., 2007. Hygroscopic behavior of NaCl-bearing natural aerosol particles using environmental transmission electron microscopy. J. Geophys. Res. Atmospheres 112, D10224. https://doi.org/10.1029/2006JD007678.

Xu, Z., Hangan, H., 2008. Scale, boundary and inlet condition effects on impinging jets. J. Wind Eng. Ind. Aerodyn. 96, 2383–2402. doi:10.1016/j.jweia.2008.04.002

You, C.-H., Lee, D.-I., Kang, M.-Y., Kim, H.-J., 2016. Classification of rain types using drop size distributions and polarimetric radar: Case study of a 2014 flooding event in Korea. Atmospheric Res. 181, 211–219. doi:10.1016/j.atmosres.2016.06.024

Zhao, P., Yin, Y., Xiao, H., 2015. The effects of aerosol on development of thunderstorm electrification: A numerical study. Atmospheric Res. 153, 376–391. doi:10.1016/j.atmosres.2014.09.011

Zhao, T., Dai, A., 2015. The magnitude and causes of global drought changes in the twenty-first century under a low–moderate emissions scenario. J. Clim. 28, 4490–4512. https://doi.org/10.1175/JCLI-D-14-00363.1.

Biography

Miloš Lompar was born in Subotica, Serbia in 1987. In 2002, Miloš enrolled natural science and mathematics major in High School "Svetozar Marković" in Subotica, Serbia. In 2006, he enrolled in the Faculty of Physics, University of Belgrade where he obtained his B.Sc. as well as his M.Sc. diplomas in meteorology in 2010 and 2011. In 2009, he was awarded with the annual student grant award from WMO "Borivoje Dobrilović" trust fund as the best student of Meteorology. In 2010 and 2011, Miloš was selected in the group of 1000 best undergraduate and master students in Serbia.

Miloš started his professional career in 2011 in national weather service "Republic Hydrometeorological Service of Serbia" where he works as analyst in numerical weather prediction (NWP) department.

In 2012, Miloš started his Ph. D. studies in the field of meteorology at the Institute for Meteorology, Faculty of Physics, University of Belgrade. His research topic was on the numerical modelling of weather modification process. Miloš has 5 journal articles.

Изјава о ауторству

Потписани-а МИЛОШ ПОМПАР

број уписа _____

Изјављујем

да је докторска дисертација под насловом

NUMERICAL MODELLING OF WARM AND
COLD TYPE RAIN MODIFICATION

- резултат сопственог истраживачког рада,
- да предложена дисертација у целини ни у деловима није била предложена за добијање било које дипломе према студијским програмима других високошколских установа,
- да су резултати коректно наведени и
- да нисам кршио/ла ауторска права и користио интелектуалну својину других лица.

Потпис докторанда

У Београду, 5. 4. 2018.

123

Прилог 2.

Изјава о истоветности штампане и електронске
верзије докторског рада

Име и презиме аутора _МИЛОШ ЛОМПАР_

Број уписа _____

Студијски програм _МЕТЕОРОЛОГИЈА_

Наслов рада _NUMERICAL MODELLING OF WARN AND COLD TYPE RAIN MODIFICATION_

Ментор _ДР. МЛАЂЕН ЋУРИЋ, РЕДОВНИ ПРОФЕСОР_

Потписани _МИЛОШ ЛОМПАР_

изјављујем да је штампана верзија мог докторског рада истоветна електронској верзији коју сам предао/ла за објављивање на порталу **Дигиталног репозиторијума Универзитета у Београду.**

Дозвољавам да се објаве моји лични подаци везани за добијање академског звања доктора наука, као што су име и презиме, година и место рођења и датум одбране рада.

Ови лични подаци могу се објавити на мрежним страницама дигиталне библиотеке, у електронском каталогу и у публикацијама Универзитета у Београду.

Потпис докторанда

У Београду, _5.4.2018._

Прилог 3.

Изјава о коришћењу

Овлашћујем Универзитетску библиотеку „Светозар Марковић" да у Дигитални репозиторијум Универзитета у Београду унесе моју докторску дисертацију под насловом:

<u>NUMERICAL MODELLING OF WARM AND COLD TYPE</u>
<u>RAIN MODIFICATION</u>

која је моје ауторско дело.

Дисертацију са свим прилозима предао/ла сам у електронском формату погодном за трајно архивирање.
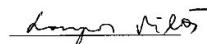
Моју докторску дисертацију похрањену у Дигитални репозиторијум Универзитета у Београду могу да користе сви који поштују одредбе садржане у одабраном типу лиценце Креативне заједнице (Creative Commons) за коју сам се одлучио/ла.

1. Ауторство

2. Ауторство - некомерцијално

3. Ауторство – некомерцијално – без прераде

4. Ауторство – некомерцијално – делити под истим условима

5. Ауторство – без прераде

6. Ауторство – делити под истим условима

(Молимо да заокружите само једну од шест понуђених лиценци, кратак опис лиценци дат је на полеђини листа).

Потпис докторанда

У Београду, <u>5. 4. 2018.</u>

1. Ауторство - Дозвољавате умножавање, дистрибуцију и јавно саопштавање дела, и прераде, ако се наведе име аутора на начин одређен од стране аутора или даваоца лиценце, чак и у комерцијалне сврхе. Ово је најслободнија од свих лиценци.

2. Ауторство – некомерцијално. Дозвољавате умножавање, дистрибуцију и јавно саопштавање дела, и прераде, ако се наведе име аутора на начин одређен од стране аутора или даваоца лиценце. Ова лиценца не дозвољава комерцијалну употребу дела.

3. Ауторство - некомерцијално – без прераде. Дозвољавате умножавање, дистрибуцију и јавно саопштавање дела, без промена, преобликовања или употребе дела у свом делу, ако се наведе име аутора на начин одређен од стране аутора или даваоца лиценце. Ова лиценца не дозвољава комерцијалну употребу дела. У односу на све остале лиценце, овом лиценцом се ограничава највећи обим права коришћења дела.

 4. Ауторство - некомерцијално – делити под истим условима. Дозвољавате умножавање, дистрибуцију и јавно саопштавање дела, и прераде, ако се наведе име аутора на начин одређен од стране аутора или даваоца лиценце и ако се прерада дистрибуира под истом или сличном лиценцом. Ова лиценца не дозвољава комерцијалну употребу дела и прерада.

5. Ауторство – без прераде. Дозвољавате умножавање, дистрибуцију и јавно саопштавање дела, без промена, преобликовања или употребе дела у свом делу, ако се наведе име аутора на начин одређен од стране аутора или даваоца лиценце. Ова лиценца дозвољава комерцијалну употребу дела.

6. Ауторство - делити под истим условима. Дозвољавате умножавање, дистрибуцију и јавно саопштавање дела, и прераде, ако се наведе име аутора на начин одређен од стране аутора или даваоца лиценце и ако се прерада дистрибуира под истом или сличном лиценцом. Ова лиценца дозвољава комерцијалну употребу дела и прерада. Слична је софтверским лиценцама, односно лиценцама отвореног кода.